Optoelectronic Properties of Semiconductor Nanowires in the Infrared Regime

Sabrina Sterzl

Somerville College

University of Oxford

A thesis submitted for the degree of

Doctor of Philosophy

Hilary 2020

Acknowledgements

People say that it needs a village to raise a child. The same is also true for writing a PhD thesis.

First, I want to thank the European Union and its Framework Program for Research and Innovation Horizon 2020. They enabled my work and gave me the opportunity to meet amazing people all over the world.

I also owe much gratitude to my supervisor Professor Michael Johnston, who gave me the chance to perform further studies on my favourite subjects — nanowires. He gave me the support and knowledge to develop as a scientist and person. I would also like to show my appreciation to Professor Laura Herz. She has been a great inspiration. Both of them have built an amazing group together.

I had so much fun with my colleagues and found support in my desperate moments, when nothing wanted to work. They aren't just colleagues, but also my friends. Thanks to all of you!

I especially want to mention Dr. Kun Peng, who ignited my love for science again. She is the most optimistic person I know and she was always up for a good discussion and encouraging words. I also want to thank my "supervisor in the lab" Dr. Jessica Boland, who made the lab into a stage. She taught me THz spectroscopy, puns and banter.

Building the PL setup would have not been possible without the electrical and mechanical workshops of the department. I especially want to shout out to Nick Callaghan for my new PL sample chamber and to Rik Elliot for repairing and reworking the cold fingers. Also special thanks to Dr. Lavina Snoek. She always offered me a third and fourth hand for aligning and her knowledge from the time when she built her own setup.

During my PhD, I was part of the innovative training network ITN INFORM. This enabled me to travel throughout Europe, participating in amazing workshops and meeting great scientists. I am happy that I could spend this amazing time with the other members of this group.

I was able to do internships at three different groups and to learn new techniques, such as ALD, TEM and device fabrication. I met so many amazing people who welcomed me with open arms and taught me patiently. I especially want to thank Professor Anna Fontcuberta i Morral from École polytechnique fédérale de Lausanne

(EPFL), Professor Gitti Frey, Tanmoy and Tias Sarkar from Technion, and Dr. Claire Burgess, David Poussin and Dr. Martin McLachlan from Imperial College London.

I also want to acknowledge and thank all my collaborators who provided me with samples. I especially want to thank the people whose samples are mentioned in this thesis: Dr. Heidi Potts, Dr. Hannah Joyce, Naiyin Wang, and Yizhen Ren.

I am so thankful that my PhD not only enabled me to follow my passion, but also to find the most amazing and supportive friends in the world. I personally want to thank Mie for giving me the best company possible at the good place, Michael for his warmth, support and brownies, and Shrav for his hope. Also cheers to Adam, who explained to me everything from science to British humour and Crista who was my shield. Thanks for offering me your food, roof and kindness. I would also like to thank my old friends for never giving up on me. Finally, I want to thank my whole family who all rooted for me. You brought me up, always supported and encouraged me. You gave me the strength, love, and stubbornness to survive everything.

Abstract

Semiconducting nanowires are promising elements for potential use in nanoscale devices. Due to their versatility, they can be utilised for a wide range of applications. To correlate the nanowires with their best possible device applications, a powerful all-optical platform was developed to characterise both their electrical and optical properties by combining terahertz spectroscopy and photoluminescence spectroscopy. The focus will be on three different material systems (gallium phosphide, silicon-germanium, indium arsenide) and their potential use for optoelectronic devices in the infrared region of the electromagnetic spectrum.

Theory has predicted a direct bandgap for silicon-germanium alloys grown in a hexagonal crystal phase, but it has not been experimentally proven so far. This thesis demonstrates the realization of hexagonal silicon and silicon-germanium via template-assisted nanowire growth. The characterisation of these hexagonal nanowires is depicted via a series of terahertz and photoluminescence spectroscopy measurements to study their electrical and optical properties and therefore confirm information about their bandgap. Firstly, hexagonal gallium phosphide nanowires, including the effect of the different growth recipes and defects, are studied as they form the template (nanowire core) for later shell growth of hexagonal silicon and silicon-germanium. The structural flaws in gallium phosphide nanowires under different growth conditions are qualitatively examined; these defects can be further transferred to the shell growth, and thus determine the shell quality. In the following, the core-shell nanowires, including hexagonal silicon shell and hexagonal silicon-germanium shell (with varying germanium contents), are investigated. Defect density is found to correlate strongly with the photoconductivity lifetime. For the first time, the surface recombination velocity of hexagonal silicon is determined. Meanwhile indications of a direct bandgap of hexagonal silicon are observed and elaborated on. Theoretical calculations are used to support the rare case of a direct bandgap in silicon. It is anticipated that such silicon nanowires could be designed as high-emission-efficiency nanolasers, which could revolutionize the field of silicon-based technology.

With the same characterisation tools, a second semiconducting nanowire system — indium arsenide and its compound indium arsenide antimonide — is investigated. Such a type of material has naturally a direct bandgap, which can be tuned from

0.1 eV to 0.4 eV (by changing its composition). Therefore, the study of these indium-arsenide based nanowires aids in the design of higher-performance devices. To give a thorough overview, nanowires grown via metal organic vapour phase epitaxy and molecular beam epitaxy are compared. They are also passivated with Al_2O_3 because these nanowires are surface sensitive. The influence of diameter, crystal structure and passivation layer on their electrical and optical properties are systemically studied. Furthermore, the bandgap engineering of indium arsenide antimonide and the benefits of doping are discussed. Finally, indium arsenide nanomembranes are proposed as an alternative to the nanowires for the optimal design of future nanoscale optoelectronic device systems.

Contents

List of Figures **xi**

List of Tables **xiii**

List of Publications **xv**

List of Abbreviations **xvii**

1 Introduction **1**

1.1 Motivation 1

1.2 Thesis Overview 2

2 Semiconducting nanowires **5**

2.1 Nanowire growth 5

2.1.1 Growth techniques 6

2.1.2 Heterostructures 9

2.1.3 Crystal structures 12

2.1.4 Doping 14

2.2 Semiconductors 15

2.2.1 Basics 15

2.2.2 Recombination mechanisms 17

2.2.3 Recombination rate model 20

2.3 Nanowire devices 22

2.3.1 Thermoelectric devices 23

2.3.2 Solar cells 24

2.3.3 Detectors 24

2.3.4 Light emitting devices 26

2.4 Summary 28

3 Experimental Methods **29**

3.1 THz spectroscopy 29

3.1.1 Introduction to THz spectroscopy 29

3.1.2 Optical-Pump THz-Probe setup 32

3.1.3 Data analysis of nanowire samples 37
3.2 Sample preparation 43
3.3 Summary 46

4 Development of cryogenic mid-infrared Fourier Transform Photoluminescence system 47
4.1 Photoluminescence Spectroscopy 47
4.1.1 Introduction to Photoluminescence Spectroscopy 47
4.1.2 Fourier Transform Infrared Spectrometry 48
4.1.2.1 Functional principles 48
4.1.2.2 Usage of Fourier Transform Infrared Spectrometer . 49
4.1.2.3 Fourier Transform Photoluminescence Spectroscopy 50
4.2 Custom-designed Fourier Transform Photoluminescence system . . . 50
4.2.1 Custom components 50
4.2.1.1 Sample chamber 50
4.2.1.2 Sample holder 53
4.2.1.3 System setup 54
4.2.2 Measurement of Fourier Transform Photoluminescence . . . 55
4.2.2.1 Scanning parameters 55
4.2.2.2 Calibration 58
4.3 Summary 58

5 Wurtzite GaP nanowires 61
5.1 Wurtzite GaP nanowires as template for hexagonal silicon 61
5.2 Sample preparation 62
5.3 OPTP setup optimisation for GaP nanowires 65
5.4 Degradation of GaP nanowires 66
5.5 Correlation of lifetime and growth parameters 70
5.6 Improved lifetime due to a two-step growth process 73
5.7 Summary 78

6 Lonsdaleite phase Si and SiGe nanowires 79
6.1 Efficient silicon optoelectronic applications 79
6.2 The lonsdaleite phase 81
6.3 Fabrication of Si and SiGe in the lonsdaleite phase 84
6.4 Lonsdaleite phase SiGe nanowires with different Ge contents 86
6.5 Defects and their influence on electrical properties in lonsdaleite Si . 89
6.6 Surface recombination of hexagonal silicon 92
6.7 Silicon as direct bandgap material? 95
6.8 Summary 103

7 Light emission from InAs-based nanowires 105
7.1 Introduction to InAs NWs 105
7.2 InAs NW passivation 106
7.2.1 MBE-grown InAs nanowires 108
7.2.1.1 Growth 108
7.2.1.2 Passivation effect on optical and electrical properties 109
7.2.2 Passivation dependence on crystal structure and sample geometry of MOVPE-grown InAs Nanowires 114
7.2.2.1 Growth 115
7.2.2.2 Experiments and Results 116
7.2.3 Comparison of MBE- and MOVPE-grown InAs NW passivation 128
7.3 InAsSb compositions 128
7.3.1 Growth and crystal structure 129
7.3.2 Bandgap dependence on Sb content 130
7.4 Summary 132
7.5 Outlook 133

8 Conclusion and Outlook 135
8.1 Summary 135
8.2 Further work 137

Bibliography 141

x

List of Figures

2.1 Schematic illustration of VLS growth 7
2.2 Heterostructures of NWs 10
2.3 Crystal structure of ZB, WZ, and Lonsdaleite 12
2.4 Schematic illustrations of SC bandgaps 16
2.5 Schematic illustrations of recombination mechanisms 18
2.6 Radiative efficiency in correlation to carrier density 21
2.7 NAND gate made of NWs 27

3.1 THz pulse and beamwidth 30
3.2 Schematic of THz spectroscopy 31
3.3 Schematic of OPTP system 33
3.4 THz detection 34
3.5 Photoconductivity decay of InGaAs NWs 37
3.6 Diameter dependent lifetimes of NWs 38
3.7 Spectra of conductivity models 40
3.8 Effect of refractive index change on InP NWs 42
3.9 NWs on substrate 43
3.10 Nanoscale transfer printing 45

4.1 Michelson interferometer in FTIR 48
4.2 CAD model of PL sample chamber 51
4.3 Cold finger and sample holders 53
4.4 Schematic of the FTIR PL system 60

5.1 Impact of optimising the OPTP system 66
5.2 Sample stability during OPTP spectroscopy 67
5.3 Degradation of GaP NWs under nitrogen atmosphere 68
5.4 Degradation under different atmospheres 69
5.5 Influence of V/III ratio on defect density and lifetimes of GaP NWs 71
5.6 Dependence of photoconductivity lifetime on defect density 72
5.7 Fluence-dependent lifetime for single-step and two-step series 73
5.8 Lifetime of GaP NWs in relation to diameter 77

6.1 Band structures of cubic and lonsdaleite Si and Ge 82
6.2 Growth of hexagonal SiGe NWs 84
6.3 OPTP spectroscopy on hexagonal SiGe 87
6.4 Influence of defective morphology on electrical NW properties . . . 90
6.5 Lifetimes of hexagonal Si before and after optimisation of wet-etching 92
6.6 Surface recombination velocity of hexagonal Si NWs 94
6.7 Global fitted photoconductivity decays of hexagonal Si indicating direct bandgap 95
6.8 Doping concentration in Si/GaP NWs 100
6.9 Comparison of global fits 101
6.10 PL spectra of hexagonal Si NW 102

7.1 Lifetime comparison of passivated and unpassivated InAs NWs . . . 111
7.2 Fluence-dependent spectra of MBE-grown InAs NWs 112
7.3 PL spectra of passivated and unpassivated InAs NWs 113
7.4 Integrated PL intensity and FWHM of passivated and unpassivated InAs nanowires 113
7.5 Cross-section of ZB and WZ structure 114
7.6 Spectra of InAs substrate and MOVPE-grown InAs NWs 117
7.7 Mott transition of InAs 119
7.8 Diameter-dependent spectra of passivated and unpassivated pure-phase WZ and ZB InAs NWs 120
7.9 Diameter-dependent peak position and intensity of InAs nanowires . 121
7.10 Fluence-dependent peak position and intensity of InAs NWs 123
7.11 Boxplot of the power law coefficient α 124
7.12 Lifetimes and surface recombination velocities of MOVPE-grown InAs NWs 126
7.13 Optical bandgap for InAsSb NWs with varying Sb content 130
7.14 SEM image and PL spectra of InAs nanomembranes 133

List of Tables

4.1 Settings of the FTIR software OPUS and the lock-in amplifier for FTIR PL spectroscopy on nanowire samples 57

5.1 Overview of the wurtzite GaP nanowire samples which are divided into two series. 63

6.1 Sample description of the $Si_{1-x}Ge_x$ nanowire series: the germanium content and the shell thickness are given for the six samples. 86

6.2 Rate equation coefficients for different direct and indirect bandgap semiconductors. 98

7.1 Overview of surface and volume lifetimes of passivated and unpassivated MBE-grown InAs nanowires with different diameters. 110

List of Publications

Jessica L. Boland, Francesca Amaduzzi, **Sabrina Sterzl**, Heidi Potts, Laura M. Herz, Anna Fontcuberta i Morral, and Michael B. Johnston. High Electron Mobility and Insights into Temperature-Dependent Scattering Mechanisms in InAsSb Nanowires. Nano Lett., 18(6):3703–3710, 2018

Sabrina Sterzl, Hannah Joyce, Lavina Snoek, and Michael B. Johnston. Dependence of passivation, crystal structure and geometry of MOVPE grown InAs nanowires on electrical and optical properties - in preparation

Sabrina Sterzl, Yizhen Ren, Kun Peng, Mathias U. Rothmann, Jos E.M. Haverkort, Erik P.A.M. Bakkers, and Michael B. Johnston. Indication for direct bandgap in hexagonal Si - in preparation

Yizhen Ren, **Sabrina Sterzl**, Marcel Verheijen, Michael B. Johnston, and Erik P.A.M. Bakkers. Carrier lifetime as a function of basal stacking fault density in hexagonal GaP - in preparation

Kun Peng, Dimitars Jevtics, Fanlu Zhang, **Sabrina Sterzl**, Djamshid A. Damry, Mathias U.Rothmann, Hark Hoe Tan, Laura M. Herz, Lan Fu, Antonio Hurtado, Chennupati Jagadish, and Michael B. Johnston. 3D-cross nanowire networks recover full terahertz state - in preparation

List of Abbreviations

ALD . . . . . . atomic layer deposition
AlGaAs . . . . aluminium gallium arsenide
ANU . . . . . . Australian National University
APD . . . . . . avalanche photodiode
APT . . . . . . atom probe tomography
AsH_3 . . . . . . arsenide
BBO . . . . . . beta barium borate
BS . . . . beamsplitter
CCS-MOVPE close-coupled showerhead MOVPE
CVD . . . . . . chemical vapour deposition
EO . . . . electro-optic
EPFL . . . . . École polytechnique fédérale de Lausanne
$FASnI_3$ . . . . formamidinium tin triiodie
FM . . . . ferromagnetic
FTIR . . . . . Fourier Transform Infrared Spectrometer
FTIR PL . . . mid-infrared Fourier transform photoluminescence
FWHM . . . . full width at half maximum
GaAs . . . . . gallium arsenid
GaP . . . . . . gallium phosphide
GaSb . . . . . gallium antimonide
Ge . . . . germanium
GeH_4 . . . . . germane
HCl . . . . . . hydrogen chloride
He . . . . helium
InAs . . . . . . indium arsenide

InAsSb . . . . indium arsenide antimonide
IR . . . . infrared
MBE . . . . . . molecular beam epitaxy
MIS . . . . . . metal-insulator-semiconductor
MOVPE . . . metalorganic vapour phase epitaxy
MSM . . . . . metal-semiconductor-metal
nano-TP . . . nanoscale transfer printing
Na_2S . . . . . . sodium sulfide
ND . . . . neutral density
NM . . . . . . non-ferromagnetic
NW . . . . . . nanowire
OAP . . . . . . off-axis parabolic mirror
ODT . . . . . . organic sulfide oxtadecylthiol
OPTP . . . . . Optical-Pump THz-Probe
PH_3 . . . . . . phosphine
PL . . . . photoluminescence
ppm . . . . . . parts per million
SA-VLS . . . . selective area vapour-liquid-solid
SAM . . . . . . self assembled monolayer
Sb . . . . antimonide
SC . . . . semiconductor
SEM . . . . . . scanning electron microscopy
Si . . . . silicon
SiGe . . . . . . silicon-germanium
Si_2H_6 . . . . . disilane
TEM . . . . . . transmission electron microscopy
THz . . . . . . terahertz
THz-TDS . . . THz time-domain spectroscopy
TMA . . . . . trimethylaluminium
TMI . . . . . . trimethylindium
TMGa . . . . . trimethylgallium

VLS . . . . . . vapour-liquid-solid

VS . . . . vapour-solid

WZ . . . . wurtzite

ZB . . . . zincblende

1 Introduction

1.1 Motivation

Industry, research and society are continuously looking for new solutions to solve current and future problems: there is a continuous demand for more compact and powerful electronic/optoelectronic devices (e.g. smartphones, computers, and lasers) to deal with rising challenges in business and daily life [1]. It would be ideal if the production of energy for those needs would be renewable. There are many different possible solutions. Semiconducting nanowires are especially promising due to their diversity and exceptional properties, as described below.

Nanowires are tiny structures with a specific geometry that has a length-to-diameter ratio larger than 10. Their length is commonly around a few micrometre and the diameter varies between a few to a few hundred nanometres depending on their application purpose. Thus, nanowires have a large surface-to-volume ratio. This enables nanowire heterostructures to be grown free from the lattice mismatch problems that are significant for bulk or thick film [2], and even to be directly integrated onto commercially used wafers and computer chips [3]. Atomically-sharp interfaces in heterostructured nanowires can be created without dislocations [4].

All these features make nanowires ideal candidates for new devices in various application areas. For example, silver nanowires have been widely used as transport

electrodes [5], and light-emitting diodes made of gallium nitride nanowires have reached the market [6]. Other commercially-produced nanowire products are rare even though a variety of material types, heterostructures, and geometries for nanowires have been realised.

This thesis tries to build a bridge between nanowire growth and device fabrication by characterising nanowires for their optical and electrical properties using photoluminescence (PL) and terahertz (THz) spectroscopy. This strategy allows the identification of factors that need to be improved in the growth or device design, for example, providing guidance for the selection of the most suitable nanowire type for scientific application.

The research performed for this thesis specialises in the study of semiconducting nanowires with light emission in the infrared (IR) regime because it is of greatest interest for optical communication. Nowadays infrared technology has issues with reliability, toxicity, cost, cryogenic cooling, and size restrictions depending on the type of device used [7]. Therefore, this field, especially the development of infrared-emitting nanowire lasers or nanoscale infrared-light sensors, could be an interesting niche area for semiconducting nanowires in industrial applications.

1.2 Thesis Overview

The goal of this thesis is to investigate the electrical and optical properties of semiconducting nanowires which are emitting photons in the infrared, in order to help develop devices like infrared nanowire detectors and lasers. Therefore, nanowires from different material systems are investigated with a focus on their growth, crystal structure, geometry, defects, and passivation.

Chapter 2 starts with an introduction to semiconducting nanowires. A summary of growth techniques, including "top-down" and "bottom-up" fabrication, different growth regimes, assistance by templates, and fabrication systems is given. A deep discussion on heterostructures is presented, which offers the possibility of complex design and device optimisation due to the large surface-to-volume ratio resulting in strain relaxation. Crystal structures, doping and their significant influence on

the nanowires are also touched upon. Afterwards, the concepts of semiconductor properties which are necessary as background knowledge for this thesis are discussed, including charge-carrier recombination mechanisms and a model describing them. Finally, promising areas for nanowire application in photonic devices are introduced.

Chapter 3 describes the experimental methods used in this thesis. The setup and principles of THz spectroscopy is explained including a method of how to analyse the results for nanowire samples. Furthermore, different ways to transfer nanowires from the growth substrate to a target one are discussed.

Photoluminescence (PL) spectroscopy was performed on a self-built cryogenic mid-infrared Fourier transform photoluminescence (FTIR PL) system. The development of this system is given in Chapter 4. Firstly, PL spectroscopy is described in general. Next, the advantages and functional principles of a Fourier Transform Infrared Spectrometer (FTIR) are given. Then the whole system is discussed focusing on PL vacuum chamber, sample holder and calibration. Also, examples for the scan parameters are presented.

Chapter 5 is the first section investigating nanowires. The properties of wurtzite gallium phosphide (GaP) nanowires are characterised in order to better understand their application as a template for infrared emitting, hexagonal silicon (Si) and silicon-germanium (SiGe) in the lonsdaleite crystal structure. The shell adapts to the underlying GaP crystal structure, including its defects. Due to the influence of the GaP core, a better understanding of the template is needed. For this reason, the degradation and the influence of growth on the photoconductivity lifetime is discussed.

Having investigated wurtzite GaP nanowires as templates, the attention in Chapter 6 is turned to the materials in lonsdaleite phase grown around the GaP core. According to theoretical calculations, hexagonal $Si_{1-x}Ge_x$ has a direct bandgap for a range of alloy fractions, x, and hexagonal Si has a smaller indirect bandgap than cubic silicon, all emitting in the near-infrared. In order to verify this band structure, THz spectroscopy was performed on hexagonal Si and SiGe. First, the importance of a direct bandgap of Si(Ge) for contemporary industrial applications

is discussed, followed by the definition of and a short introduction to the crystal structure lonsdaleite. Then the results obtained from hexagonal SiGe with different germanium (Ge) contents and hexagonal Si samples with varying thicknesses are analysed. For the first time, the surface recombination velocity of hexagonal silicon is extracted and evidence for a direct bandgap for hexagonal silicon is shown.

For a broader understanding of infrared emission of nanowires, a material system emitting in the mid-infrared is introduced in Chapter 7. Nanowires based on indium arsenide (InAs) and its compound indium arsenide antimonide (InAsSb) are investigated, compared to each other and their electrical and optical properties are analysed by THz and PL spectroscopy. First, the effect of Al_2O_3 passivation on molecular beam epitaxy (MBE) grown nanowires is analysed. Then the results are compared to metal organic vapour phase epitaxy (MOVPE) grown InAs wires with and without an Al_2O_3 layer. Furthermore, the effect of diameter and crystal structure on electrical and optical properties are investigated. Then InAsSb nanowires are introduced. They enable engineering of the bandgap in the infrared regime. In the outlook, InAs nanomembranes are introduced as a possible alternative to nanowires for better device performance (e.g. higher signal-to noise ratio).

The final Chapter 8 draws together the studies on nanowire materials emitting in the infrared and provides an outlook for the next steps to gain a deeper understanding of semiconducting nanowires in the design of infrared devices.

2
Semiconducting nanowires

"Semiconducting nanowires offer the possibility of nearly unlimited complex bottom-up design" (R.E. Algra) [8].

Nanowires (NWs) are very versatile, which allows diverse material combinations and new crystal structures to be achieved, thus enabling individual tailoring of devices and creating novel applications. Nanowires possess a high surface-to-volume ratio, which is among their most distinguishing properties and allows for applications only feasible to nanowires due to their unique one-dimensional structure.

In the following, I will give a short introduction to different nanowire growth techniques, common growth systems, nanowire heterostructures, passivation layers and crystal structures. Furthermore, I will introduce some basics of semiconductors with the focus on charge-carrier recombination mechanisms, which will be mentioned frequently throughout this thesis. Finally, I will list a few potential nanowire applications in optoelectronics related to this thesis.

2.1 Nanowire growth

The growth control of nanowires is essential to their applications. To achieve the desired material properties, the appropriate growth system and technique for producing nanowires needs to be developed.

2.1.1 Growth techniques

"Top-down" and "bottom up" fabrication

The first nanowires were grown by Wagner *et al.* [9] in the 1960s when trying to create two-dimensional layers: the additional wire-like structures were seen as parasitic growth [10]. Since then, potential applications of nanowires have been discovered and different growth techniques have been developed to control their properties. Fabrication of nanowires can be divided into "bottom-up" and "top-down".

"Top-down" describes all techniques where a three-dimensional bulk material is reduced and shaped until a nanowire structure is achieved. Lithography and etching enables well-controlled fabrication of complex structures. For example, Rauber *et al.* [11] fabricated a complex three-dimensional structure of crossing nanowires by etching channels in a polymer block. The channels were filled with a chosen material and the residual polymer was removed.

The "top-down" technique enables very complex, otherwise unattainable structures, but the surfaces are usually rough and have many defects detrimental for applications. "Bottom-up" fabrication is used to combine materials with different lattice constants in a defect-free manner [2]. This technique includes all methods which grow nanowires from a substrate. The different ways to grow nanowires can be classified by substrate preparation, nucleation seed, and the reaction causing the growth. In the following, an overview of the most used mechanisms is given.

Vapour-liquid-solid growth

Nanowires are frequently grown via vapour-liquid-solid (VLS) growth. For VLS, a liquid metal droplet, usually gold, is deposited on the substrate. It acts as a catalyst, lowering the activation energy for nanowire growth. Simultaneously, it also acts as reservoir for the impinging gaseous molecules [12]. When the droplet reaches supersaturation, a nanowire grows at the interface of the solid substrate and the liquid droplet. New incoming gaseous atoms impinge on the droplet and maintain constant saturation, while the nanowire continues growing [9]. The incoming molecules can also be adsorbed on the growth substrate or the nanowire's

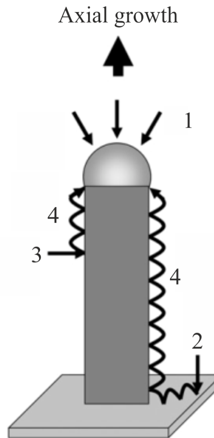

Figure 2.1: Schematic illustration of VLS growth: 1) The gaseous molecules impinge on the liquid catalyst droplet and crystallise on the solid-liquid interface initialising axial growth. Other molecules adsorb at the 2) substrate or 3) nanowires side facets. 4) Then they diffuse towards the droplet or crystallise on side facets causing radial growth. Adapted from Ref. [2].

side facets. Then they can either diffuse towards the droplet or crystallise on the side facets causing radial growth and tapering. Figure 2.1 illustrates this process.

The direction of the wire is determined by the surface energy and crystal structure of the growth substrate. Depending on the lowest energy, the nanowire can grow vertically or horizontally [13, 14, 15]. The length of the wires is limited by the diffusion length of the adsorbed molecules which is typically around 1 to 10 μm. The diameter of the nanowire is determined by the droplet size. As a result, the growth can be tapered when atoms of the catalyst are incorporated into the nanowire and the droplet size decreases [12].

Different types of catalysts for nanowire growth

If the catalyst's atoms are incorporated, they can contaminate the wire and negatively affect the quality. For example, metal atoms can form deep level traps in silicon nanowires [16]. Such a contamination can be prevented by changing the VLS growth from metal-induced — using a metal droplet as catalyst — to self-induced — using a droplet consisting of one element used for the nanowire [12]. In some cases, the growth can be performed without any droplet. This is called metal-free or catalyst-free growth. A switch between self-induced and

metal-free growth can be realized by minor adjustments of the growth parameters [17]. However, the growth mechanism of catalyst-free growth is different to VLS growth. The nucleation of the nanowire is facet-driven and depends strongly on the substrate and its crystal direction. Nanowires usually prefer the <111> growth direction [12]. The atoms in the growth chamber impinge directly on the substrate and diffuse until they are integrated in the nanowire [16].

Template assisted growth

All "bottom-up" nanowires can be grown template-assisted or template-free. Template-free growth can achieve a higher nanowire yield, but the positions of the wires on the as-grown substrate are randomly distributed. For template-assisted growth, different kinds of templates can be used: substrate patterning, oxide nanotube templates, and nanowire core templates.

If substrate patterning is used, the starting point of growth is imposed and the size and yield of the nanowires is determined. For VLS growth, the patterning can be achieved by controlling the location and size of the catalyst, for example with lithography [2]. If the growth is metal-free, controlled nucleation seeds can be fabricated by covering the wafer with an oxide layer and etching holes into the oxide until they reach the substrate [18]. This method can also be applied to catalyst-assisted growth.

Vertically- or horizontally-grown oxide nanotubes are a different kind of template which guides the growth of nanowires. This method enables the growth in crystal directions independent of the substrate's crystal structure. Even the fabrication of horizontally grown nanowires is possible [19, 20, 21, 22].

A nanowire can also become a template for the shell growing around it. This method is used to obtain a better control over crystal structures of certain materials, such as gallium antimonide (GaSb), Si [23, 24] or the hexagonal silicon and silicon-germanium studied in this thesis. This process allows heterostructure growth, which is discussed in Section 2.1.2.

Growth regimes

Not only the choice of catalyst and template is important, but also the spacing

between the wires. The distance between the nucleation sites determines the growth regime of the nanowires. For large widths, growth is diffusion-limited and for smaller ones competitive-limited. Diffusion-limited means that all atoms within the distance of diffusion length can contribute to the growth. Therefore, the diffusion length determines the nanowire's length. In the competitive growth regime, the number of molecules, which are adsorbed and move within one diffusion length, is shared between different nanowires and therefore, the growth is hampered [18].

Growth systems

All this "bottom-up" growth can be achieved with technologies relying on either physical or chemical mass transport. For both methods, there are many different approaches [25, 26, 27]. In this thesis, the nanowire samples were fabricated using two commonly used methods: molecular beam epitaxy (MBE) and metalorganic vapour-phase epitaxy (MOVPE).

MBE growth is based on physical reactions. Under ultra-high vacuum, elements are heated up to a gaseous state. Then the atoms are directed onto a substrate, where they are physically adsorbed. MOVPE is based on chemical reactions. Different gaseous precursors are flowing over or along a substrate. There they undergo a chemical reaction and adsorb on the substrate. The by-products of the chemical reactions are taken away by an inert carrier gas. The two growth methods have different advantages and disadvantages, but both of them can achieve similar results, even if the growth parameters, such as temperature, pressure or nucleation process, are different [28, 29]. For example, GaAs nanowires were fabricated by Rudolph *et al.* via self-induced growth with Ga droplets using MBE [18] and by Ikejiri *et al.* with metal-free growth using MOVPE [30].

2.1.2 Heterostructures

The nanowires' versatility allows for optimisation of their material properties for various applications. This versatility originates from the possibility to combine many different materials using the methods described above. Fabricating heterostructures can induce strain and may result in defects. However, nanowires have a large

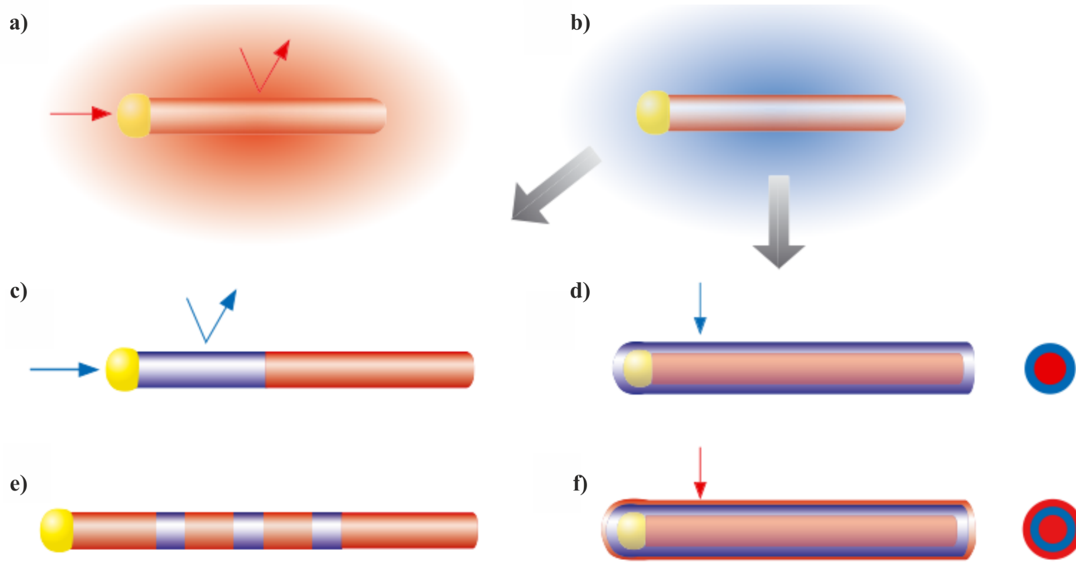

Figure 2.2: Illustration of axial and radial growth of nanowires: (a) axial VLS growth of nanowires. (b) Introduction of a different material (blue) enabling either (c) axial heterostructure growth or (d) radial overgrowth of the core material (red). Superlattices formed by (e) axial growth and (f) radial growth by continuous switching of alternating materials. Adapted from Ref. [31].

surface-to-volume ratio enabling the relaxation of the strain caused by lattice mismatch [32, 33]. Heterostructures can be divided into polytypism, radial, and axial heterostructures.

Radial and axial heterostructures describe the geometry in which the different materials are combined. The different growth structures and changes of materials are illustrated in Figure 2.2. Axial growth describes the growth along the nanowire axis with a constant nanowire diameter, while radial growth refers to growth around the nanowire core. If a new material is introduced (Figure 2.2b), the growth continues either axially (Figure 2.2c) or radially (Figure 2.2d).

At an axial heterostructure interface, the material changes, but the nanowire continues growing along the wire axis. If the materials are switched multiple times within a few nanometres, an axial superlattice can be fabricated (Figure 2.2e). The interfaces can be achieved with atomically sharp junctions [2, 28, 31]. However, abrupt interface changes cannot be achieved for all growth techniques. For example during VLS growth, the catalyst droplet can act as a reservoir for the first material even after the second material has been introduced to the system. Furthermore, the

droplet can migrate from its original position on top of the wire, in order to obtain a lower surface energy. This can result in a change of growth direction [2, 34].

Radial growth can only be achieved by vapour-solid (VS) growth [35]. For this method, the gaseous molecules are directly adsorbed on the solid interfaces of the nanowire. The growth parameters are different from axial growth, because the side facets have a lower surface energy than the top facet [36]. Therefore, neither a sudden change of growth direction or an gradual interface caused by the reservoir of the catalyst can occur. For radial heterostructures, shells with different materials are grown around the nanowire core (Figure 2.2d). A shell structure can be used to fabricate, among others, quantum wells [4, 37, 38] within wires and large area junctions [14, 39, 40]. A capping layer can be added that way, in order to protect the surface from degradation and surface effects. These layers do not need to be necessarily fabricated in the same setup [41, 42, 43].

Radial growth has the disadvantage that the strain cannot be released as easily as in axial structures. Therefore, the shell can be inhomogeneous. For an instance in gallium arsenide/ aluminium gallium arsenide (GaAs/AlGaAs) core-shell nanowires, there are Al-rich stripes along the corners of the hexagonal AlGaAs shell forming one-dimensional channels [36]. Radial growth can also be applied to grow a material in a specific crystal structure. The core can act as a template for the shell and the shell adopts the crystal structure of the core independent of its own preferred structure. This was shown by Paladugu *et al.* [44], who grew different heterostructures with InAs, whose preferred crystal structure is wurtzite, and GaAs, which preferably grows in a zincblende structure. When InAs was grown around a GaAs core, the material adapted to GaAs's zincblende phase. However, when InAs was the core material, GaAs grew in the wurtzite phase. This effect is useful to grow materials in a structure in which they could not usually or easily be fabricated without template. This method enabled the growth of GaSb in the wurtzite phase around a wurtzite InAs nanowire [24]. Algra *et al.* fabricated a wurtzite/zincblende superlattice made of silicon, whose crystal structures usually are hard to control [23]. It was even possible to grow silicon nanowires in the lonsdaleite phase [45],

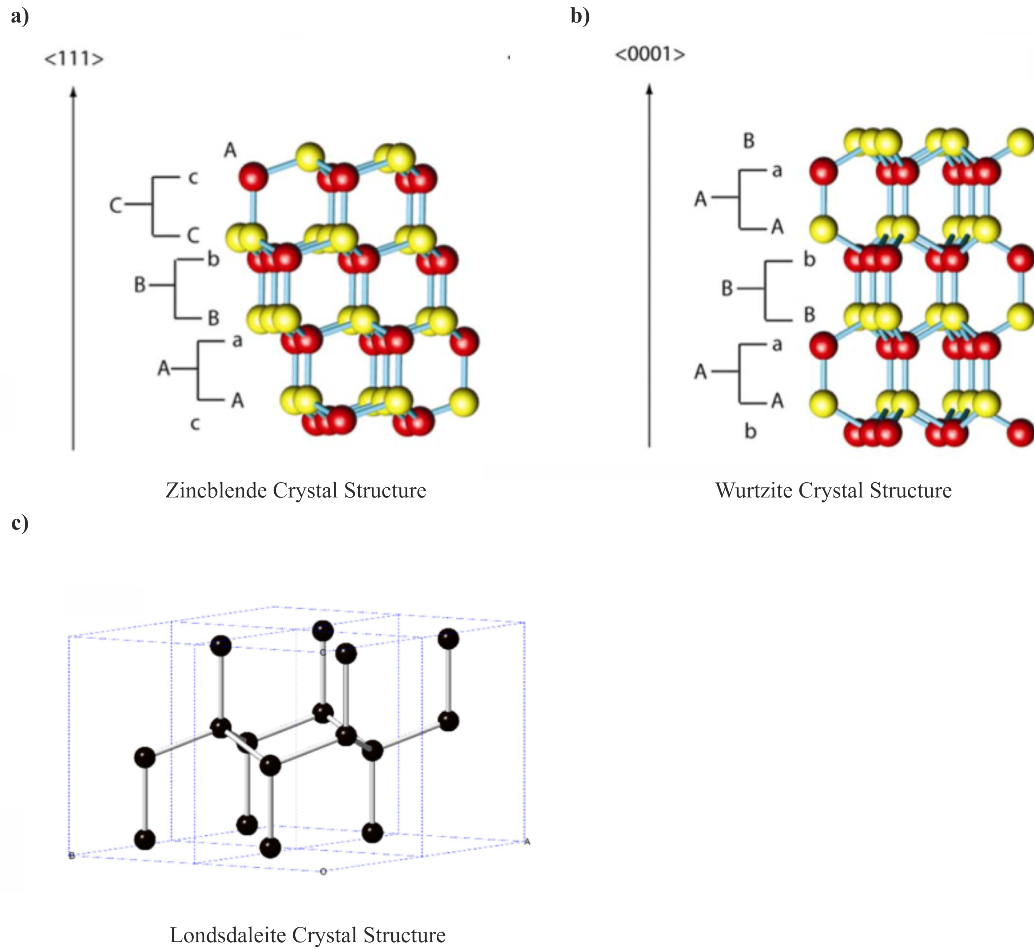

Figure 2.3: Atomic structures of a crystal in (a) zincblende phase, (b) wurtzite phase, and lonsdaleite phase: (a) and (b) are labelled with capital letters representing a bilayer which consists of two layers (small and capital letter). Each colour stands for a different kind of atom. Adapted from Refs. [48, 49].

a crystal structure which was first found in meteorites [46, 47]. So far it has not been possible to grow this structure uniformly however, except by transferring the crystal structure using an appropriate nanowire core.

2.1.3 Crystal structures

Crystal structures have a significant influence on the band structure and the optical, mechanical, thermal, and electrical properties of nanowires [50, 51, 52, 53, 54, 55]. There are many different crystal systems [56, 57, 58], but most semiconductors are in the zincblende (ZB) or wurtzite (WZ) phase. Zincblende consists of octahedral segments. It has two atoms per primitive cell and the bilayers are stacked ABCABC.

Each capital letter stands for a different bilayer. Wurtzite consists of four atoms per primitive cell and its layer structure is ABAB. It has a hexagonal cross-section [2, 59].

The lonsdaleite phase is a crystal structure which is hard to grow for materials, such as silicon and germanium, and thus not well-known. It consists of two interpenetrating hexagonal close-packed lattices [60]. It is similar to wurtzite, but there is only one species of atoms instead of two. The differences between the structures are visualised in Figure 2.3.

Semiconductors grown in bulk or as epitaxial layers can only be fabricated in a limited number of crystal phases. Nanowires offer more options because the crystal structure can be controlled better due to the high surface-to-volume ratio and the resulting strain relaxation in lattice-mismatched epitaxy.

The crystal structures of nanowires depend on many factors like nanowire diameter, growth system, growth temperature, growth rate, doping and strain [8, 61, 62, 63]. InAs, for example, changes its crystal structure differently when grown with MOVPE or MBE. MOVPE-grown InAs nanowires generally have a wurtzite structure at small diameter. For increasing diameters there is a random mixture of ZB and WZ segments until the nanowires are mostly zincblende for large diameters. In contrast, MBE-grown nanowires barely show any diameter dependence [55].

During growth, the nanowires' crystal structure can be changed between WZ and ZB because they are energetically close [12]. Therefore, stacking faults — a local interruption of the crystal structure — or the insertion of segments with a different crystal structure can occur [48]. Different stacking sequences in one wire with otherwise identical structure and composition is called polytypism. Depending on the device, number of, and control over the polytypism, it can be detrimental or beneficial. For example, it is a disadvantage if the changes in crystal structure act as scattering centres [64]. However, if controlled, polytypism can result in miniband formation [65] and twin-defect superlattices [66].

2.1.4 Doping

The tailoring described above covers only big changes in the crystal structure. However, semiconducting nanowires can also be engineered with spatially resolved insertions of single atoms. This is called doping.

Doping can be p-type or n-type. The kind is determined by the doping material and the substituted atom of the main material. In GaAs, for instance, Si can either be a p- or an n-type dopant, depending whether it replaces a Ga or an As atom [67]. P-type doping causes an abundance of holes, because atoms with fewer electrons than the main material are inserted. n-type doping causes an abundance of electrons. The incorporation of dopants can be done ex-situ and in-situ. The spatial resolution is larger and more material dependent for ex-situ, while the in-situ method can change the growth rate and the material composition [8, 67]. For example, Sb doping has a positive influence on the nanowire growth enabling a better control over the crystal structure, and thus reducing the stacking faults in nanowires and increasing the electron mobility [68, 69, 70].

Furthermore, doping can occur unintentionally during growth. For example, in a MOVPE system carbon will be inevitably incorporated during fabrication [61]. If a core-shell nanowire is grown, more dopants, such as carbon or phosphorus atoms, are incorporated during shell growth than during core growth [71, 66].

An extensive knowledge about semiconductor doping is important because of its significant influence on nanowire conductivity. It has been demonstrated that doping can affect nanowires more than the surface condition [72]. It can alter nanowire properties in negative and positive ways. For example, doping can increase the number of charge-carriers, but it can also enhance impurity scattering, and thus decrease carrier mobility. To prevent this, the wires can be grown modulation doped. Herewith, the dopants are inserted into the nanowires' shell which has a higher bandgap than the core. The charge-carriers from the dopants move to the nanowire core and contribute there to a higher photoconductivity. This way the charge-carriers are not negatively affected by dopants as scattering centres, but the photoconductivity is enhanced [42].

Not only the position but also the concentration of doping determines the impact on the electrical properties of the nanowires. Light doping causes a light overlap between electron states leading only to an increased conductivity. Heavy doping, however, induces metal-like behaviour [73]. Therefore, doping is commonly used to increase the conductivity of semiconductors. The different kind of dopants can be distinguished by their characteristic temperature-dependent behaviour. At very low temperatures, the carrier density is the lowest. The carriers originating from the doping are frozen out and cannot contribute to the free carrier density. If the temperature is higher than the freeze-out temperature, which is different for each dopant, the charge-carrier density increases suddenly. For medium temperatures, the density stays constant because the dopants have no abundant carriers anymore. For higher temperatures, the carrier density increases again with temperature due to thermally activated carriers from the intrinsic semiconductor [74, 75].

2.2 Semiconductors

2.2.1 Basics

Semiconductors (SC) are materials which have one almost-filled energy band and one almost-empty energy band at room temperature. They behave similarly to metals at high temperatures and similarly to insulators at low temperatures [56]. The transition from semiconductor to insulator is not sharp and there are many definitions to distinguish them. In semiconductors, the highest occupied energy band is called the valence band, while the highest unoccupied one is called the conduction band. The energy difference between these two is called bandgap, which determines many of the properties of semiconductors. For example, the bandgap defines the photon energy at which the material emits or absorbs radiation. This thesis concentrates on semiconductors that emit photons in the infrared part of the electromagnetic spectrum. This means that their bandgap is between 1.8 eV and 0.4 meV (700 nm - 3000 μm). The IR region can be divided into three categories: near-infrared (1.8 eV - 0.6 eV/700 nm - 2 μm), mid-infrared (600 meV - 60 meV/2 μm - 20 μm), and far-infrared (60 meV - 0.4 meV/20 μm - 3000 μm) [76, 77].

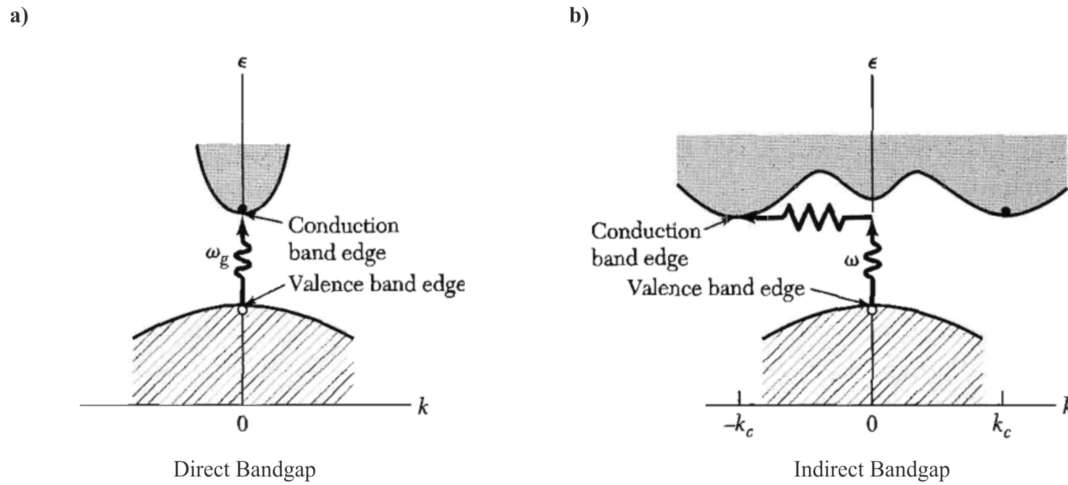

Figure 2.4: Schematic illustration of (a) direct and (b) indirect bandgap. For a direct bandgap, the maximum of the valence band and the minimum of the conduction band are at the same wave vector. For the indirect case, they are not. Therefore, recombination of charge-carriers takes longer. Adapted from Ref. [78].

Semiconductors can be classified in many different ways: intrinsic/doped, direct bandgap/indirect bandgap, and crystalline/amorphous.
These classifications are briefly addressed in the following. Intrinsic semiconductors are undoped. Therefore, the free charge-carriers are created by lifting electrons into the conduction band by some kind of excitation, such as optical or thermal excitations. Doped semiconductors have added atoms with a different number of valence electrons than the pure semiconductor. Therefore, free charge-carriers are available without excitation. Doping can improve the conductivity, but it can also increase scattering and thus harm electronic device performance.

Semiconductors can have direct or indirect bandgaps, which are both illustrated in Figure 2.4. This property describes how the valence band and conduction band changes in relation to each other at different positions in k-space: the Fourier-transformed space of the atoms' position, describing the space of momenta. For a direct bandgap material, the minimum of the conduction band is directly above the maximum of the valence band and photons with an energy larger than, or the same as, the bandgap can be absorbed and excite an electron from the valence into the conduction band. This negatively-charged electron leaves an empty space in the valence band, which can be treated like a positively-charged quasiparticle, called

a hole. In an indirect bandgap semiconductor, the two extrema are separated in k-space. If a photon is absorbed or created around the bandgap energy, a third particle needs to be involved for momentum conservation. A phonon, which is a lattice vibration, is usually involved in this process. However, a two-particle transition (as occurs for a direct bandgap) can also take place with an indirect bandgap, if the energy of the excitation photon is bigger than the gap between valence and conduction band at the wave vector of the indirect gap. The probability of a three-particle transition is smaller than that of a two-particle transition because more particles are involved. Therefore, direct bandgap materials are more efficient for optical or optoelectronic applications.

The bandgap only describes a small area of a semiconductor's energy bands, which consist of multiple bands. The energy band structure of a semiconductor depends on many factors like crystal structure, lattice constant, chemical species, bonding, bonding lengths, electronegativity, stiffness and elasticity. If dopants are added, they create their own flat energy band, which can be within the bandgap or in any energy bands. This also alters the absorption and emission spectra of the semiconductor.

Once the electrons are in the conduction band, they move around and can create a current, if a voltage is applied. However, they can also recombine using different paths. These different recombination mechanisms will be explained in more detail in the following section. A more detailed discussion of fundamental semiconductor physics can be found in various works on semiconductors, e.g. Refs. [56, 74, 75, 78].

2.2.2 Recombination mechanisms

The charge-carriers in a semiconductor can decay radiatively or non-radiatively through different recombination processes. Non-radiative decays, which are often detrimental for the performance of optoelectronic devices, can be caused by defect mediated or Auger recombination, while radiative decays are mostly caused by bimolecular recombination.

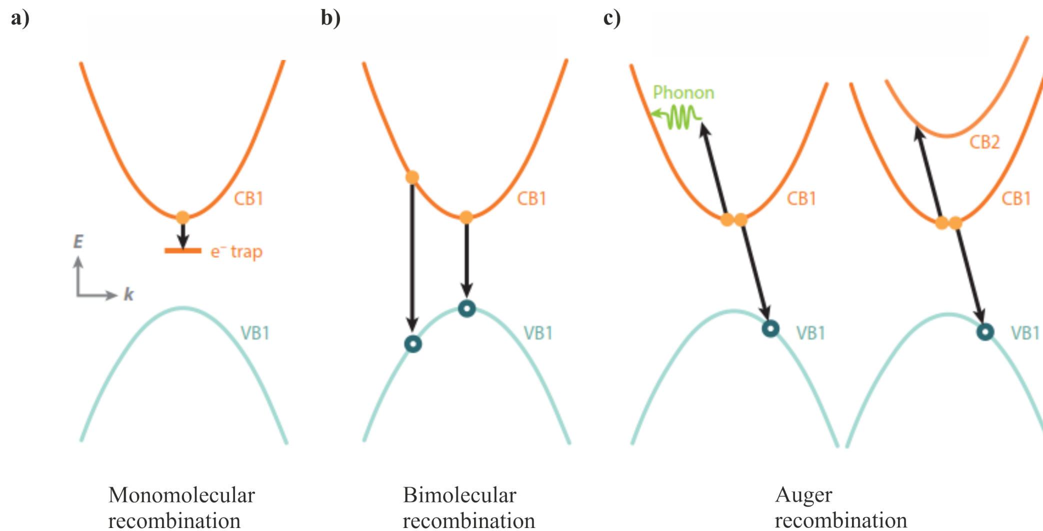

Figure 2.5: Schematic illustrations for different recombination mechanisms in semiconductors. (a) Monomolecular recombination: an electron or hole is captured by an energy state outside the SC's energy bands. This state is called a trap and can occur due to impurities or doping. It is mostly non-radiative (b) Bimolecular recombination: electron and hole recombine. Their energy is usually released radiatively by creating a photon. (c) Auger recombination: electron and hole recombine non-radiatively. Their energy is either transferred to the atom lattice creating phonons or to a third charge-carrier, which is then lifted to a higher energy band. Adapted from Ref. [79].

Monomolecular recombination

Monomolecular recombination is a decay process involving only one carrier, as shown in Figure 2.5a. It can be both radiative or non-radiative depending on the exact process. For example, the recombination of an exciton — a quasiparticle consisting of an electron and a hole attracted to each other due to electrostatic force — is monomolecular and radiative.

Another monomolecular process is defect mediated charge-carrier recombination which is assisted by recombination centres created by dopants, impurities, defects and surface states. The centres act as traps, where electrons or holes can be captured prior to recombination. The capture rate is determined by the capture cross-section of traps, trap density and thermal velocity. The recombination itself can be either radiative or non-radiative depending on the type of recombination centre [80]. Defect mediated recombination is highly dependent on the material and growth conditions which determine the density and strength of traps.

Bimolecular recombination

Bimolecular recombination is a two-particle, radiative process (Figure 2.5b). It is highly desirable for many efficient optoelectronic devices [81]. During the recombination, an electron and a hole recombine and release their energy, which creates a photon. The recombination rate is determined by the probability that initial and final states are populated and the strength of coupling. Therefore, the rate is lower for indirect bandgap materials than for direct ones.

With increasing charge-carrier density, the photon energy is blue-shifted in emission and absorption spectrum. Due to the Pauli exclusion principle there is a finite number of states to be occupied. Therefore, electrons fill up the conduction band, once the lower states are populated. Consequently, the charge-carriers, which recombine radiatively, transfer more energy to the created photon. This shift is called Burstein-Moss effect [82].

Before carriers can recombine, they first need to be optically excited to the conduction band. The photons are absorbed and give their energy to the electron which changes its energy band. For effective absorption, the photons need an energy higher than the bandgap. Below that, the electrons cannot reach the conduction band in a linear absorption process. If the photons' energy is higher than the bandgap, the electrons relax to the lowest unoccupied state by transferring their excess energy to phonons. This heats up the sample.

Auger recombination

Auger recombination is always a non-radiative three particle process (Figure 2.5c). An electron and hole recombine and instead of creating a photon, the excess energy is transferred to a third particle, which is elevated to a higher energy band or vacuum, or causes a lattice vibration. This process strongly depends on the band structures because energy and momentum must be conserved. It is highly sensitive to the carrier density due to the involvement of three particles [83].

2.2.3 Recombination rate model

A rate equation model can be used to describe charge recombination in semiconductors. The different recombination mechanisms together determine the development of the charge-carrier density n with time t after photoexcitation in a material. The time dependence can be described by

$$\frac{dn}{dt} = -k_1 n - k_2 n^2 - k_3 n^3. \tag{2.1}$$

The intrinsic electron density n is as big as the intrinsic hole density p. Therefore, n can be exchanged with p [84]. Each term stands for a different recombination process. The first one accounts for monomolecular decay. The recombination rate coefficient k_1 with the unit 1/s describes the quantity of this decay. If the charge-carrier density is increased, the traps are saturated and bimolecular decay starts to dominate. This recombination is determined by the bimolecular rate constant k_2 [cm^3/s]. Auger processes are represented by the Auger rate constant k_3 [cm^6/s] and are proportional to the charge-carrier density raised to the third power. Therefore, Auger recombination dominates at very high carrier densities.

Consequently, the radiative efficiency, which is regulated by the ratio of recombination processes, significantly depends on the charge-carrier density. An example of this dependence can be seen in Figure 2.6 for the example of the perovskite film formamidinium tin triiodie ($FASnI_3$). This figure distinguishes between recombination including and excluding radiative monomolecular recombination processes. If all monomolecular recombination is non-radiative, the radiative efficiency is zero for low charge-carrier densities, but increases significantly when the bimolecular recombination regime is reached. For high charge-carrier densities the efficiency decreases again due to non-radiative Auger recombination. However, this curve differs, if the monomolecular recombination processes are not only non-radiative, but radiative. Then there is a constant radiative efficiency even at low charge-carrier densities and its value increases faster at higher charge-carrier densities.

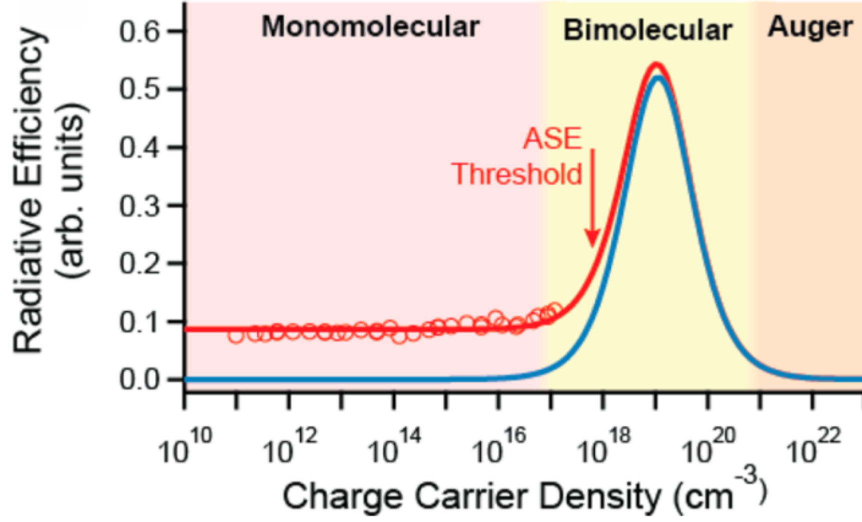

Figure 2.6: The radiative efficiency of a perovskite film is plotted against the charge-carrier density for 13 orders of magnitude. The different recombination mechanisms (monomolecular, bimolecular, Auger) are marked. The blue line is the radiative efficiency calculated only with non-radiative monomolecular recombination. The radiative monomolecular component is also considered for the calculation of the red line. The threshold of the amplified spontaneous emission (ASE) is marked by the arrow. Adapted from Ref. [80].

Often the decay of photoexcited charge, which can be measured with PL or THz spectroscopy, is fitted with an exponential decay function to analyse the time dynamics of the sample.

$$f(t) = a \cdot e^{(-b \cdot t)} \tag{2.2}$$

where a represents the initial number of carriers, and b is the inverse of the carrier lifetime. However, the exponential fit only considers monomolecular decay. The bimolecular rate constant and Auger rate constant are approximated as zero. These assumptions are valid for scans at low charge-carrier densities. If the decay cannot be monoexponentially fitted anymore, equation (2.1) should instead be used because all recombination mechanisms are considered. Because there are four parameters to be determined (n, k_1, k_2, k_2), it is beneficial to globally fit multiple decay transients from the same sample at different photoexcitation fluences. The recombination rate coefficients are constant at different fluences. They only change with temperature, while the charge-carrier density also varies with excitation power.

A drawback of this method is the fact that radiative monomolecular recombination caused by doping is not considered. However, this process can have a large influence on the radiative efficiency, as can be seen in Figure 2.6 [80]. Therefore, the equation needs to be adapted for materials with high doping densities to

$$\begin{aligned}\frac{dn}{dt} &= -k_1^{\mathrm{nr}} n - k_2(n + n_0)n - k_3 n^3 \\ &= -(k_1^{\mathrm{nr}} + k_2 n_0)n - k_2 n^2 - k_3 n^3 \\ &= -k_1^{\mathrm{total}} n - k_2 n^2 - k_3 n^3.\end{aligned} \tag{2.3}$$

The extrinsic electron density is called n_0. For p-type doping, an extrinsic hole density p_0 needs to be included. k_1^{total} is the coefficient for all monomolecular recombination, including the non-radiative monomolecular rate coefficient k_1^{nr} and the radiative monomolecular rate coefficient $k_2 n_0$ [80, 85, 86].

2.3 Nanowire devices

The various properties of semiconducting nanowires and their nearly limitless possibilities to combine materials, doping, and crystal structures enable their fabrication and optimisation for many applications. Some nanowire devices are downscaled or improved compared to bulk devices, and some of them are only possible or efficient as nanowires. The geometries and materials used vary a lot due to the different demands of the devices. For electronic devices, such as transistors, a high mobility and one-dimensional transport is preferable. Therefore, the diameter of the nanowires should be as small as possible. However, if the wire is used for laser applications, its diameter should be at least one quarter of the emitted photon wavelength [87]. In the following, a selection of electrical and optoelectronic nanowire applications is presented. The applications were singled out because the nanowires discussed in this thesis would be ideal for them. InAsSb nanowires, which are investigated in Section 7.3, are promising for thermoelectric devices due to their high electron mobility, but low thermal conductivity [88]. They are also ideal for detectors or lasers because the bandgap can be engineered. The same applies to InAs nanowires due to their remarkable properties which are explained in Chapter

7. Also hexagonal Si and SiGe nanowires can be useful for those two types of application because they emit and absorb in the near-infrared, while bandgap of InAs and InAsSb is in the mid-infrared. Due to their compatibility with current silicon-based technology, Si and SiGe would also be beneficial for solar cells.

2.3.1 Thermoelectric devices

Thermoelectric devices convert a temperature gradient into electric current or the other way round. They are useful to provide environmentally friendly electricity by converting waste heat into energy. Despite the demand, these devices are not widely used because the efficiency for bulk devices is too low [89].

The efficiency is calculated by the figure of merit ZT,

$$ZT = S^2\sigma T/(\kappa_e + \kappa_l), \tag{2.4}$$

where S stands for the Seebeck coefficient, σ for the electrical conductivity, κ_e for the electronic thermal conductivity and κ_l for the lattice thermal conductivity. S, σ and κ_e are properties linked to each other, thus limiting the device efficiency [90]. ZT should be between 2 and 3 for applications, but it practically only reaches up to 1 for current devices [89].

In 1993 Dresselhaus and Hicks predicted an increase of ZT in lower dimensions, because the different parameters can be manipulated independently. Nanowires seem to be especially appropriate, because the large surface-to-volume ratio increases the diffusive phonon scattering rate, resulting in a higher ZT [90]. Furthermore, the peaks in the density of states resulting from the single dimension of the nanowires decrease the thermal conductivity [91]. Moreover, heterostructures, like Si nanowires with a few nm thick Ge shell, can reduce the phonon thermal conductance [89, 92].

Thermoelectric devices can be driven by two different effects: Seebeck or pyroelectric effect. The Seebeck effect describes carriers diffusing in the nanowire due to a temperature gradient, and thus causing a direct current as output. The pyroelectric effect causes a current due to spontaneous temperature fluctuations. Due to the different techniques of gaining current, the Seebeck effect is used for

constant temperature gradients and the pyroelectric effect for random fluctuations [93]. Both methods are promising for the reuse of energy, but more research is needed before the first commercial thermoelectric nanowire devices will be available.

2.3.2 Solar cells

Solar cells are a feasible renewable way to provide all of the energy needed by humanity. Commercially used Si photovoltaics reach power conversion efficiencies of around 20% [94]. The utilisation of nanowires in this area can yield higher efficiencies and reduce fabrication costs because less material is needed for the cell and the substrates are less costly. The structure of solar cells with standing nanowires benefits from reduced reflection losses compared to bulk devices due to multiple scattering events between the wires [39].

There are multiple approaches for optimising nanowire solar cells. Especially the junctions, which can be grown axially or radially, are important for efficient devices. A radial junction provides reduced reflection combined with a high light trapping rate and a radial charge separation. An axial heterostructure has the same advantages like the radial structure, but does not result in fast charge separation. Also a substrate junction or a junction created by doping is feasible [39, 94, 95]. There are also multiple solutions for fabricating low resistivity contacts. Flat-lying nanowires can be electrically connected with metal strips, but for vertical ones a transparent upper contact is needed.

2.3.3 Detectors

Photodetectors are devices used to measure radiation. Semiconductor detectors can be categorised into these primary areas based on their structure: avalanche photodiodes (APD), metal-semiconductor-metal (MSM) detectors, p-i-n detectors and metal-insulator-semiconductor (MIS) detectors.

APDs enable the detection of low-power signals through avalanche multiplication. A high voltage is applied and this accelerates the electron created by an incoming photon. When the kinetic energy of the carrier imparted to the multiplication

medium exceeds the ionization energy, another electron is created and two electrons are accelerated. This is repeated multiple times resulting in high sensitivity.

MSM detectors have two Schottky contacts at the active semiconductor region allowing only the transport of one kind of carrier. Therefore, the low capacitance and short delay of the circuit result in a high operation speed.

p-i-n detectors have a sandwich-like structure with an intrinsic semiconductor region between a p-doped and an n-doped one. Their external quantum efficiency and responsivity is higher than that on MSM [96].

Each structure has its own advantages and disadvantages. Nanowires can be beneficial for each one of them. For example, the sensitivity can be increased due to the wires' large surface-to-volume ratio [96]. The ability of nanowire devices to absorb light is not only an intrinsic material property, but can also be engineered by the size, geometry and orientation of the wires [97].

In recent research, superconducting nanowires have been exploited as photodetectors. They are sensitive to visible and infrared wavelengths and can be used as single-photon detectors with recovery times and timing precision orders of magnitude faster than bulk superconducting detectors. The functional principle is explained in the following.

The nanowire is cooled below the critical temperature and reaches the superconducting state. Then a direct current is applied. It flows without resistance. When a photon hits the wire, it has enough energy to disrupt a few hundred Cooper pairs — pairs of electrons in superconductive materials — and it creates a local hotspot with an extension smaller than the nanowire. The supercurrent is forced to flow around this hotspot. Because the nanowires have a small diameter, the critical current density is reached and the superconducting state is broken, leading to a resistive barrier in the wire, thus the current is blocked. This can be detected electronically. After the dead time, once the heat dissipates, the nanowire starts superconducting again along the whole wire [98]. Depending on its diameter size, the device can be used either for single-photon (under 100 nm) or for multi-photon detection (above 100 nm) [99]. Potential applications range from optical quantum

computing and quantum key distribution over fibre temperature sensing to space-to-ground communication. For example, Takesue *et al.* [100] have successfully used a superconducting nanowire single-photon detector to detect a photon that transmitted quantum information via a 100 km long fibre.

Nanowires are particularly promising as infrared detectors. It has been shown that they can be fabricated as mid-infrared detectors without the need for cooling. This is a big advantage over the commercially available detectors, which often require cryogenic cooling [7].

2.3.4 Light emitting devices

Nanowires are not only suitable as photodetectors, but also as light emitting devices, such as nanosized LEDs [101, 102] or lasers [103, 104]. Their geometry is beneficial for these applications because their shapes make them ideal waveguides.

For example, the "top-down" etched diamond nanowires with nitrogen vacancies are better as single-photon sources than their bulk counterparts. When implemented, the photon flux for the nanowire array was increased tenfold and the excitation power was simultaneously decreased ten times compared with bulk diamond [105].

Nanowires are especially promising as lasers because the whole nanowire acts as both gain medium and cavity at the same time. Furthermore, nanowire lasers can be directly integrated onto computer chips enabling optical interconnects [3].

Laser is an acronym for 'light amplification by stimulated emission of radiation' [106]. It creates photons due to electrical or optical pumping. The photons oscillate in the laser cavity and create more photons, which are coherent to the seed photons, through stimulated emission. This means all photons have the same energy, momentum, polarisation and phase [107]. In order to get feedback, a gain medium and a cavity are necessary for a working laser.

Nanowires have the major advantage that the whole wire is simultaneously the gain medium and the cavity with the side facets as mirrors. Therefore, the ratio of gain medium to cavity is larger than for conventional lasers, making nanowire lasers highly efficient. Furthermore, there are barely any waveguide losses $\alpha_{\text{waveguide}}$,

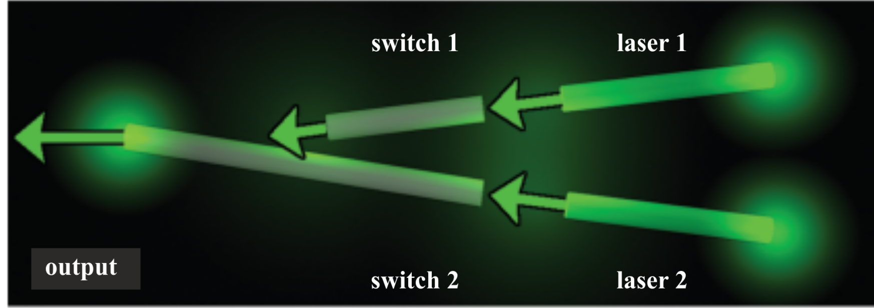

Figure 2.7: Schematic of a NAND gate built from nanowires: light from laser 1 and 2 are guided through switch 1 and 2. If one of the switches is optically excited, the light from laser 1 and 2, respectively, cannot be transmitted. To suppress the final output, switch 1 and 2 must be off. Adapted from Ref. [111].

because the light does not have to couple into the cavity. As a result, the threshold gain g_{th} of nanowire lasers is very low — as can be seen in the following equation.

$$g_{\mathrm{th}} = \frac{\alpha_{\mathrm{waveguide}}}{\mathcal{T}} - \frac{1}{2L\mathcal{T}} \ln(\mathrm{R}_1\mathrm{R}_2) \quad (2.5)$$

[87]. $\mathcal{T}$ is the confinement factor, which gives the fraction of the material gain, which amplifies the laser mode [108]. L is the nanowire length and R_1 and R_2 represent the reflectivity at each nanowire end facet. As shown by Mayer *et al.* for GaAs nanowires $\mathcal{T}$ is around 0.9 and the reflectivity of the untreated end facets is around 0.8 [87]. Nanowire lasers usually emit in a fundamental mode and the photon dynamics are ultrafast in the femtosecond to picosecond regime [109]. Furthermore, the pulses created by a pulsed nanowire laser have a coherence time of more than 40 ps [110].

Piccione *et al.* [111] demonstrated a logic NAND gate created by all-optical active switching of CdS nanowire lasers. A schematic can be seen in Figure 2.7. The light from a nanowire lasers (laser 1 and 2) is coupled into an adjacent nanowire (switch 1 and 2), which acts as waveguide and switch. If the waveguide is pumped by an external laser, the light from laser 1 and 2, respectively, is blocked. Switch 1 and 2 are coupled and have one mutual output. Only if the emitted light of both laser 1 and laser 2 are blocked, will the output be zero.

Due to the abundant possibilities of materials and material combinations, nanowire lasers have been developed from the UV regime ranging over the visible to the infrared regime [108]. However, there are still issues which need to be resolved.

It is difficult to fabricate infrared nanowire lasers due to their low bandgap and the resulting high fraction of non-radiative recombination. Furthermore, so far it has not been possible to create an electrically driven nanowire laser standing on substrate. Almost all nanowire lasers are optically driven.

It is complicated to achieve lasing using monolithically integrated nanowires because the refractive indices of the nanowires and the substrates are very similar. This problem was solved by Mayer *et al.* [3] using GaAs/AlGaAs core-shell nanowires, whose end facets have less than 1% reflectivity on a silicon substrate, for example. In order to increase the reflectivity, the silicon wafer was covered with a 250 nm thick SiO_2 layer interspersed with 80 nm thick pinholes reaching the wafer. A 80 nm thick GaAs core was then grown out of the holes by molecular beam epitaxy. Above the layer the wire is thickened to the desired diameter. SiO_2 has a lower refractive index and therefore, the reflectivity is increased and β reaches values up to 21%. Furthermore, the nanowire has a large enough diameter to guide the laser mode and the 80 nm thick core enables an electrical contact with the substrate. Work like that described above contributes to the creation of an electrically driven nanowire laser. However, a lot of research is still required.

2.4 Summary

The importance of nanowires for future technology was discussed in this chapter. Therefore, an introduction into the field of semiconducting nanowires was given. First, the different growth techniques, growth regimes, growth templates, heterostructures, doping, and crystal structures, and the possibility of nanowires to be designed and optimised for many different types of devices were summarised. Then the fundamental physics of semiconductors needed for understanding this thesis was given with the focus on different recombination mechanisms. In the end, promising areas for nanowire applications, which were connected to the research performed in this thesis, were introduced.

3
Experimental Methods

3.1 THz spectroscopy

3.1.1 Introduction to THz spectroscopy

The terahertz (THz) part of the electromagnetic spectrum is usually defined to include all frequencies between 100 GHz and 10 THz (0.4 meV to 40 meV) [112]. Scientific progress, such as quantum cascade laser and femtosecond lasers, made feasible many different applications for THz radiation, e.g. in biology, medicine and security [113].

In this thesis, THz radiation is used for THz spectroscopy which is a non-invasive, non-destructive method of investigating the charge-carrier dynamics of materials [114]. Charge species in semiconductors show a distinct response in the THz frequency regime because their energies for motions and excitations are of the same order of magnitude as for THz photons. Furthermore, THz spectroscopy achieves high temporal resolution in the femtosecond regime, enabling fast carrier dynamics to be probed. Therefore, this method enables accurate measurements of photoconductivity lifetimes, recombination rate coefficients, surface recombination velocities, scattering times, mobility, doping, and charge-carrier densities [112, 115]. More information about THz generation and detection, measurement techniques, and applications can be found in works, such as [113, 116, 117].

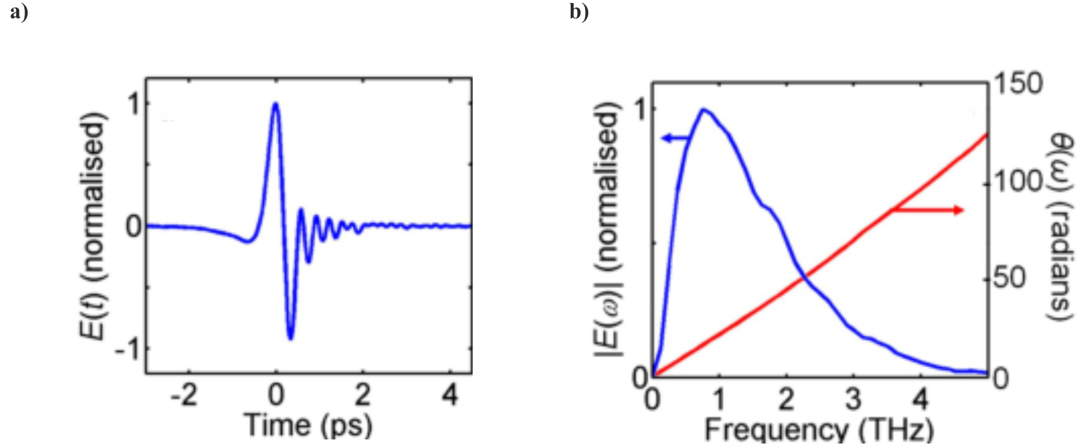

Figure 3.1: (a) Electric field of a THz pulse in the time domain and (b) amplitude spectrum E(ω) and phase $\theta(\omega)$ in the frequency domain. To obtain the spectrum in (b) a Fourier transform was applied on the signal in (a). Adapted from Ref. [112].

In the following only Optical-Pump THz-Probe (OPTP) spectroscopy and measurements on semiconducting nanowires will be discussed due to their relevance and use in subsequent chapters. It is instructive to first explain THz time-domain spectroscopy (THz-TDS), followed by the principles of OPTP spectroscopy and the OPTP setup. In the end, the analysis applied to the nanowire samples will be discussed.

THz-TDS

In THz-TDS, the time-dependent phase and amplitude of the electric field E of a short THz pulse is measured. An example of such a pulse is given in Figure 3.1a. This signal can be Fourier-transformed into the frequency domain, see Figure 3.1b. Then this amplitude spectrum can be used to determine electrical properties, such as the momentum scattering time and charge-carrier mobility of the sample. The simultaneous measurement of amplitude and phase enables the analysis of more parameters than if only the squared amplitude of the signal were recorded.

In THz-TDS the THz pulse is transmitted through the sample and then detected. During transmission, the pulse is delayed and partially absorbed by the sample. Any changes in the transmitted pulse therefore contain information about the sample. To calibrate the system, a reference pulse $E_{\mathrm{ref}}(t)$ is measured, which has

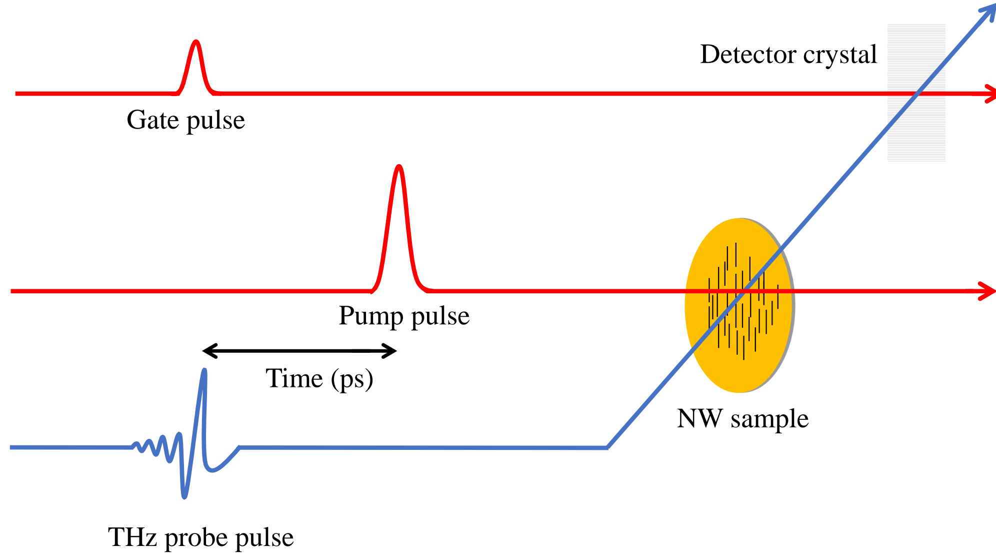

Figure 3.2: Schematic illustration of an OPTP system: a THz pulse is transmitted through a sample which has been optically excited by a pump pulse. The transmitted THz signal is then detected by interaction with the gate pulse.

been transmitted through the same path, but without the sample. Therefore, the transmission $T(\omega)$ can be calculated by

$$T(\omega) = \frac{E_{\text{sample}}(\omega)}{E_{\text{ref}}(\omega)} \tag{3.1}$$

where $E_{\text{sample}}(\omega)$ is the pulse transmitted through the sample in the frequency domain, while $E_{\text{ref}}(\omega)$ is the reference pulse in the frequency domain. The THz signal cannot be detected directly. Therefore, a gate-pulse is used to measure it by converting it into an electric signal. The delay between the gate pulse and the THz pulse can be varied in order to probe all of the time-dependent THz pulse (see Figure 3.2).

Principles of OPTP spectroscopy

Optical-Pump THz-Probe (OPTP) spectroscopy is a pump-probe spectroscopic method probing the optically excited charge-carriers in a material. It is similar to THz-TDS, but the charge-carriers of the sample are not in equilibrium. A simple schematic showing the principles of this system can be seen in Figure 3.2. An additional optical pump pulse arrives before the THz pulse. The time

between the optical pump and the THz probe pulse can be delayed enabling measuring time-dependent charge-carrier dynamics. The charge-carrier density is higher than in THz-TDS due to prior optical pumping. Therefore, more THz radiation is absorbed by the sample. To analyse the data, the change of THz transmission ΔT is given in comparison to the THz signal T of the same sample in equilibrium. The THz pulse probing the photoexcited sample is $E^{\text{on}}_{\text{sample}}$ and the one for the unexcited sample $E^{\text{off}}_{\text{sample}}$.

$$\frac{\Delta T(\omega)}{T(\omega)} = \frac{\Delta E(\omega)}{E(\omega)} = \frac{E^{\text{on}}_{\text{sample}} - E^{\text{off}}_{\text{sample}}}{E^{\text{off}}_{\text{sample}}} \tag{3.2}$$

$\frac{\Delta T(\omega)}{T(\omega)}$ is directly proportional to the photoinduced change in the conductivity $\Delta\sigma(\omega)$.

3.1.2 Optical-Pump THz-Probe setup

In the following, the OPTP system which was used for the measurements in this thesis will be introduced and discussed. A sketch of this system can be seen in Figure 3.3.

All three pulses used for the THz spectroscopy were generated by a 800 nm (1.55 eV) centre wavelength output of a Spectra-Physics Spitfire Ti:Sapphire regenerative amplifier, which was pumped by a 527 nm (2.35 eV), 20 W Empower laser and seeded by the 800 nm (1.55 eV) output from a Spectra-Physics Mai Tai. The amplifier creates pulses with a duration of 35 fs and a power of around 4 W at a repetition frequency of 5 kHz. Each pulse is separated into different paths by beamsplitters.

One path creates the THz pulse. For that, the optical laser pulse is sent through a spintronic emitter generating a THz pulse, the bandwidth of which is larger than 6 THz in the configuration used for this thesis. A spintronic emitter consists of a ferromagnetic (FM) and a non-ferromagnetic (NM) metal thin film. An external magnetic field of around 10 mT is applied, magnetising the ferromagnetic layer. When an optical pulse from the amplifier illuminates the spintronic emitter, electrons are excited above the Fermi energy and a spin current is created perpendicular to the layers due to the different transport properties of the layers. Because the optical excitation is only 35 fs long, the ultrashort transverse charge current emits

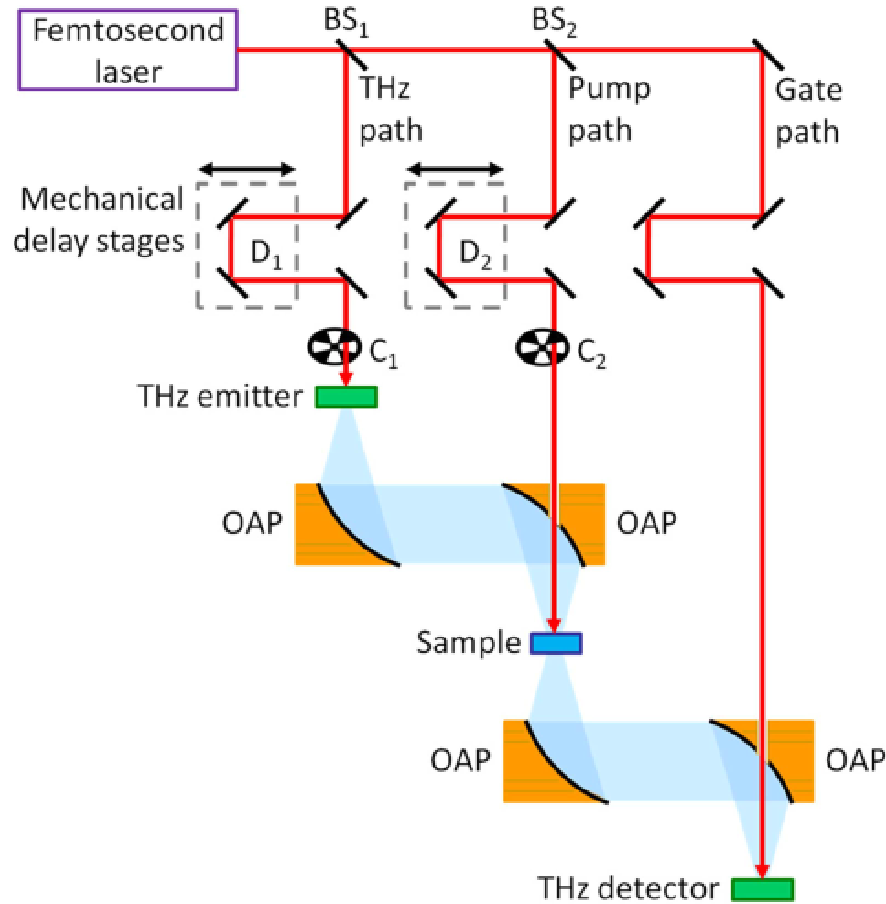

Figure 3.3: Diagram of the OPTP system. BS stands for beamsplitter, D for delay stage, C for chopper, and OAP for off-axis parabolic mirror. Adapted from Ref. [112].

a THz electromagnetic pulse which is polarised perpendicular to the propagation axis and external magnetic field. The spintronic emitter is superior to other THz generation methods due to a bandwidth of up to 30 THz, its high field amplitude, flexibility, scalability and cost [118, 119, 120].

The optical pump pulse has the same polarisation as the THz pulse. Its power is changed with neutral density filters. The full width at half maximum (FWHM) at the sample is *circa* 10 mm, while that of the THz beam is around 1-2 mm. The difference in FWHM enables a homogeneously excited sample to be probed. To excite a sample, the photon energy needs to be larger than the bandgap of the sample. If the bandgap of the sample is larger than the laser energy of 1.55 eV, the energy of the pump pulse is doubled to 3.10 eV by a BBO crystal.

The THz signal is detected by electro-optic (EO) sampling. It is based on a

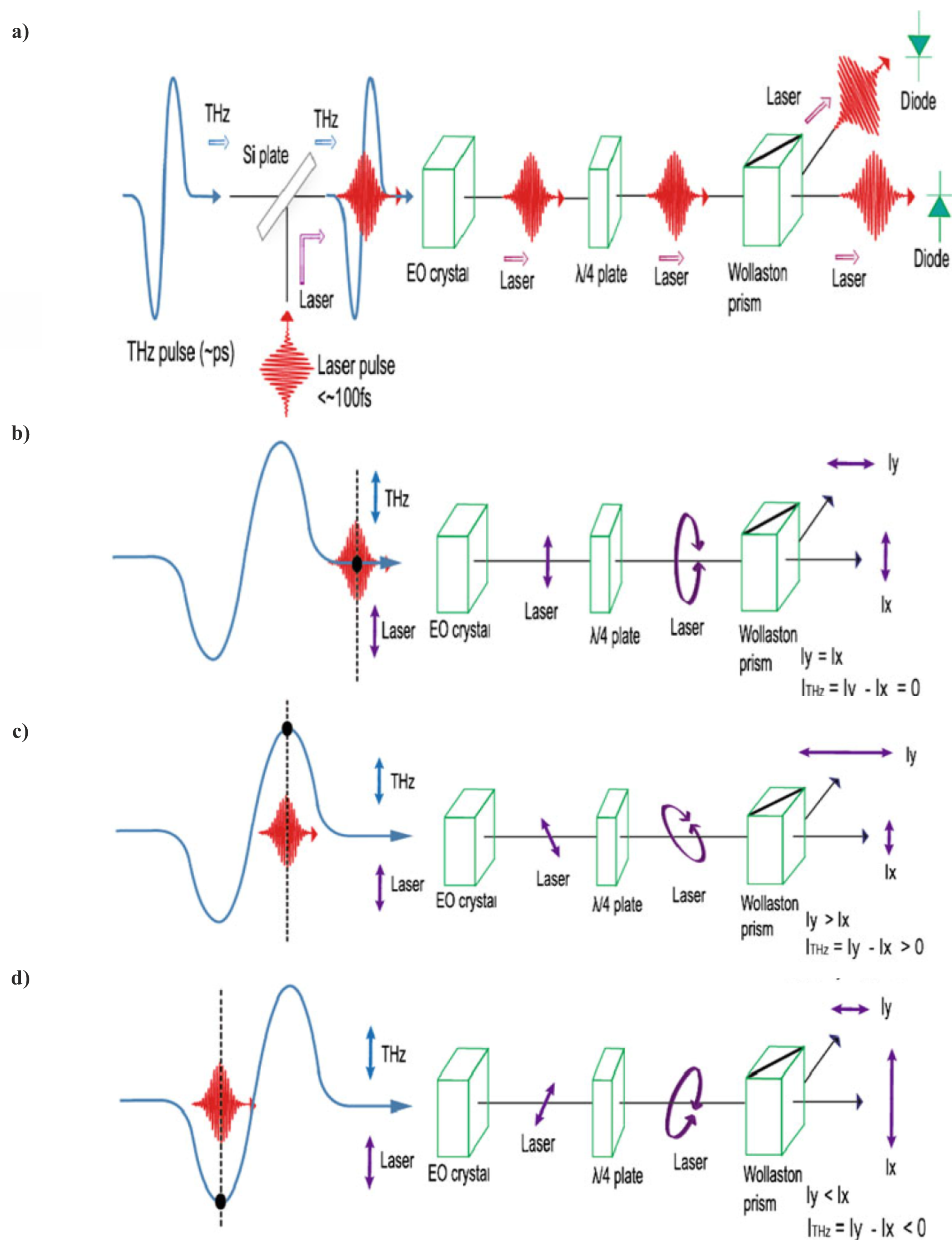

Figure 3.4: Principles of THz detection with electro-optic sampling explained (a) in general and in three different specific cases: (b) gate pulse arrives before the THz pulse, (c) gate pulse arrives at maximum of THz pulse, and (d) gate pulse arrives at minimum of THz pulse. Adapted from Ref. [121].

second-order nonlinear effect in anisotropic crystals which lack inversion symmetry. The detection method is triggered by the optical, linearly polarised gate beam. As shown in Figure 3.4a the beam transmits through the EO crystal, then through a quarter-wave plate. Afterwards the light passes a Wollaston crystal, which spatially divides the photons according to vertical and horizontal polarisation. The parted beam is then detected by two balanced photodiodes. The difference between these two signals is used to measure the THz pulse.

Before the start of a scan, the detection system needs to be calibrated and balanced, as shown in Figure 3.4b. Without the influence of THz radiation, the measured signal, which is the difference between both photodiode measurements, must be zero. Therefore, the quarter-wave plate is turned, until the linearly polarised laser light is circular polarised, consisting of equally strong vertical (lx) and horizontal (ly) linear polarisation. Consequently, the measured signal is zero.

If the THz beam hits the EO crystal, the electric field of the photons induces birefringence in the crystal. This changes the refractive indices experienced by the ordinary and the extraordinary ray. Therefore, the polarisation of the gate beam changes and is not circular but instead elliptically polarised after the quarter-wave plate. Elliptical polarisation can be divided into time-dependent uneven horizontal and vertical linear polarisation. Consequently the net signal measured is not zero anymore. The polarisation and propagation of the beam is shown in Figure 3.4c.

At the position of the EO crystal, the FWHM of the THz beam is kept larger than the beamwidth of the gate pulse to ensure a homogeneous birefringence in the crystal. The gate pulse ($\sim 35\,\text{fs}$) is much shorter than the picosecond-long THz pulse. Therefore, the gate pulse duration limits the temporal resolution. Furthermore, it is possible to measure the form of the THz pulse by changing the time delay between the gate and the THz beam, as can be seen in Figure 3.4d. (110) ZnTe and (110) GaP crystals were used as EO crystals for the OPTP system operated in this thesis. The (110) GaP crystal measures a larger THz bandwidth, but the detected signal is smaller. ZnTe achieves a higher signal due to a stronger second-order nonlinear

effect, but a lower bandwidth because the mismatch between the refractive indices of the ordinary and extraordinary axis is bigger than for the GaP crystal [122, 123].

During OPTP spectroscopy, the undisturbed gate beam is measured continuously as a reference signal. Therefore, half of the THz pulses are blocked by chopper 1 which is in front of the sample box. It is running at a frequency of 2.5 kHz. Furthermore, the THz signal needs to be detected for a photoexcited and an unexcited sample. Thus, there is a second chopper with a frequency of 1.25 kHz in the pump beam in front of the sample box.

In summary, due to the two choppers, four different pulses are measured to obtain T and ΔT. They are called:
A: THz pulse off & Pump pulse off
B: THz pulse on & Pump pulse off
C: THz pulse off & Pump pulse on
D: THz pulse on & Pump pulse on
From these measured signals T and ΔT can be calculated by

$$\begin{aligned} T &= \frac{(A-B)+(C-D)}{2} \\ \Delta T &= (A-B)-(C-D) \\ \frac{\Delta T}{T} &= 2\frac{(A-B)-(C-D)}{(A-B)+(C-D)} \end{aligned} \tag{3.3}$$

All measurements are performed in vacuum to avoid sharp absorption lines caused by THz absorption by water vapour present in air and to prevent the creation of plasma and cause damage to the sample. Furthermore, two linear delay stages are implemented in the system — one in the THz path and one in the pump path. They can be changed independently enabling two different kinds of scans.

THz photoconductivity spectra are measured while the THz path is changed, but the pump path is kept constant. Therefore, the whole THz pulse is characterised. Photoconductivity decays are measured at the maximum peak of the THz pulse with changing time delay between THz and pump pulse. The two measurement techniques and the analysis of THz spectroscopy on nanowires will be discussed in more detail in the next section.

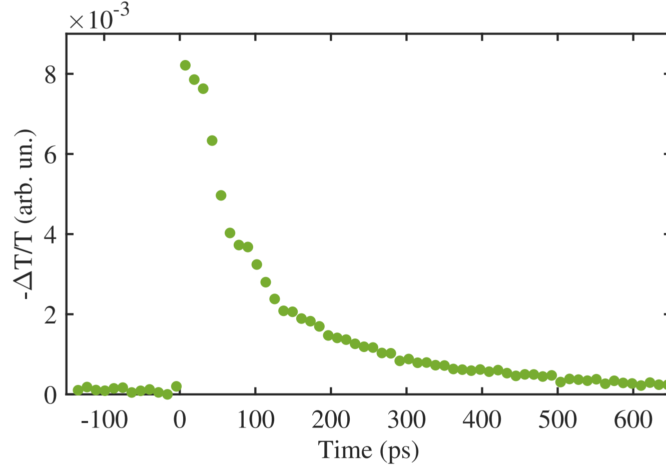

Figure 3.5: Photoconductivity decay of InGaAs nanowires at 148 μJ cm^{-2} measured with THz spectroscopy.

3.1.3 Data analysis of nanowire samples

OPTP spectroscopy is useful to extract the electrical properties, and radiative and non-radiative lifetimes of nanowires without the usage of contact electrodes in a non-invasive, non-destructive way. The nanowires cannot be measured on the growth substrate with OPTP spectroscopy because the substrate would absorb most or all of the THz radiation and interfere with the signal from the nanowires. Therefore, the nanowires need to be transferred onto a substrate which is transparent to THz radiation. In the research described in this thesis they are moved to a quartz disc covered in parylene C. Furthermore, nanowires are strongly polarisation dependent due to their inhomogeneous geometry. The maximum signal is achieved when all nanowires are aligned parallel to the electric field of the THz pulse. With this arrangement, the carriers can move along the length of the nanowire and are not confined by the wire's limited lateral dimensions [124].

Photoconductivity decays

Because the optical paths of the THz pulse and the pump pulse can be changed separately in the OPTP setup, two different types of scans can be performed: photoconductivity decays and photoconductivity spectra. Photoconductivity decays investigate the THz signal as a function of time after photoexcitation and thus the

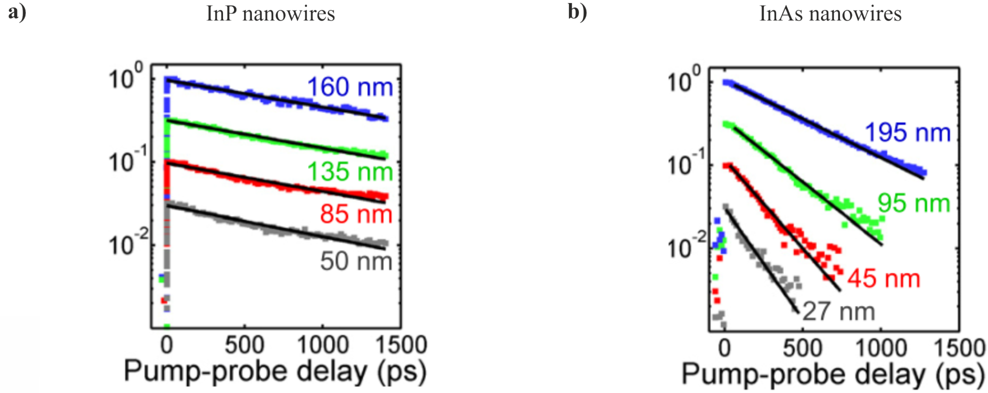

Figure 3.6: Diameter dependent photoconductivity decays for (a) InP nanowires and (b) InAs nanowires measured at $10\,\mu\mathrm{J\,cm^{-2}}$. The photoconductivity lifetimes of InP stay constant independent of diameter (1.18 ns, 1.27 ns, 1.30 ns and 1.34 ns for increasing diameters) and has a low surface recombination velocity of 170 cm/s. In contrast, the lifetimes of InAs increase significantly with diameter (200 ps, 290 ps, 470 ps, 660 ps), and thus the surface recombination velocity is 3×10^3 cm/s. Adapted from Ref. [125].

time-dependent charge-carrier dynamics. After the photoexcitation, the charge-carriers decay over time. Therefore, less THz radiation is absorbed by the sample and the THz signal increases. During the measurement, the path of the pump pulse is altered while the THz pulse is fixed at its maximum signal position, in order to achieve the optimal signal.

An example of photoconductivity decay is given in Figure 3.5. To depict the graph like a decay spectrum, despite an increasing signal over time, the negative value of $\Delta T/T$ is taken. The time is set to be zero when THz and pump pulse overlap and $-\Delta T/T$ is maximal. Negative times indicate that the pump pulse arrives at the sample before the THz pulse. The signal is zero under these circumstances.

Photoconductivity decays enable the extraction of the photoconductivity lifetimes of materials, and the calculation of the recombination rate coefficient for monomolecular, bimolecular and Auger recombination by fitting the data with the recombination rate model as described in Section 2.2.3. It is also possible to extract the nanowires' surface recombination velocity, which is an important parameter for nanowire devices due to their high surface-to-volume ratio.

The surface recombination velocity describes the influence of a semiconductor's surface on the charge-carrier decays by quantifying the speed of carrier recombination

on the surface. A low value, like for InP nanowires (170 cm/s), shows that nanowire properties are not-strongly dependent on its surface. Therefore, the photoconductivity lifetimes stay constant with changing diameters and surface-to-volume ratio, respectively. In comparison, InAs nanowires have a high surface recombination velocity of 3×10^3 cm/s [125]. Therefore, their lifetime decreases with smaller diameters, as can be seen in Figure 3.6, because the surface-to-volume ratio increases with shrinking diameter d. Consequently, surface effects get more prominent. Due to the diameter dependence, the surface recombination velocity S can be calculated by measurements of the lifetime with

$$\frac{1}{\tau} = \frac{1}{\tau_{\text{volume}}} + \frac{4S}{d}. \tag{3.4}$$

τ_{volume} represent the lifetime of the bulk material and τ the lifetime of the whole sample.

THz photoconductivity spectra

THz photoconductivity spectra are the second type of measurements which can be performed with OPTP spectroscopy. The delay between the THz pulse and the pump beam is fixed, but the delay between the THz pulse and gate pulse is altered. Therefore, the THz pulse is measured time-dependently. An example of the pulse can be seen in Figure 3.1.

Photoconductivity spectra are a powerful tool and many parameters, such as charge-carrier density, doping density, scattering time, mobility, and dielectric constant, can be extracted from them. In order to extract these values, the THz signal needs to be Fourier-transformed from the time domain into the frequency domain. This enables the calculation of the nanowires' change in photoconductivity with frequency.

$$\Delta\sigma_1(\omega) = -\frac{\epsilon_0 c(1+n_s)}{d}\frac{\Delta T}{T} \tag{3.5}$$

Where ϵ_0 stands for the vacuum permittivity, c for the speed of light, n_s for the refractive index of the substrate and d for the thickness of the sample. For nanowires, the thickness can be replaced by their diameter because it is assumed that there is

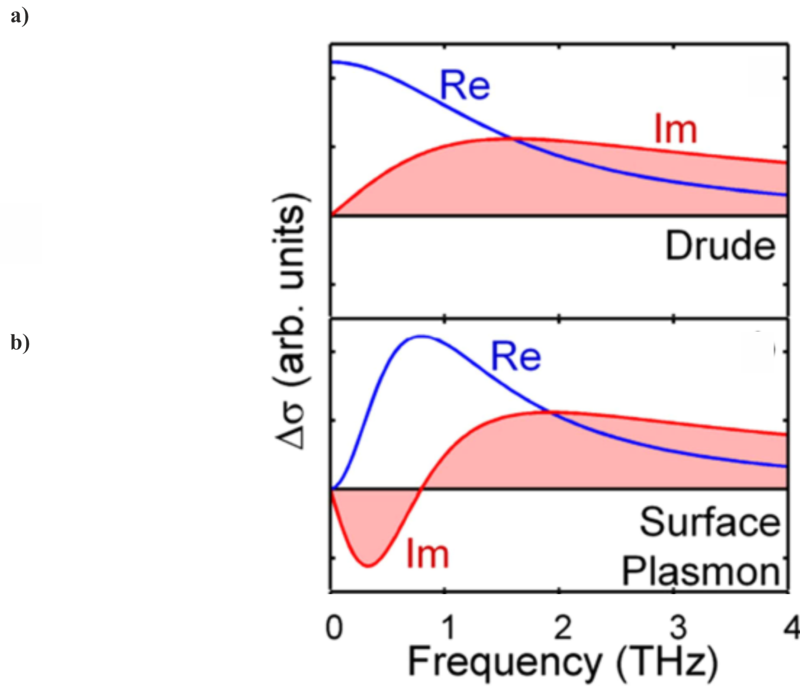

Figure 3.7: Real (blue) and imaginary (red) photoconductivity calculated using (a) the Drude model and (b) the surface plasmon model. Adapted from Ref. [112].

only one layer of wires on the substrate. A derivation of this equation can be found in paper [112]. To extract more information from the data, the photoconductivity spectra need to be fitted by an appropriate model.

Drude model

A common model for fitting the complex conductivity of semiconductors is the Drude model. It assumes that the movement of free charge-carriers is controlled by the alternating electric field of the THz pulse. The conductivity can be calculated by

$$\sigma(\omega) = \frac{ne^2}{m^*}\frac{i}{\omega + i\gamma}, \tag{3.6}$$

where n represents the charge-carrier density, e the electronic charge, m^* the effective mass of the carriers, and γ the momentum scattering rate of the carriers. The real and imaginary conductivity calculated from experimental data using this model is shown in Figure 3.7a.

This model describes bulk semiconductors very well, but it does not fit for semiconducting nanowires, which behave as shown in Figure 3.7b. The Drude model is only a simple classical model and does not account for several transport

phenomena in nanowires, such as backscattering of carriers on nanowire surfaces, carrier localisation, or the polarisability of nanowires [112].

Plasmon model

In contrast, the surface plasmon model fits the nanowires' conductivity accurately (Figure 3.7b). It is a generalised version of the Drude model. When an external electrical field is applied, the electrons and holes move to opposite sides, causing a majority of either negatively or positively charged carriers on each nanowire end. Consequently, an electric dipole and a depolarisation field, which is opposite to the external electric field, are created. Due to the two electric fields, the charge carriers oscillate in the nanowire. This response alters the equation from the Drude model equation (3.6) to

$$\sigma(\omega) = \frac{ne^2}{m^*}\frac{i\omega}{\omega^2 - \omega_0^2 + i\omega\gamma}. \tag{3.7}$$

The new parameter ω_0 is introduced for the surface plasmon model. It is the resonant frequency of the oscillating systems with the THz electric field and the depolarisation field as driving forces. The resonant frequency is shifted to higher values with increased excitation power because

$$\omega_0 = \sqrt{g\frac{ne^2}{\epsilon_0 m^*}}, \tag{3.8}$$

where g is a geometrical factor [112].

The mobility μ can be determined with

$$\mu = \frac{e}{m^*\gamma} \tag{3.9}$$

To extract the exact value for the photoconductivity rather than just its difference, an effective medium theory, like the Maxwell-Garnet or the Bruggeman theory, needs to be applied. More information about these can, among others, be found in [112].

Refractive index change of the sample due to photoexcitation

Photoconductivity decays and photoconductivity spectra can also be combined in a two-dimensional measurement by using both stages at the same time, to investigate the photoconductivity for different delays after photoexcitation.

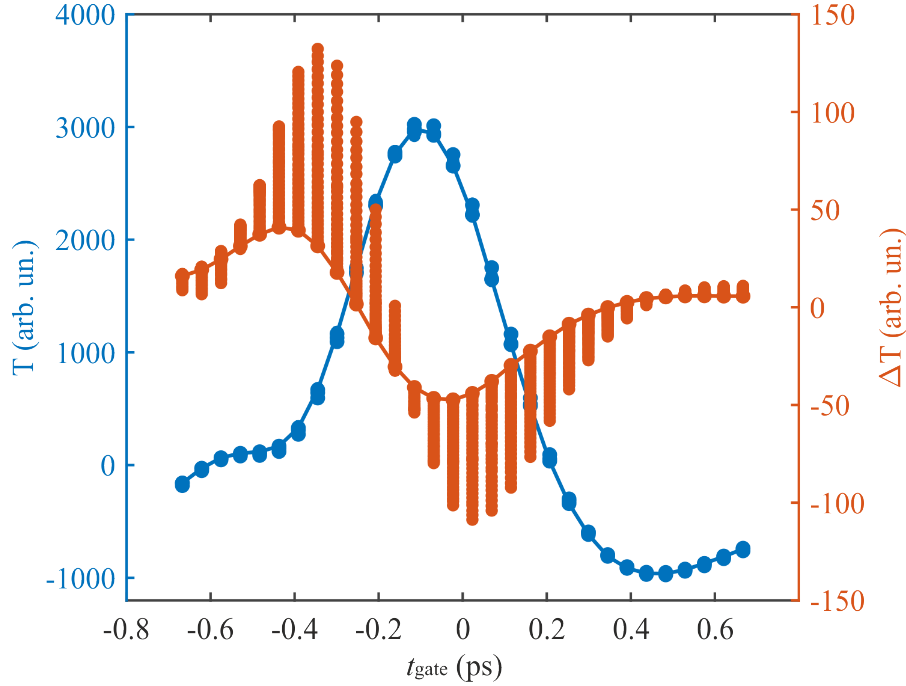

Figure 3.8: THz signal (blue) and ΔT (red) for different time delays t_{gate} between gate and THz pulse. Multiple values at the same x-coordinate were measured at different time delays between THz and pump pulse. The refractive index of the sample changes for higher charge-carrier densities and shorter time delays between THz and pump pulse. Therefore, the THz pulse gets delayed in relation to the gate pulse.

For example, a two-dimensional scan performed on InP nanowires is shown in Figure 3.8. This plot demonstrates the influence of the fluence-dependent refractive index of the sample on the THz signal. THz transmission T (blue dots) and the photoconductive change ΔT (red dots) are plotted against the time t_{gate}, which gives the time delay between THz pulse and gate pulse. The THz pulse is only displayed for less than 1.5 ps. Otherwise, it would look like the THz pulse in Figure 3.1a. The different points at the same coordinate on the x-axis belong to different photoconductivity spectra performed at different times after photoexcitation ($t_{\text{photoexcited}}$).

It can be observed, that the maximum of ΔT changes its position on the x-axis t_{gate} for different delays $t_{\text{photoexcited}}$. There is also an noticeable, but much smaller, shift for T.

The shift occurs due to a photoinduced change of the sample's refractive index. The refractive index depends on the material, but also on the charge-

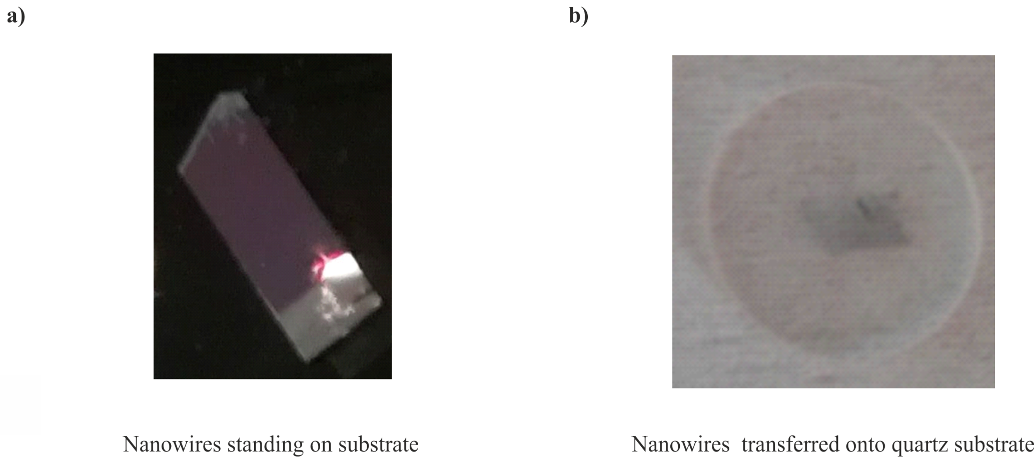

Figure 3.9: (a) Semiconducting nanowires standing on a growth substrate and (b) flat-lying on quartz substrate after transfer from the growth substrate.

carrier density. If the density rises significantly, the refractive indices increase too [126]. Consequently, the optical path, which is defined as product of actual distance and refractive index, becomes longer and the THz pulse arrives later (compared to the gate pulse) than for the same measurement on a material with a smaller refractive index. Therefore, the maxima of ΔT and T shift to longer times t_{gate} with higher excitation powers and carrier densities, respectively. The effect is more prominent for ΔT, because its value is 27 times smaller than T's. For most samples, this effect has no significant influence and cannot be seen using OPTP spectroscopy. However, it can be detrimental for photoconductivity decays if a sample has a strong correlation between photoexcitation power and refractive index. Then it can occur that at high fluences the fixed position of the THz pulse changes while measuring a photoconductivity decay because the carrier density decreases over time. This can create bumps in the scan. If this problem arises, a two-dimensional scan — a series of photoconductivity spectra at different time delays after photoexcitation — is needed to account for the delayed THz pulse.

3.2 Sample preparation

The nanowires studied in Chapter 5, 6 and 7 of this thesis are grown standing (Figure 3.9a, but in this configuration they cannot be measured if the signal from

the growth substrate interferes indistinguishably with the signal from the nanowire samples. Therefore, it is important to develop a method to break them off from the substrate and transfer them to a target substrate. In the following, I will discuss some transfer methods that I used and experimented with.

If a high nanowire density is needed on a target substrate (e.g. glass, quartz, silicon wafer), the most convenient way to achieve this is to rub the nanowires directly onto the new substrate. The nanowires break off close to the growth substrate. Furthermore, they are aligned on the new substrate, if the rubbing is only done in one direction. For the samples used for THz spectroscopy, z-cut quartz discs as the substrate are required since they are transparent to THz radiation and dissipate heat (Figure 3.9b). To improve the adhesion between the quartz substrate and the nanowires, z-cut quartz discs coated with thin (10 nm - 60 nm) layer of parylene C [127] were developed. The polymer was added by the Gorham process [128] in a PSD 2010 LabCoter 2 by Dr. Hannah Joyce at the University of Cambridge. Parylene C is simple to manufacture and also transparent to THz radiation [129].

Another commonly used transfer method is the solution-based transfer technique. Nanowires standing on a growth substrate are put into a beaker filled with 99.9% pure isopropanol and then sonicated in an ultrasonic bath. The duration and strength of the process must be adjusted according to the diameter and chemical composition of the nanowires. For transferring, the nanowires/isopropanol solution is pipetted onto the desired substrate. Isopropanol evaporates and the nanowires are left behind on the surface. The nanowire density can be controlled by the ratio of nanowires to isopropanol.

Sometimes an ultrasonic bath is not the best solution, e.g. when the nanowires either get damaged during the process, or when they do not break off the growth substrate for example due to their large diameter. In that case another rubbing technique can be used. Filter paper is cut into a triangle with a sharp, low angle tip and long neighbouring sides. For transfer, the sharp corner of the filter paper slides along the substrate with nanowires. Some wires will stick to the paper, which is slowly tipped at the new position. This method is not very

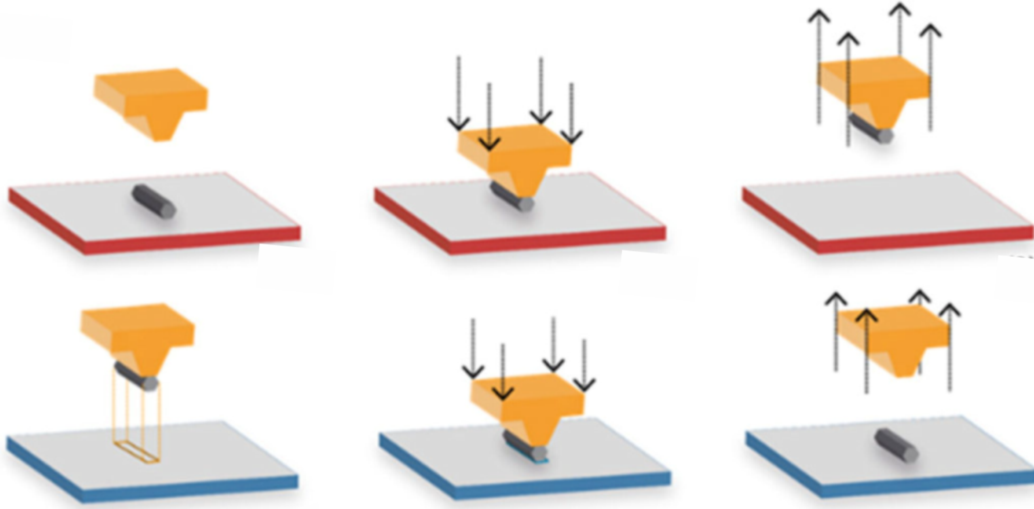

Figure 3.10: Nanoscale transfer printing. A polymer stamp selects a single nanowire and places it accurately and controlled at another position. Adapted from Ref. [131].

efficient. Therefore, the nanowire density will be low, but their transfer position can be more-or-less controlled. If a higher density is needed, the filter paper transfer process can be repeated.

An advanced method offering a more accurate control over the transfer position and orientation of the nanowires has been recently developed. It is called nanoscale transfer printing (nano-TP) [130, 131]. Here, the nanowires are captured by polymer microstamps. Then they are transferred and printed to a predefined position on the target substrate with sub-micrometre accuracy. These stamps are made out of polydimethylsiloxane, which was chosen due to its adhesiveness and viscoelasticity. An example for the precise movement of one wire is given in Figure 3.10.

In the first step the microstamp is aligned parallel to a single nanowire. In a next step the polymer is pressed against and is attached to it. Then the stamp holding the wire can be moved to the new position. After contact with the substrate, the wire is released without any damage. This method is especially beneficial for accurately placing single nanowires for devices. Additionally, using a different stamp, a higher density of nanowires can also be achieved with the same technique.

Each method has its own advantages and is chosen according to the final purpose of the transferred nanowires. For THz spectroscopy, for example, a very

high density of aligned nanowires is needed. Therefore, they are mostly transferred by rubbing them in one direction on parylene-coated quartz. However, if the spacing between the nanowires on the as-grown substrate is large, this method cannot provide the required density. In this case, nano-TP is the better process. Fewer nanowires will be transferred, but they will all be at the same spot and therefore, the density will be higher.

3.3 Summary

In this chapter the measurements of nanowire samples with THz spectroscopy were discussed. Therefore, the principles of THz creation and detection was described. The OPTP setup and both photoconductivity decays and photoconductivity spectra were discussed specifically for nanowire samples. It was also demonstrated how to analyse the data obtained by THz spectroscopy to extract nanowire properties, such as photoconductivity lifetime and surface recombination velocity. Furthermore, ways to prepare nanowire samples for different types of measurements and the advantages and disadvantages of each transfer method were debated.

4

Development of cryogenic mid-infrared Fourier Transform Photoluminescence system

4.1 Photoluminescence Spectroscopy

4.1.1 Introduction to Photoluminescence Spectroscopy

Photoluminescence (PL) spectroscopy is used to characterise the optical properties of nanowires and it can provide complementary data to THz spectroscopy. For PL measurements, the sample is optically excited and the light emitted by the sample is analysed by either time-dependent or wavelength-dependent spectra which are taken with a detector. This method enables among others the characterisation of radiative lifetimes and energy bands [132].

PL spectroscopy incorporates several different characterization techniques, which probe various sample properties and photon energy ranges. Polarisation spectroscopy, for example, optically excites the sample with linearly polarised light and analyses the sample's polarisation dependence. The systems can also be distinguished by the detection system used. The detection can be done by a spectrometer separating the different wavelengths with a diffraction grating and measuring each wavelength on its own, or by simultaneous measurements of all wavelengths with

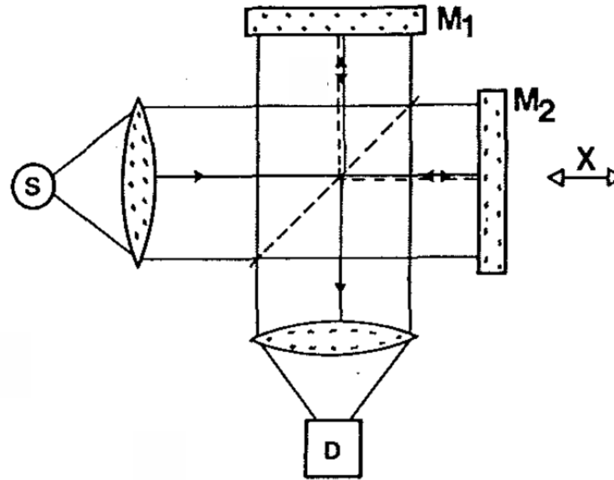

Figure 4.1: Schematic of a Michelson interferometer and FTIR, respectively: the source S emits light, which is split at the beamsplitter and then reflected by two mirrors M1 and M2. M2 is movable, and thus the difference in path length between the two split beams can be altered. Adapted from Ref. [133].

an interference spectrometer [133]. Furthermore, different systems are used for emission spectroscopy in the infrared and visible regions, respectively.

To characterise the nanowire samples used in this thesis, the measurements were performed on a cryogenic mid-infrared Fourier transform photoluminescence (FTIR PL) system, which was custom designed for this thesis work. Therefore, the functional principles and usage of the FTIR will be introduced in the following.

4.1.2 Fourier Transform Infrared Spectrometry

4.1.2.1 Functional principles

Fourier Transform Infrared Spectrometry (FTIR spectroscopy) is an optical experimental technique used to obtain an infrared spectrum of a material, and is so called because a Fourier transform is needed to convert the raw data (interferogram) into the (absorption) spectrum [133]. For measurements, light is coupled into the Michelson interferometer which consists of two mirrors and a beamsplitter aligned in the way shown in Figure 4.1. Photons, emitted by a light source, are coupled into the Michelson interferometer. The beamsplitter divides the light into two coherent, equally powerful parts which follow different paths. They are both reflected at mirrors, before they are coupled together again. One of the mirrors

is fixed, but the other one can be moved. Thus, the difference in path length of both coherent rays can be continuously altered, resulting in constructive and destructive interference at the detector. The interference is recorded by a detector as a time-dependent interferogram. The interferogram is then converted into the energy domain by a Fourier transform. Modern FTIR systems can cover the spectral range from ultraviolet to far-infrared by easily interchangeable detectors, light sources, and beamsplitters.

Originally the FTIR spectrometer was especially designed for infrared measurements. Therefore, the FTIR spectrometer is either purged with nitrogen or under vacuum to prevent the photons from being absorbed by water vapour present in the air. Additionally, the vacuum protects the hygroscopic optical parts from moisture.

4.1.2.2 Usage of Fourier Transform Infrared Spectrometer

FTIR spectrometers are used for many different kinds of measurements due to their many advantages. It is a very versatile tool and has applications when rapid scanning, high sensitivity, high resolution, and data processing are required.

It is predominately used for transmission, reflection, and thus absorption measurements. For this purpose, a source emitting a broad spectrum of light is used. The photons travel through the Michelson interferometer. Before the detector, they interact with the sample — either by reflection or transmission, where photons of certain wavelengths will be absorbed by the sample. The bandgap of semiconductors can be determined in this way for instance.

The FTIR can also be used for photocurrent spectroscopy. With this method no sample is tested, but instead a detector. Usually the spectral response of a detector is analysed monochromatically. Using an FTIR spectrometer enables one to measure the spectral response for a broad light spectrum. This is especially beneficial if small detectors like nanowire devices are tested, but requires the response of the detector to be linear.

4.1.2.3 Fourier Transform Photoluminescence Spectroscopy

The FTIR spectrometer is also a useful method to measure samples emitting in the (mid)-infrared. For that, the (illuminated) sample replaces the conventional light source. Because the samples investigated in this thesis generally have a low radiative efficiency which increases with decreasing temperatures, a custom-designed cryogenic mid-infrared Fourier transform photoluminescence spectroscopy setup was built. It enables short scan times, a high signal-to-noise ratio, and a good spectral resolution. Furthermore, the vacuum in the system prevents IR absorption from water molecules present in the air, and allows the sample to be cooled down to 4.2 K.

The home-built FTIR PL system consists of the commercially produced FTIR Vertex 80v from Bruker GmbH and a home-built PL system attached to its side entrance. The PL sample chamber was designed to enable movements of the samples in relation to the excitation laser, to hold multiple samples per run, and to allow fine alignments of the sample and system during a measurement run. The modifications save time because fewer sample changes need to take place (requiring the sample chamber to warm up to room temperature, and after a sample change, being pumped down and cooled down). It is also less costly because of the reduced number of runs for which less liquid helium (He) is required for cooling.

The newly-built system will be discussed in the following section. First the design of the sample chamber and the sample holder will be described, followed by the whole setup. The optimal parameters for PL spectroscopy on nanowires will also be given. In the end, calibration of the PL spectra will be demonstrated.

4.2 Custom-designed Fourier Transform Photoluminescence system

4.2.1 Custom components

4.2.1.1 Sample chamber

A special sample chamber was developed for the PL system, in order to enable measurements of multiple samples in one run and adjustments of the sample in

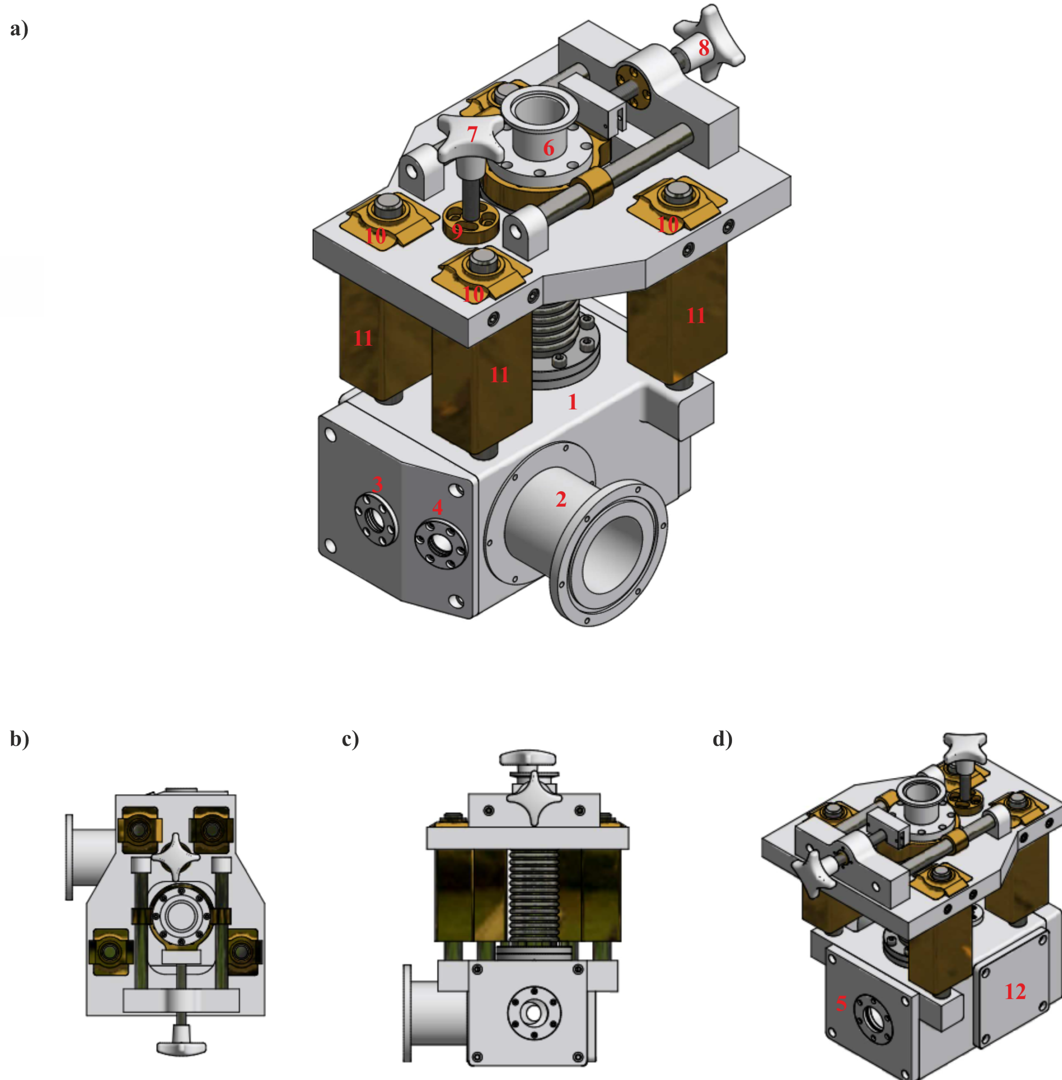

Figure 4.2: CAD model of the sample vacuum chamber from (a) 3D projection, (b) top view, (c) side view and (d) 3D projection of the back. The different numbers describe the different parts of the chamber: (1) main PL chamber, (2) side port to FTIR, (3)-(5) windows, (6) translation bellows, (7) Z-translation adjuster, (8) X-translation adjuster, (9) brass bearings, (10) supports and (11) their stabilising brass tubes, and (12) plate with off-axis parabolic mirror. The CAD model was made by Nick Callaghan.

relation to the excitation laser. A CAD model of the vaccum chamber is presented in Figure 4.2, where it is viewed from different angles. The different components (1-12) are discussed in the following.

The main chamber (1) was milled out of a single piece of stainless steel. It is connected to a side port of the FTIR system (2). Flanges with quartz windows (3-5) are attached on the short sides of the chamber. Window (3) is the entrance for the excitation laser to the chamber. The light from the excitation laser passes through a hole in the off-axis parabolic gold mirror, which is used to collect the photons emitted from the sample, and then illuminates the sample. If the laser radiation is partially transmitted through the sample, it exits the vacuum chamber through window (5) and is collected by a beam dump.

Window (4) can also be used as entrance port for the excitation laser. On this path, the light passes in front of the parabolic mirror and hits the sample at an angle of roughly 45°, reducing the fraction of scattered laser photons collected by the parabolic mirror.

The sample is mounted on a cold finger which is inserted into the translation bellows (6). The bellows, and thus the sample, can be moved with adjustment screws in the Z- (7) and X-directions (8). The screws are connected to the chamber with brass bearings (9), while the top shelf with the sample holder is stabilised by four supports (10). The X-translation screw is used to adjust the distance between sample and parabolic mirror. Through the Z-adjustment the sample holder can be moved up and down, enabling measurements of multiple neighbouring samples in one run. Being able to measure at various positions on one sample, and measuring multiple scans in one run is both time-saving and cost-saving.

The weight of the He-transfer tube, which connects the He-dewar to the sample holder, puts a large torque on the bellows mechanism and especially the supports (10). Therefore, the bearings of the supports did not move by equal amounts, and the sample holder was tilted, changing the distance between the parabolic mirror and the sample during the first test runs. Furthermore, the excitation spot on

a)

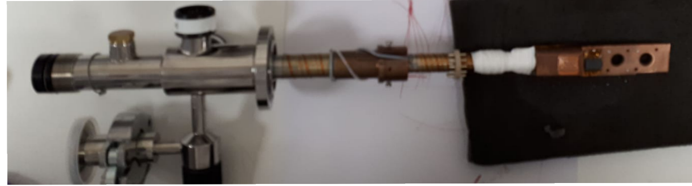

b)

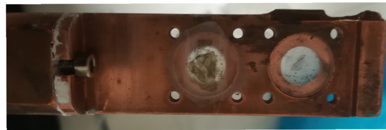

c)

Figure 4.3: Pictures of (a) cold finger, (b) sample holder for quartz discs, and (c) sample holder for wafer pieces with a silver heat shield. To distinguish the various samples (black), thin strips of wafer (shiny), emitting at a different wavelength than the samples, are used as dividers.

the sample moved randomly left and right. This problem was solved by adding long brass tubes (11) to the bearings for stabilisation.

The PL vacuum box itself is divided into two chambers, separated by a glass window, which is situated between sample holder and parabolic mirror, which is attached to flange (12). Due to this window, the chambers can be evacuated separately. The first chamber containing the parabolic mirror is openly connected to the FTIR, which operates at a pressure of around 10^{-2} mbar, while the second chamber, containing the sample, is at a pressure of around 10^{-7} mbar during cryogenic measurements.

4.2.1.2 Sample holder

The shape of the samples typically measured with this system can be divided into two different types — one on a round, 13 mm diameter quartz disc and the other on a small, thin, randomly sized substrate, which is often a semiconducting wafer. The two kinds of substrates need to be mounted on different sample holders, which are shown in Figure 4.3. If the samples are on quartz discs, two samples can be measured during one measurement run. They are fixed in milled holes on the sample holder. However, the vertical distance, by which the sample holder

can be moved, is only around 30 mm. Therefore, only one disc and half of the second one can be measured in one run.

If the sample is on a wafer, this wafer can be cleaved into small pieces and multiple samples can be combined on a holder. The pieces are glued to the sample holder with vacuum grease, which keeps its adhesive properties even at cryogenic temperatures. To distinguish the samples, long, thin semiconductor wafer strips are added between two samples. The wafer fragments emit a strong PL at a wavelength different than the PL of the sample. The strips should be wider than the laser spot size which was of roughly 1 mm in full width at half maximum.

4.2.1.3 System setup

After discussing the individual parts of the FTIR PL system, such as the vacuum compartment containing the sample and the FTIR (Section 4.1.2), I will explain now how the single components are put together to build a cryogenic mid-infrared Fourier transform photoluminescence spectroscopy system. A sketch of the system can be found in Figure 4.4.

The samples are excited by the output of a diode pumped solid state laser (Ventus, continuous wave, 532 nm (2.33 eV), max. 110 mW). A 532±10 nm bandpass filter suppresses the residual emission from the diode. The laser power can be varied by using a neutral density (ND) filter wheel. The laser was aligned onto the sample with dielectric mirrors, which are optimised for 523 nm and 1064 nm, to reduce losses. The laser optically excites the sample, resulting in photoluminescence. The photoluminescence radiation and the pump light are collected by the gold-coated aluminium off-axis parabolic mirror and coupled into the FTIR. In order to maximise the collection efficiency of photoluminescence photons, the sample surface is at the focal point of the parabolic mirror. To suppress the scattered laser photons, which are also gathered by the parabolic mirror, a longpass filter is used in the optical path before the detector. Depending on the emission wavelength of the sample either a 780 nm longpass filter (Chapter 6 and 7.2) or a silicon filter (Chapter 7.3) was used.

To reduce the noise, the detector is connected to a lock-in amplifier, which is phase-locked to a chopper in front of the laser. The chopper was usually driven at around 3000 Hz. To increase the versatility of the system, the 532 nm laser can be easily replaced by a 1064 nm laser. Various FTIR detectors and beamsplitters can be used for the measurement, and they should be selected according to their spectral response and the PL range of the sample. It is also optional to use a focusing lens in the PL excitation laser beam. However, this is not necessarily beneficial for all samples because a higher power density could burn the sample. Furthermore, as a smaller area of the sample is optically excited, this could result in a decrease of PL intensity.

4.2.2 Measurement of Fourier Transform Photoluminescence

4.2.2.1 Scanning parameters

While I have already discussed the usage of the FTIR, the settings for FTIR PL spectroscopy are different than the ones for measurements only with the FTIR, such as transmission/reflection. Therefore, I will discuss in the following the specific parameters for measuring PL with the FTIR and present a table with the optimal settings for nanowire samples on the system described above.

For transmission and reflection measurements, the movable mirror changes the path length steadily and continuously. The time-dependent constructive and destructive interference are detected and converted into an energy spectrum by Fourier transform. To reduce the noise, the same scan is performed multiple times and the average of all this succeeding interferograms is taken. For FTIR PL spectroscopy, these measurements are not possible because the light source is pulsed. Therefore, the FTIR needs to be operated in step-scan mode. This means that the movable mirror is fixed at the starting point. The PL signal at that position is measured when triggered by the lock-in amplifier. For noise reduction, multiple points are taken at one mirror position, called coadditions, and averaged over. Afterwards, the mirror moves to the next position, which is determined by the resolution settings of the scan, and held there during the measurement of

the next point. This is repeated until all data points are taken. In the end, all the individual time-domain measurements are stitched together and the energy spectrum is calculated by Fourier transform.

Step-scan mode takes longer than a normal measurement in which the movable mirror is in continuous oscillating motion. Therefore, often a trade-off needs to be made between the desired resolution and scan time. Furthermore, the optimal parameters for PL spectroscopy depend largely on the sample and the particular FTIR. The parameters used for the photoluminescence measurements in Chapter 7 are given in Table 4.1. These settings are specific to the commercially produced FTIR Vertex 80v, the software OPUS, which is used for controlling the setup and the Fourier transform, and nanowire samples in the infrared. However, they can also be taken as initial settings for other measurements. The parameters are divided into settings for the lock-in amplifier and the ones for the OPUS software.

The stabilisation delay is the down time during which the mirror moves to the next position. It must be longer than several times the constant of the lock-in amplifier. The resolution determines the accuracy of the scan and has a large impact on the duration of the measurement. It should be chosen in such a way that all features of the PL spectrum can still be distinguished. The phase resolution influences the Fourier transform made by the OPUS software and should be around four times higher than the measurement resolution. In the OPUS software different methods for the Fourier transform for data processing can be selected. Information about all options can be found in the manual [134]. Optical filters can be automatically inserted with a filter wheel inside the FTIR. The filter should block the excitation laser and scattered light from the environment, while being transparent to the sample's PL. Furthermore, detector and beamsplitter need to be adjusted according to their spectral response. The aperture is typically used to control the rate at which the photons reach the detector. Its diameter should be small enough to ensure that the detector is not saturated, but large enough to enable a well detectable signal

OPUS parameters			
Stabilisation delay	330 ms		
Number of coadditions	100,000		
Resolution	$50\,\mathrm{cm}^{-1}$		
Phase resolution	$200\,\mathrm{cm}^{-1}$		
Optic	right input		
Beamsplitter	CaF_2		
Optical filter settings	silicon (NG4)		
Aperture	8 mm		
Detector	DC_In [Internal Pos. 2] (InSb)		
Sample signal gain	automatic		
Sample preamp gain	Ref		
Delay after device change	0 s		
Delay before measurement	0 s		
Optical bench ready	off		
Wanted high frequency limit	7950 ($15797.87\,\mathrm{cm}^{-1}$)		
Wanted low frequency limit	0 ($0\,\mathrm{cm}^{-1}$)		
Highpass filter	open		
Low pass filter	automatic		
Acquisation mode	single sided		
Phase correction	Mertz/No Peak Search		
Apodization function	Blackman-Harris-3-Term		
Zero-filling factor	128		
Lock-in amplifier			
Time constant	300 ms		
Sensitivity	$2\,\mu\mathrm{V}$		
Signal input	A	AC	Float
Reserve	low noise		
Filters	Line		2xLine
Chopper frequency	3038 Hz		
Phase	30°		

Table 4.1: Settings of the FTIR software OPUS and the lock-in amplifier for FTIR PL spectroscopy on nanowire samples

4.2.2.2 Calibration

After all measurements have been performed, the excitation laser's beamwidth and power need to be determined and the system and spectra need to be calibrated. It is especially necessary to calibrate the detector because the PL spectrum is supposed to show the true emitted intensity from the sample, and not the one changed by the system response function of beamsplitters, mirrors, filters and detectors. Therefore, a spectrum of a known source is recorded. The difference between the original emitted light and the measured spectrum shows the changes caused by the system. A blackbody radiation source at a temperature of 1373 K — an internal MIR light source for the FTIR Vertex 80v supplied by Bruker GmbH — was used for calibration. It is a continuous light emitter integrated in the FTIR system. Because the chopper is outside of the FTIR box, the measurement cannot be triggered. Therefore, a normal continuous scan was performed. The optical parameters and the settings of the OPUS software are measured under the same conditions and system influences as the PL measurements before.

The resulting spectrum is fitted by a polynomial fit of the ninth order to smooth it for further calculations. In the original spectra there are steps due to the resolution of $50\,\mathrm{cm}^{-1}$ or more. The fit is divided by the theoretical spectral intensity I

$$I = \frac{2\pi hc^2}{\lambda^5}\frac{1}{\exp(\frac{hc}{\lambda k_b T} - 1)} \tag{4.1}$$

for a blackbody at 1373 K [56]. h is the Planck constant, λ stands for the wavelength and k_b for the Boltzmann constant. The quotient of measured and theoretical spectrum describes the influence of the optical path and detector on the measured data. Therefore, the PL spectra are divided by it.

4.3 Summary

In summary, the development of a custom-designed cryogenic mid-infrared Fourier Transform Photoluminescence was discussed. Therefore, photoluminescence spectroscopy and the usage and functions of a FTIR spectrometer were introduced.

Then the home-built FTIR PL setup was debated. The focus was on the sample chamber which enabled measurements of multiple samples in one run because the new chamber allowed adjustments of the samples in Z- and X-directions. Furthermore, exemplary setting parameters for PL spectroscopy with an FTIR and the calibration of spectra were given.

Figure 4.4: Schematic of the home-built FTIR PL system.

5 Wurtzite GaP nanowires

5.1 Wurtzite GaP nanowires as template for hexagonal silicon

GaP is a promising candidate to cover the "green gap" technology for intrinsically green LEDs due to its bandgap of 2.26 eV [135, 136]. Yet, its indirect bandgap limits its use for light emission applications, and thus the usability of GaP for many applications. Theory has suggested the usage of a different crystal structure to create direct bandgap GaP and thus overcome the inefficient light conversion [137, 138]. A controlled engineering of the crystal structure can be achieved by nanowire growth as discussed in Chapter 2. Zincblende is the naturally occurring crystal structure for GaP [139] causing an indirect bandgap. The direct bandgap of wurtzite GaP with an energy of around 2.13 eV (582 nm) at low temperatures has been confirmed and investigated [52, 132, 136, 140].

While wurtzite GaP nanowires have received widespread attention based on their prospects for visible optical devices, I principally focus on their application as a template to achieve direct bandgap SiGe which may revolutionise silicon technology. If SiGe is grown around the wurtzite GaP nanowires, the shell adapts to the crystal structure of the core and develops a direct bandgap [45, 53]. A deeper insight into growth and properties of direct bandgap SiGe will be given in Chapter 6. In this

chapter, I will focus purely on wurtzite GaP nanowires to get a better understanding of their growth, defects, surface defects and their influence on material properties. This knowledge is important for the use of GaP nanowires as templates for hexagonal shells because the dimensions and quality of the template will determine the quality of the SiGe shell which inherits the defects of the core [45, 141].

THz spectroscopy is used to analyse and discuss degradation of GaP nanowires and the influence of the precursor's ratio on defect density and lifetime. Furthermore, the growth of these samples will be compared to the two-step core-clad growth method with which GaP nanowires are initially grown axially followed by radial growth, and thus enabling the growth of nanowires with a diverse range of different diameters.

5.2 Sample preparation

All GaP nanowires discussed in this chapter were grown by Yizhen Ren in Professor Erik Bakkers' group at the University of Eindhoven in a low-pressure (50 mbar) Aixtron close-coupled showerhead metalorganic vapour-phase epitaxy (CCS-MOVPE) system using the selective area vapour-liquid-solid (SA-VLS) approach on 2 inch GaP(111)B wafers. More details about the growth system MOVPE can be found in Section 2.1.1.

The growth was achieved by patterning the GaP wafer, which was covered at both sides by SiN_x with nanosized holes. Subsequently, gold layers were deposited via electron-beam evaporation, followed by a standard lift-off technique to remove the gold outside the holes, thus leaving behind gold discs as the catalyst in the selected areas. Two different series of GaP nanowire samples, which are listed in detail in Table 5.1, were grown: a series of sample growth was performed where the flux ratio of the group V to group III elements was varied and it is called single-step series. The second series of samples has a constant V/III ratio of 12.2, but the nanowire diameter is varied. It is called two-step series.

The single-step series consists of 6 master samples. Their diameter for all samples was similar which is in the range of 130 nm to 150 nm, and their length varied

Series name	V/III ratio	Diameter [nm]	growth process
single-step	10.7	150	core
single-step	21.5	150	core
single-step	30.0	150	core
single-step	40.8	150	core
single-step	49.3	150	core
single-step	60.1	150	core
two-step	12.2	46	core-clad
two-step	12.2	142	core-clad
two-step	12.2	171	core-clad
two-step	12.2	175	core-clad
two-step	12.2	219	core-clad
two-step	12.2	233	core-clad
two-step	12.2	266	core-clad
two-step	12.2	298	core-clad

Table 5.1: Overview of the wurtzite GaP nanowire samples which are divided into two series.

between 5 and 13 μm. For the growth of this series, the holes, which were printed into a 50 nm thick SiN_x layer with nanoimprint lithography, had a diameter of 250 nm and a pitch size of 2.5 μm. Wurtzite phased GaP nanowires were grown at 600 °C using gold discs of 16 nm as catalyst and phosphine (PH_3) and trimethylgallium (TMGa) as precursors. The flux ratio of PH_3 to TMGa, the V/III ratio, was changed from 10.7 to 60.1 for the different samples. Hydrogen chloride (HCl) was used to prevent tapering of the nanowires because HCl acted as an in-situ etchant and impeded radial growth [142]. Each master sample was broken into segments to perform different measurement techniques on each fragment. I received two pieces of each master sample. One set was directly sent to Oxford to perform THz spectroscopy measurements on them. These samples were stored in a glovebox (nitrogen environment; 5 parts per million (ppm) oxygen and water; 3 to 4 bar). The second set was kept in Eindhoven for three months, stored in air, and some of these nanowires were transferred onto a copper grid for TEM. Then the second set was also sent to Oxford and subsequently stored in a nitrogen environment.

A two-step series of wurtzite GaP nanowires was then grown. Theoretically, the size of the gold catalyst determines the diameter of the nanowire; thus it should be possible to grow similar wires with different diameters by changing the size of the

gold catalyst. However, as the supersaturation of the catalyst with precursors is size-dependent, a larger gold catalyst increases the stacking fault density, if growth parameters stay the same [143, 144]. In order to grow nanowires with different diameters but same quality, the two-step core-clad growth procedure was developed [145]. First, 50 nm holes with a pitch size of 2.5 μm were put into the 20 nm thick SiN_x layer, covering the GaP substrate, by electron beam lithography. A 6 nm thick gold disc acted as a catalyst, and PH_3 and TMGa as precursors. Wurtzite GaP cores of 50 nm were grown at 600 °C with a V/III ratio of 12.2. Afterwards the parameters were changed to 615° C and a V/III ratio of 162.5. Then wurtzite GaP shells were grown around the cores. Eight samples were produced with a length of about 9 μm and diameters ranging from 46 nm to 298 nm. However, uniform diameters could not be easily achieved and the distribution varied for each sample significantly. The standard deviation of the nanowire diameters even reached up to 30 nm. The sample with a diameter of 46 nm was grown differently than the other samples because it had already reached the desired diameter after core growth.

Both the single-step and the two-step series consist of non-tapered GaP nanowires with similar geometry. However, the differences in growth have a significant effect on the unintentional doping in the two different series of GaP nanowires — as can be seen in the work of Perea *et al.* [71]. They fabricated Ge nanowires with phosphorus doping in a chemical vapour deposition (CVD) system in two steps. First, the core was grown with a gold droplet as catalyst via the VLS method. This means that the crystal grows at the liquid-solid interface from the Ge enriched catalyst. Afterwards, a shell made of the same material was radially grown through catalyst-free gaseous solid surface growth. Due to the different growth mechanisms, the dopant concentration was 6 orders of magnitude higher for the shell than for the core, while the precursor flow ratios stayed constant. The same effect was also observed for unintentional carbon doping using MOVPE systems [72, 146]. The same also happened to the two-step series of GaP nanowires studied in this thesis.

Sebastian Kölling from Professor Erik Bakkers' group performed atom probe tomography (APT) on a 150 nm thick GaP nanowire grown with core-shell structure

and determined high unintentional carbon doping of 400 ppm to 500 ppm averaged over the whole wire. Due to an increased doping insertion during radial growth, it can be assumed that this value would be much higher than the average over the whole GaP nanowire. This assumption will be confirmed in the following by THz spectroscopy measurements, for which each sample was transferred onto a parylene-coated quartz, which is transparent to THz radiation [129].

5.3 OPTP setup optimisation for GaP nanowires

OPTP spectroscopy is a non-contact method to extract the electrical properties of semiconducting samples, such as photoconductivity lifetime, momentum scattering and charge-carrier mobility. A detailed discussion about the setup and principles of THz spectroscopy is given in Section 3.1. The OPTP system needs to be adjusted and optimised for each type of samples, in order to achieve a high signal intensity and signal-to-noise ratio. The experimental details and changes of the setup specifically for GaP nanowires will be explained in the following.

A laser amplifier with a centre wavelength of 800 nm (1.55 eV) and a pulse duration of 35 fs was used to perform measurements under vacuum at room temperature. The beam path was split into three different paths: one to create the THz radiation by interaction with a spintronic emitter, one to detect the THz pulse after transition through the sample, and one to optically excite the nanowire sample.

The energy of the photons (1.55 eV), which were used to optically excite the sample, is lower than the direct bandgap of wurtzite GaP nanowires ($E_{\text{gap}}(4\,\text{K}) = 2.2\,\text{eV}$ [132]). Therefore, a beta barium borate (BBO) crystal is used to double the frequency of the excitation photons to 400 nm (3.10 eV). The excitation fluence was varied through a neutral density filter wheel (8 to 63 $\mu\text{J}\,\text{cm}^{-2}$).

In Figure 5.1a, a photoconductivity decay of the GaP nanowire sample, which belongs to the single-step series with a V/III ratio of 10.7, is shown at a fluence of 35 $\mu\text{J}\,\text{cm}^{-2}$. A (110) GaP crystal (200 μm thick) was used to detect the THz radiation after transmission through the sample. The measurement is the average over 10 scans with each 60,000 boxcar averages. Despite the averaging and long

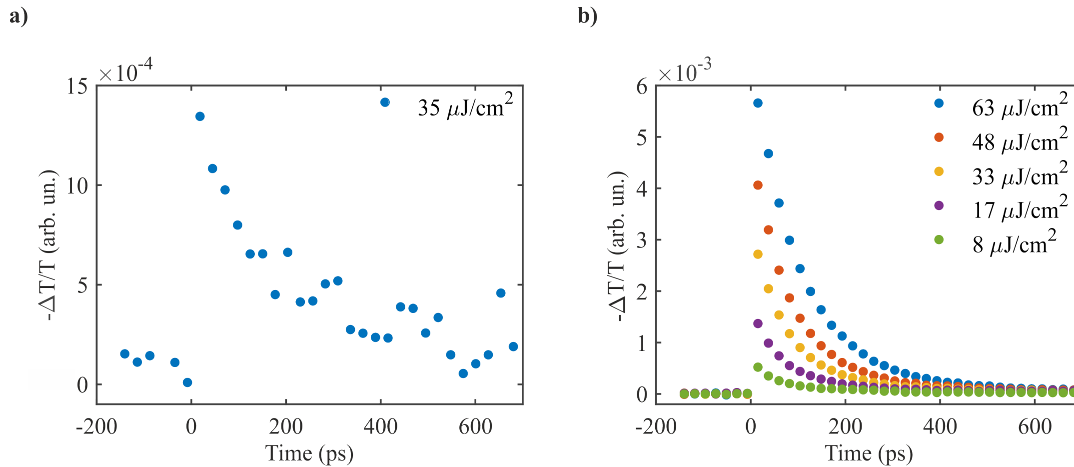

Figure 5.1: Photoconductivity decays for the same sample (GaP with V/III = 10.7) (a) before and after (b) optimising the THz spectroscopy setup for GaP nanowire samples. The signal intensity, signal-to-noise ratio and scanning time were improved due to a different detection crystal.

measurement times of over 10 hours, the signal intensity and the signal-to-noise ratio is small, increasing the error for extracting photoconductivity lifetimes.

To optimise the scanning parameters for these samples, different approaches were considered. First, the fluence was increased by decreasing the area of the pump beam on the sample. Second, the (110) GaP detection crystal (200 μm thick) was replaced by a (110) ZnTe crystal (1 mm thick). Using a thick ZnTe as a detection crystal yields a higher signal than GaP, but reduces the detectable bandwidth of the THz pulse [122, 123].

The improvement due to the 1 mm (110) ZnTe crystal can be seen in Figure 5.1b. The excitation fluence was tunable from 8 up to 63 μJ cm^{-2}. With the optimised THz system only 5 scans with 10,000 boxcar averages were taken, thus one measurement was completed within 40 minutes.

5.4 Degradation of GaP nanowires

After optimisation of the OPTP system for GaP nanowires, it also needs to be ensured that the samples are not damaged during OPTP spectroscopy or storage, and thus the quality of the measurement is not reduced.

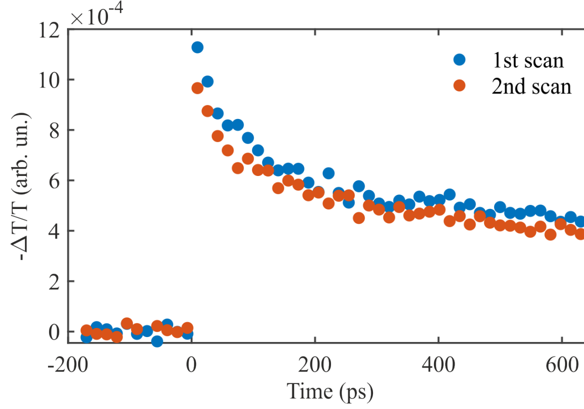

Figure 5.2: Comparison of two spectra from wurtzite GaP nanowires at 13 μJ cm^{-2}, which were taken 27 hours apart from each other and show no significant degradation despite continuous excitation.

During OPTP spectroscopy

In order to identify damages caused by the high excitation fluences of the pump pulse during OPTP spectroscopy, long measurements were performed on the GaP nanowires with a diameter of 298 nm and a V/III ratio of 12.2. Two spectra at a fluence of 13 μJ cm^{-2} are compared to each other in Figure 5.2. The first scan was taken at the beginning and the second one 27 hours afterwards. The sample was being measured and excited at different fluences, which varied from 8 to 63 μJ cm^{-2}, for 21 out of the 27 hours. A six hour break from optically pumping this sample was taken in the middle of the 27 h. The two photoconductivity decays measured at different times are very similar. The intensity of the second measurement is slightly lower than the first measurement, but this can be attributed to normal fluctuations of THz signal and heating of the sample over time. The signal intensity will recover with time, as it has been observed for other samples before. Therefore, it can be assumed that the measurements with the OPTP setup does not cause any long-term damage on the GaP samples.

During storage

Multiple measurements were performed before and after optimisation of the OPTP system, which is described in Section 5.3, on GaP nanowires. However, they cannot be compared qualitatively to each other because the samples degraded during storage. Therefore, the degradation and its dependence on storage is investigated in the

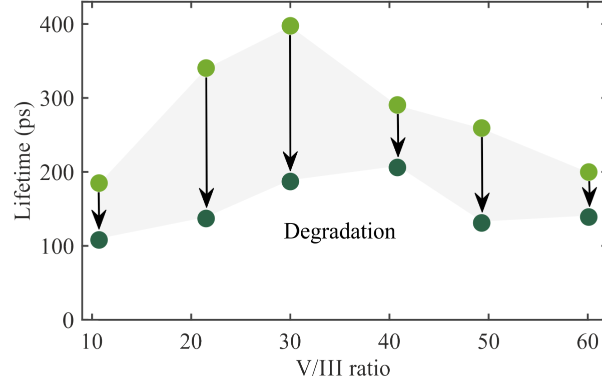

Figure 5.3: Sample degradation of GaP nanowires with different V/III ratios between two sets of measurements, which were 3 weeks apart with samples stored under a nitrogen environment. The first set (bright green) was taken at 35 μJ cm^{-2}, while the second one (dark green) had a fluence of 63 μJ cm^{-2}. The samples were stored under nitrogen environment and measured under vacuum.

following section on the base of the wurtzite GaP nanowire samples from the single-step series by analysing their photoconductivity lifetimes with OPTP spectroscopy.

The photoconductivity decay at the highest fluence of 35 μJ cm^{-2} was taken from each of the six GaP samples with varying V/III ratio. Each scan was fitted by a monoexponential decay equation, thus extracting the sample's lifetime. The results are given in Figure 5.3 (bright green dots). After storing the samples for three weeks under nitrogen environment, the second set of THz measurements was performed. The spectra at a fluence of 63 μJ cm^{-2} were taken and fitted monoexponentially (dark green dots).

The first-time measurements (bright green) show that the photoconductivity lifetime reaches a maximum lifetime of 398 ps around V/III = 30.0. The lifetimes extracted from the second-time measurements (dark green) do not follow the same trend. GaP nanowires with V/III = 40.8 have a maximum lifetime of 187 ps. The measurements were performed with doubled excitation fluence, for which it is expected to see higher lifetimes due to trap saturation when using higher excitation powers [112]. However, the lifetimes decreased by up to 2.5 times, indicating a strong degradation. The drop of lifetimes suggests that the samples degraded, but to a different degree for each sample. To verify the influence of the storage, a second set of the same single-step series which was stored differently to the first set was measured.

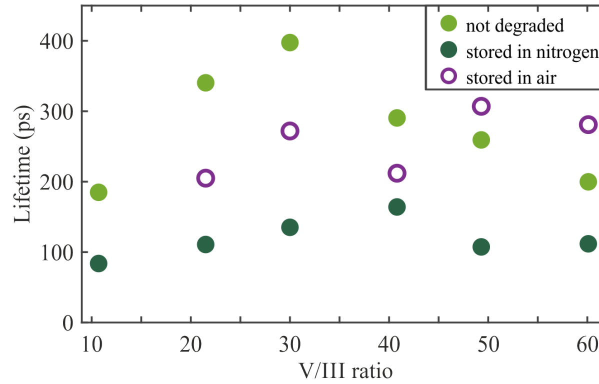

Figure 5.4: Lifetime degradation of GaP nanowires grown with different V/III ratios: bright green dots represent the lifetimes obtained from the first measurements of the first set of the single-step series. Dark green dots stand for the lifetimes extracted from the second series of measurements three weeks after storing them under nitrogen atmosphere. The purple circles show the lifetimes of measurements on a second set of fragments from the same series. These samples were stored a few months in air and then in nitrogen. The samples degrade in nitrogen, but not in an air environment.

The photoconductivity lifetimes extracted from three series of measurements for different V/III ratios are compared in Figure 5.4. The excitation fluence was $35\pm2\,\mu\text{J}\,\text{cm}^{-2}$ and the measurements were performed at different times. The first (light green dots) and second (dark green dots) series of scans were taken from the first sample set, which had been stored under nitrogen environment. There was a time difference between three weeks between those sets of measurements. The third series (purple circles) was performed on the second sample set, which had been stored in air for three months and under nitrogen for six months, 10 months after the other set of samples. The first series of scans were used as benchmark for the following sets of measurements. Storing the samples under nitrogen environment decreased the lifetimes of the sample up to 3 times. The degradation of the sample stored in air only shows a degradation of up to 1.5 times for some samples. Other samples have a longer lifetime than the measurements on the first set of samples, taken soon after growth.

These observations suggest that the nitrogen environment has a different effect on GaP nanowires than air. Apparently, the molecules in the atmosphere, such as oxygen and water, seem to improve the performance of the nanowire samples, but the degree varies for each sample. The dependence could be attributed to a

reaction, which depends on the V/III ratio of GaP nanowires. It could be that a protective, native oxide layer is built around the nanowires in air [147]. This would not be possible in the nitrogen atmosphere of the glovebox because there are only 5 ppm of oxygen and water. However, the passivation layer could have still been created during the transport when the samples were exposed to air. Consequently, a passivation layer cannot explain the degradation while stored in a nitrogen-filled glovebox. The degradation cannot only be due to the nitrogen, but also due to contamination in the glovebox which is also used to store other samples and connected to an evaporator for perovskites.

In conclusion, it appears that storing GaP nanowires under atmosphere is beneficial for them and can even increase the photoconductivity lifetime of samples with certain V/III ratios. In contrast, a nitrogen environment in a possibly contaminated glovebox seems to be detrimental for the electrical properties of GaP nanowires.

5.5 Correlation of lifetime and growth parameters

To gain a better understanding of the influence of stacking faults on nanowire electrical properties, such as photoconductivity lifetime, six samples from the single-step series with different precursor flow rates were characterised with transmission electron microscopy (TEM) and THz spectroscopy. TEM was performed by Dr. Marcel Verheijen from the University of Eindhoven.

All samples have uniform, high quality grown nanowires. However, the nanowires have stacking faults, the density of which varies with the V/III ratio. The stacking fault density was extracted from bright field TEM images. Examples of three different samples are shown in Figure 5.5a, with V/III ratios of 10.7, 30.0, and 60.1, respectively. The dark half sphere at the end of the wires is the gold catalyst and each black stripe perpendicular to the nanowire axis represent a stacking fault. The defect densities — averaged over ten nanowires — for all six samples are given in Figure 5.5b. GaP nanowires grown with a V/III flux ratio of 10.7 have the

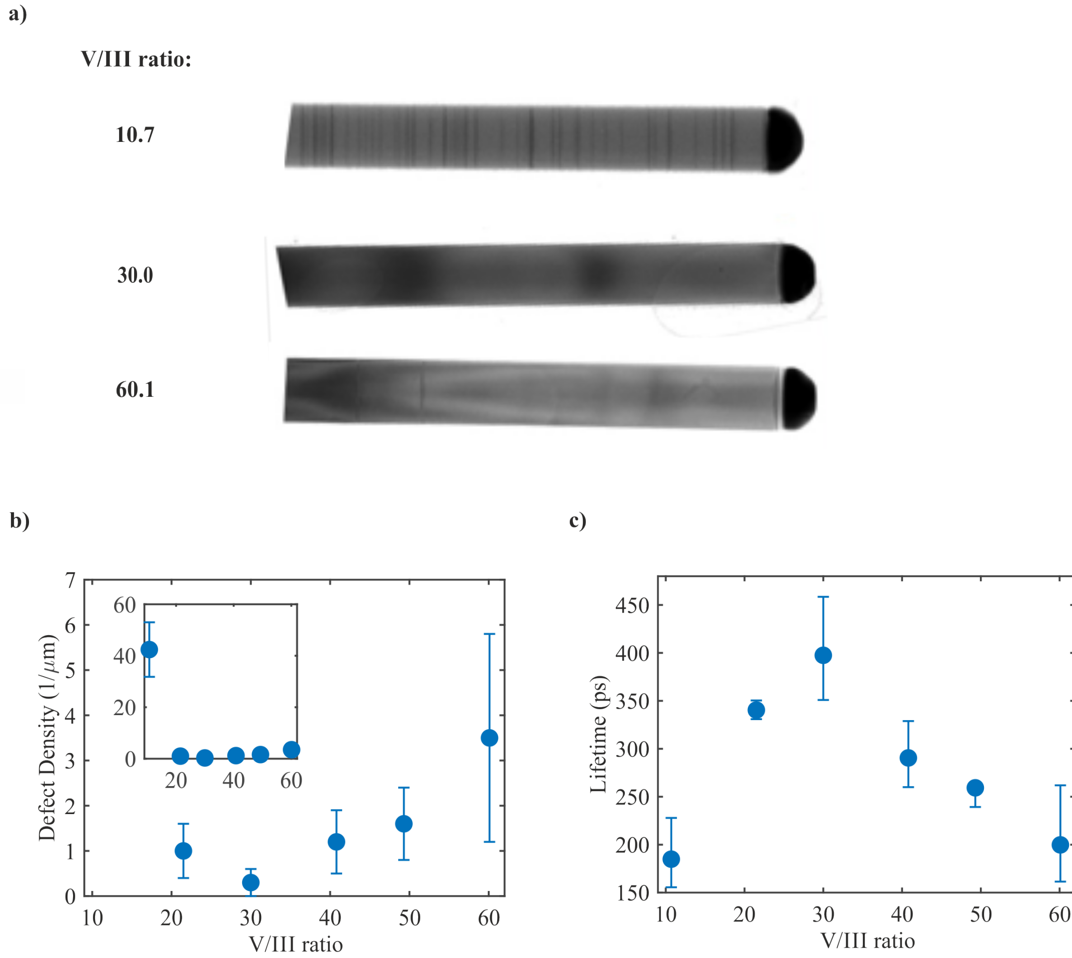

Figure 5.5: (a) TEM pictures of three GaP nanowires with different V/III ratios of 10.7, 30.0, 60.1. Each wire has a different defect density. (b) Defect density, extracted from TEM pictures, plotted against the V/III ratio. The inset shows all values, even the outlier at V/III = 10.7. (c) The lifetimes, which were extracted by a monoexponential fit from photoconductivity decays taken with THz spectroscopy, also have a strong dependence on the V/III ratio.

highest defect density of 42.2 μm^{-1}. The value is more than 12 times higher than the density in any other sample. In general, the defect density depends strongly on the V/III ratio and reaches a minimum of 0.3 μm^{-1} for V/III = 30.0.

Furthermore, the V/III flux ratio appears to have a significant influence on the nanowire lifetimes, which varies from 185 ps to 398 ps for the different samples, as shown in Figure 5.5c. The photoconductivity lifetimes of wurtzite GaP nanowires are much shorter than the lifetime of the zincblende GaP wafer, which is around 254 ns [140]. This disparity is caused by their different types of bandgaps: zincblende GaP has an indirect bandgap, but wurtzite GaP has a direct bandgap. In a direct

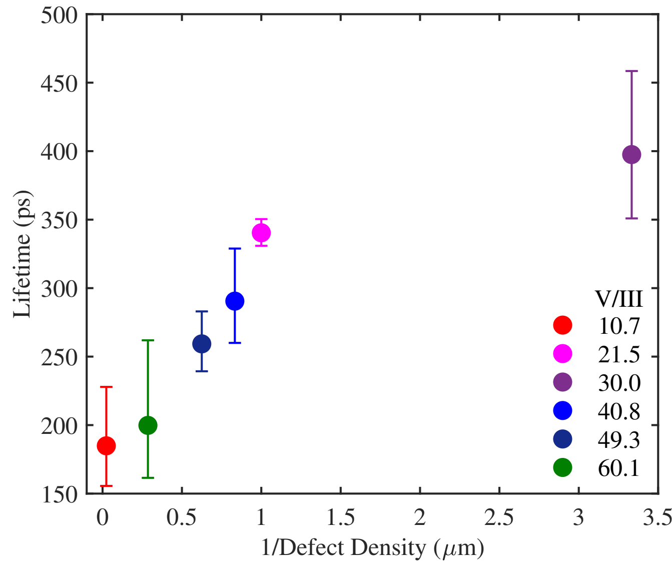

Figure 5.6: Photoconductivity lifetimes of nanowires with different V/III ratios ranging from 10.7 to 60.1 are shown in relation to the inverse of their respective defect densities, which were determined by TEM: the lifetime correlates with the inverse of the defect density. The presence of fewer stacking faults results in longer lifetimes.

bandgap, electron and hole can recombine radiatively without the need of a phonon, in order to conserve momentum. This changes the recombination from a three-particle into a two-particle interaction and reduces the lifetimes [56, 78] (More information can be found in Section 2.2.2).

Both defect density and photoconductivity lifetime seem to be dependent on the V/III ratio during MOVPE growth. In order to determine a possible correlation between these two parameters, the photoconductivity lifetime is plotted against the inverse of the defect density in Figure 5.6. Each dot is colour-coded and represents a different sample from the single-step series. All samples follow a monotonic trend. When the defect density is high, the lifetime is short. The changes in lifetime due to defects seem to saturate with very high ($42.2\,\mu\text{m}^{-1}$) and very low ($0.3\,\mu\text{m}^{-1}$) stacking fault densities, while the lifetime is quite sensitive to small variations around moderate defect densities ($1.6\,\mu\text{m}^{-1}$-$1\,\mu\text{m}^{-1}$). The saturation means that the lifetime is dominated by some other effect at high stacking fault densities.

Figure 5.6 clearly demonstrates the dependence of lifetimes on the stacking fault density. Furthermore, GaP nanowires fabricated with a V/III ratio of 30.0 can be identified as the best candidate as template for lonsdaleite SiGe shells. They

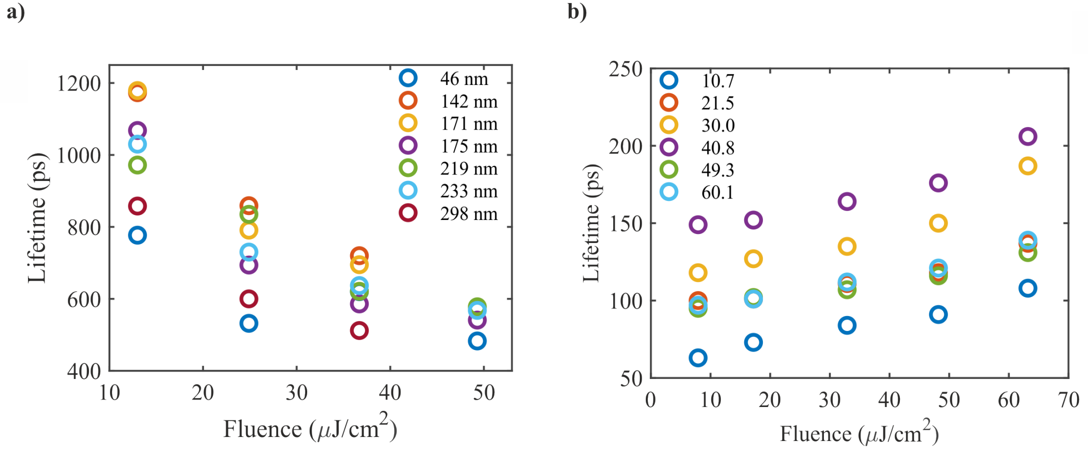

Figure 5.7: Significant disparity in fluence dependence and length of lifetimes for (a) two-step series and (b) single-step series. (a) shows photoconductivity lifetimes, which were extracted by a linear fit of the natural logarithm of the change in THz signal after transmission. The samples from the two-step series have a V/III ratio of 12.2 and diameters varying from 46 nm to 298 nm. The wires were grown in a two-step core-clad process, at which a core of 50 nm is grown first with VLS and then a shell is added through radial VS growth. (b) presents photoconductivity lifetimes, extracted with monoexponential fits from photoconductivity decays. The series consists of GaP nanowires with V/III ratios from 10.7 to 60.1 and a common diameter of 150 nm. All wires were grown in one step with VLS growth.

have a minimal defect density of $0.3\,\mu\text{m}^{-1}$ and the longest photoconductivity lifetime of 398 ps.

While the crystal quality of the samples discussed above is very high, Assali *et al.* [132, 140] have demonstrated GaP nanowires with photoluminescence lifetimes of about 0.8 ns. This value, which was determined with photoluminescence spectroscopy, is more than two times longer than the longest lifetime I have achieved with my samples. To identify the reason for the difference in lifetimes and its effect on GaP nanowires as templates, research on nanowires grown the same way as in Assali's papers [132, 140] has been performed. The results will be discussed in the following section.

5.6 Improved lifetime due to a two-step growth process

In this section I will use THz spectroscopy to investigate the photoconductivity lifetimes of the wurtzite GaP nanowire two-step series and compare it with the

single-step series.

The two-step series was created in the same growth reactor, with the same precursors like the single-step series, but the growth and thus the nanowire properties differ significantly. The GaP nanowires from the two-step series were fabricated in two different steps: axial growth of a 50 nm GaP core, followed by radial growth of the GaP shell. The V/III ratio was 12.2 and the total diameter varied between 46 and 298 nm. The lifetimes of these samples were extracted from their decays taken with THz spectroscopy. The fluence-dependent lifetimes of all seven samples of the two-step series are shown in Figure 5.7a. For comparison, the lifetimes of the single-step series, whose samples were fabricated by axial growth in one step with diameter of 150 nm and different V/III ratios in the range of 10.7 to 60.1, are shown for different fluences in Figure 5.7b.

If the two graphs and the lifetimes of the two different GaP nanowire series are compared, two things become apparent: the photoconductivity lifetimes of the two-step series are around a factor of 10 higher than the photoconductivity lifetimes of the single-step series, and the series' fluence dependence shows opposite behaviour. The samples grown in the two-step process have photoconductivity lifetimes, which decrease with increasing fluence, while the lifetimes of the samples grown in one step increase with rising fluences. The correlation of larger lifetimes with increasing fluences is frequently seen in nanowire samples [86, 148, 149]. At low excitation, the lifetime of carriers is usually limited by monomolecular recombination. The electrons and holes are getting trapped in lattice vacancies or defects. At higher fluences the amount of carriers is increased, but the number of traps is constant. Therefore, traps get saturated and the lifetime increases [112, 148]. A decrease in lifetime with increasing fluence usually happens when recombination starts to get dominated by bimolecular recombination [84, 85]. As described in Section 2.2.3, the recombination rates after excitation can be modelled by rate equation [84]:

$$\frac{dn}{dt} = -k_1 n - k_2 n^2 - k_3 n^3, \tag{5.1}$$

where n stands for the charge-carrier density, k_1 is the recombination rate coefficient for monomolecular decay, k_2 the recombination rate coefficient for bimolecular decay, and k_3 the recombination rate coefficient for Auger recombination, which can usually be neglected until very high charge-carrier densities are reached. This equation shows that bimolecular decay is dependent on the charge-carrier density by the power of two. Therefore, the amount of bimolecular recombinations increases faster than monomolecular decays with higher charge-carrier density. A more detailed discussion about recombination mechanism can be found in Section 2.2.

A change of the dominating recombination process cannot explain the opposite fluence dependence because the excitation fluences were similar for the measurements of both series. Therefore, the disparate growth methods must be responsible for the different behaviour. As mentioned in Section 5.2, more dopants are incorporated during shell growth than during core growth. Unintentional carbon doping was detected in GaP nanowires using atom probe tomography. High doping changes the recombination equation (5.1) to:

$$\frac{dn}{dt} = -(k_1 - k_2 n_0)n - k_2 n^2 - k_3 n^3. \tag{5.2}$$

Where n_0 represents the doping density. (The derivation from the normal rate equation model to the doped one can be found in Section 2.2.2.) The monomolecular recombination ($k_2 n_0$) can also result in radiative decay and increase the radiative efficiency, which also includes bimolecular recombination. The two-step series was grown in two steps: first the core was grown and then the shell around. Therefore, it has a higher doping than the single-step series which was grown as a single-step process. Consequently, radiative recombination dominates for the two-step series, and thus the lifetime decreases with increasing fluence, while non-radiative monomolecular recombination dominates the single-step series.

Not only is the fluence dependence different for both series, but also the lifetimes themselves. The lifetimes of the sample from the two-step series are significantly longer than the ones of the sample from the single-step series. For a better quantification of the difference, one sample from each of the two series are selected

and compared. The two-step series is represented by the sample with a diameter of 142 nm because this value is the closest to the fixed 150 nm diameter of the V/III ratio series. From the single-step series the sample with a ratio of 10.7 is taken because it is similar to the V/III ratio of 12.2 used in the two-step series. Due to opposite correlations between fluence and lifetimes for the two series, the highest lifetime across all fluences is taken for each sample. It is clear from Figure 5.7 though that the lifetimes of the two-step series are constantly higher than the ones from the single-step series. The sample with 142 nm had a photoconductivity lifetime of 1173 ps at 13 μJ cm^{-2}, while the maximum value for the sample with a V/III ratio of 10.7 was 108 ps at 63 μJ cm^{-2} fluence, although the material's morphology, crystallography, and elements are the same. The short lifetimes of the single-step series could result from HCl gas, which was added during growth to suppress tapering. It can create a chlorine passivation layer and affect the surface [142, 150]. Due to the large surface-to-volume ratio the unwanted chlorine passivation has a strong detrimental effect on the GaP nanowires. The two-step series is not affected by it, because HCl is only used during core growth and the shell growth prevents the formation of a chlorine compound on the surface. Therefore, the photoconductivity decays of the samples grown by the two-step core-clad method were not influenced by the added HCl.

After having discussed the two different growth processes for GaP nanowires, the focus will now only be on the effect of diameter on the photoconductivity lifetime. The lifetimes at 13 μJ cm^{-2} are shown for different diameters in Figure 5.8. Except for the outlier sample with 46 nm diameter (red dot), the lifetime decreases with increasing nanowire diameter. This behaviour is not expected. Usually, the lifetime increases with increasing diameter [125]. Due to their large surface-to-volume ratio of nanowires, effects on the surface such as surface traps and defects play a dominant role in nanowires. With increasing diameter, the surface-to-volume ratio reduces, the surface effects are less prominent, and thus the lifetime normally increases (see Section 3.1). These correlations depend on the material and its

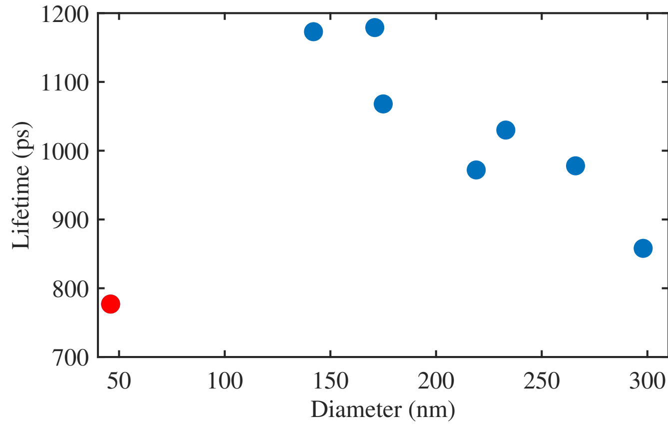

Figure 5.8: The photoconductivity lifetimes in relation to the diameter of GaP nanowires for a fluence of 13 μJ cm^{-2} show a behaviour which is uncommon to these plots due to unintentional doping. The red dot marks the outlier of the two-step series because it was grown in one step. Each y-value was extracted by fitting an exponential decay to the photoconductivity decays. These data corresponds to first column of points in Figure 5.7a.

sensitivity to surface defects, but the lifetime should always increase with increasing diameter as long as no other effects interfere.

However, in the GaP nanowires from the two-step series an effect seems to reverse this correlation: the lifetimes decrease linearly from 1170 ps for wires with a diameter of 171 nm to 858 ps for the sample with 298 nm. The values do not align to a straight line due to the variations of nanowire diameter within a sample. Furthermore, the sample with a diameter of 46 nm is an outlier due to its different growth technique. For the two-step series, a 50 nm core and then a shell was usually grown until the planned thickness was reached. However, the 46 nm sample was only fabricated in one step because its diameter is as big as the core alone. Therefore, the lower lifetime for this sample could be attributed to an incomplete removal of the chlorine layer, which has detrimental effects on the nanowire properties as discussed previously in this chapter. The different growth methods also affect the unintentional doping density. The incorporation of dopants is higher during shell than during core growth, as discussed in Section 2.1.4. Therefore, the doping density of the sample with a 46 nm diameter is much smaller compared to the other samples of the two-step series. They have at least a shell thickness of 90 nm.

As a result, the doping density seems to affect the photoconductivity lifetimes of the nanowires more than recombinations on the surfaces. Therefore, the photoconductivity lifetime of the samples from the two-step series decreases with increasing diameter.

5.7 Summary

In conclusion, wurtzite GaP nanowires with a direct bandgap were characterised to obtain a better understanding of the template for the lonsdaleite SiGe shells. Furthermore, the degradation of the wires during THz spectroscopy, and storage under nitrogen environment and air was discussed. Additionally, the stacking fault density was correlated with nanowire lifetime characterised by THz measurements. When the defect density is lower, the lifetime is longer. The sample with a V/III ratio of 30.0 was determined to be the best template because it has the lowest defect density of $0.3\,\mu\text{m}^{-1}$ and the longest lifetime (398 ps). Unfortunately, these nanowires have a chlorine passivation layer, which decreases the lifetimes. The harmful passivation layer is likely removed if the two-step core-clad method is used for nanowire fabrication. Therefore, this growth technique can be recommended for the fabrication of GaP nanowires as template for the growth of a Si or SiGe shell in lonsdaleite phase. Furthermore, the shell growth in the two-step process causes a high doping density changing the fluence-dependent behaviour of the lifetimes compared to the single-step series.

6 Lonsdaleite phase Si and SiGe nanowires

6.1 Efficient silicon optoelectronic applications

"If an all-silicon laser could be created, it would revolutionize the design of supercomputers and lead to new types of optoelectronic devices" (Brian Libby) [151]. Silicon plays an important role in everybody's life. Most of our current technology is fabricated from silicon, which is abundant, cheap and one of the most researched materials. Already in 1996 the price of one transistor was lower than for printing one letter on paper [152]. The major drawback of silicon is its indirect bandgap [153]. This decreases the probability of radiative recombination, and thus the material is very inefficient in optoelectronic devices. However, these are needed more than ever to speed up computer performance and reduce power consumption [154, 155].

Much research has been performed on achieving a way to create efficient optoelectronic devices based on existing silicon-based technology. There are five different main approaches to create these devices:

Firstly, silicon can be doped with rare earths like erbium [156]. The localisation of the electrons and holes around the impurity centres enables the carriers to recombine without the need of a third particle. However, the doping concentration is limited due to the solubility of the dopants [81].

Secondly, quantum confinement can be used to increase the light emission efficiency. It raises the energy levels and the wavefunction has a larger dispersion, increasing the probability of radiative instead of non-radiative recombination. Furthermore, the scattering at the adjacent borders can provide the momentum needed for an indirect bandgap transition [81, 157, 158].

Quantum confinement is also important for the third option: to create an efficient optoelectronic device made of porous silicon. This material shows strong photoluminescence with a tunable absorption edge *circa* 0.5 eV above the silicon bulk value. Compared to direct bandgap materials, the peak intensity is lower and the lineshape broader due to size fluctuations of the porous material. However, the total PL intensity is similar to the total PL intensity of III-V materials [81, 153, 159].

Fourthly, silicon can be alloyed with another element or compound to create a direct bandgap. Optoelectronic devices made of III-V compounds have a high radiative efficiency due to many having a direct bandgap and they would be a good candidate. However, combining III-V and silicon as alloys or junctions can be detrimental for the overall device. There is a polar-nonpolar mismatch and the lattice constants are different for silicon and III-V compounds, causing defects and dislocations, and thus enabling non-radiative decays and short circuits in devices [81]. Furthermore, cross- and transfer-contamination between silicon and the III-V semiconductor when fabricated within the same system can occur causing defects and reducing the device performance. This increases the complexity of fabrication and the device cost [96].

It is much more beneficial to alloy silicon with germanium, which is completely miscible with silicon [160] and can be fabricated without cross-contamination at high crystal quality. The electron mobility is increased by the covalent bonds between silicon and germanium [96]. The absorption coefficient is increased, and the effective mass reduced [81, 161]. Furthermore, SiGe alloys can be tailored in composition for certain applications, such as detecting or emitting photons at 1.5 μm (0.8 eV), which is the optimum wavelength for optical fibres [151, 162]. However, it remains an indirect bandgap material.

The fifth option for efficient silicon devices is based on the engineering of the band structure independent of uncontrollable factors like strain and impurities. A direct bandgap in a silicon-based alloy, which can be easily integrated into modern Si-based fabrication processes, is very promising for efficient optoelectronic devices. Therefore, much theoretical work has been done on this special crystal phase, but there is still a lack of experimental research. A direct bandgap has not been experimentally proven so far.

In this chapter Si and SiGe grown in the lonsdaleite phase were investigated by THz spectroscopy, with further analysis of their electrical properties and bandgap information. The surface recombination velocity of lonsdaleite silicon was characterised and evidence was found for a direct bandgap. This study aims to create the first electrically driven direct bandgap SiGe nanowire laser, which can be directly integrated onto a silicon chip.

6.2 The lonsdaleite phase

Lonsdaleite is a special crystal structure, also known as the hexagonal diamond structure. It consists of two interpenetrating hexagonal close-packed lattices [60], as shown in Section 2.1.3. Therefore, lonsdaleite silicon (germanium) is also called hexagonal silicon (germanium).

In the 1960s lonsdaleite carbon was first found in meteorites. It was created due to the high pressure and temperature, to which the meteorite was exposed to [46, 47]. Other group IV materials were subsequently found to enable growth in this crystal structure.

Silicon and germanium have many different crystal phases (e.g. diamond cubic phase or the rhombohedral phase r8) [57, 63, 163, 164, 165, 166], but the lonsdaleite phase is one of the most promising structures because it may create a direct bandgap material in the fourth periodic group. The theoretically calculated band structures of germanium and silicon grown in lonsdaleite phase instead of the cubic phase are shown in Figure 6.1. For silicon, the energy gap decreases from 1.1 eV to 0.95 eV, but it is still indirect [167, 168]. However, germanium is supposed

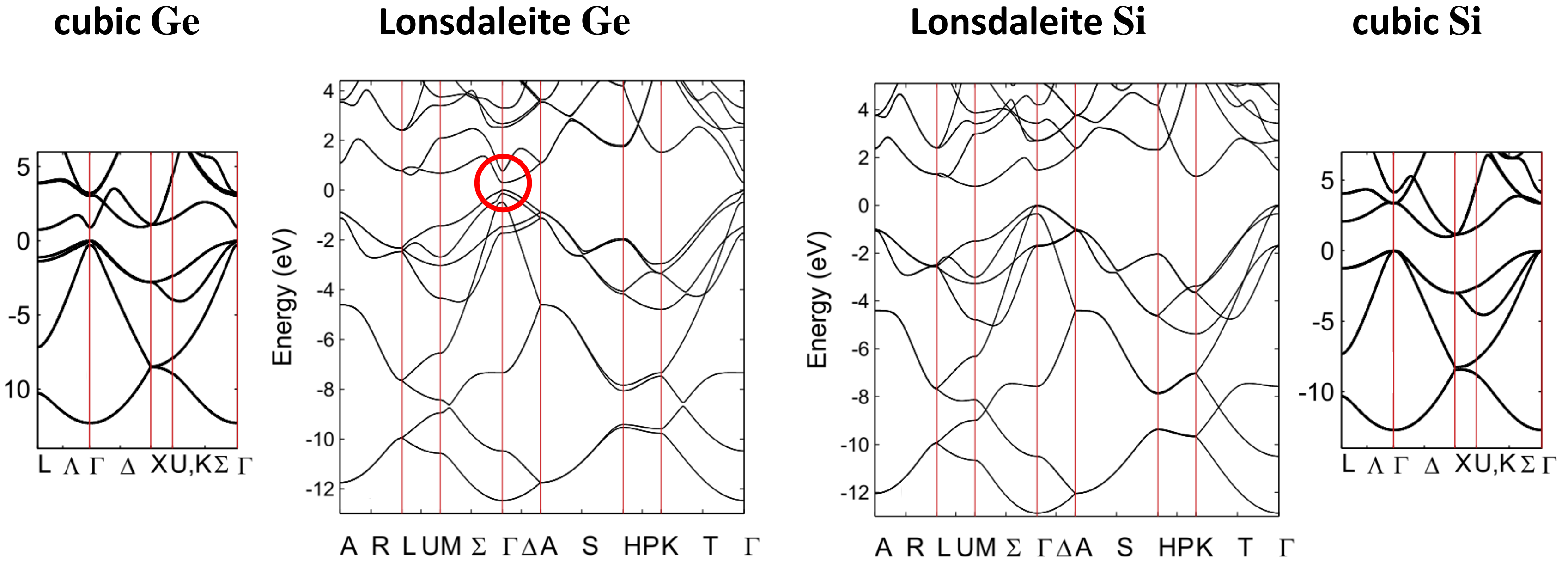

Figure 6.1: Theoretically calculated band structure of cubic germanium, lonsdaleite germanium, lonsdaleite silicon, and cubic silicon. For the lonsdaleite phase the direct bandgap is smaller than for the same material in cubic phase. Lonsdaleite germanium is the only group IV material with a direct bandgap (red circle) in this special crystal structure. Adapted from Ref. [60].

to become a direct bandgap material [60]. By mixing lonsdaleite silicon and germanium, a compound could be formed with a direct bandgap, whose energy can even be tailored [49, 53, 54, 57, 169]. Cartoixá *et al.* predicted a direct bandgap for SiGe with a germanium content of 35% or higher [170]. Furthermore, Rödl *et al.* predicted that for a biaxial strain of more than 4% a direct bandgap lonsdaleite silicon is possible [168].

Since the first natural lonsdaleite crystals were found in meteorites, many different processes have been applied to artificially create silicon and germanium in this phase. For example, a high pressure was applied to cubic silicon in a diamond anvil cell, in order to achieve lonsdaleite crystals [171]. In another method microcrystallites were deposited during laser ablation of SiO_2 films [172]. Even silicon nanowires have been grown in lonsdaleite structure with either the plasma-assisted VLS method [173] or with VLS growth [174]. Some papers reported, boron being added during fabrication to stimulate nanowire growth in the wurtzite phase [175, 176]. However, all these methods create samples which are only partially in lonsdaleite phase.

The fact that, especially in the beginning, lonsdaleite structures only existed in micrometre-sized areas, made it hard to verify and distinguish the lonsdaleite structure from other structures [177]. It was difficult to identify this crystal phase with TEM diffraction patterns because the peaks which are supposedly caused by lonsdaleite phase could also originate from defects in cubic silicon, such as microtwins and nanotwins [45, 178]. Nemeth *et al.* even claimed that lonsdaleite phase does not exist [179].

However, Hauge *et al.* [45] managed to fabricate silicon shell nanowires which are uniformly in a stable lonsdaleite phase, by using a new growth technique, a crystal-phase transfer method. Therefore they were able to unambiguously characterise the lonsdaleite phase for silicon. Si and SiGe nanowires in the lonsdaleite phase grown by this crystal-phase transfer method will be discussed in the following sections.

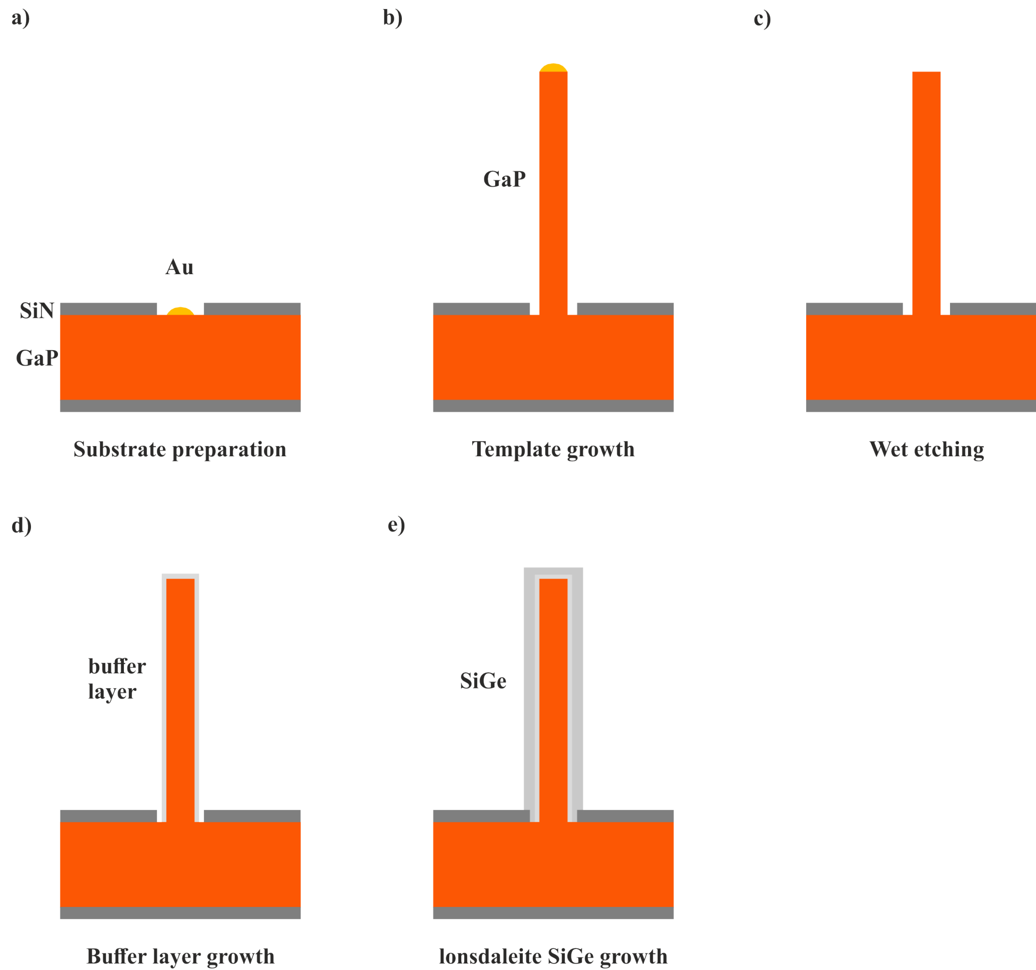

Figure 6.2: Sketch of the fabrication process of lonsdaleite SiGe nanowires: (a) Substrate preparation by patterning the GaP substrate covered by a SiN_x layer with holes, and by casting gold droplets as catalyst. (b) Fabrication of GaP nanowire template with two-step core-clad growth. (c) Removal of gold catalyst by wet etching. (d) VS growth of $Si_{0.86}Ge_{0.14}$ shell as a thin buffer layer to decrease lattice mismatch between GaP and Ge. (e) Growth of SiGe shell in lonsdaleite phase.

6.3 Fabrication of Si and SiGe in the lonsdaleite phase

All samples in this chapter were fabricated by Yizhen Ren in Professor Erik Bakkers' group at the University of Eindhoven using a low-pressure (50 mbar) Aixtron CCS-MOVPE. Growing Si and SiGe nanowires in lonsdaleite phase requires many steps, which are discussed in the following based on Figure 6.2. These materials can only be prepared when grown around a template in the hexagonal crystal structure. In

this case wurtzite GaP nanowires, which were discussed in Chapter 5, were chosen because the lattice constants of GaP and Si match [180, 181]. These heterostructured nanowires could generally be named GaP/Si(Ge) core-shell nanowires. However, the GaP core is only a template. For simplicity they are called Si or SiGe nanowires without mentioning the GaP core specifically, and every time when the lonsdaleite materials are discussed this refers to the shell, not the whole nanowire.

In the case of SiGe nanowires, a GaP(111)B wafer was first prepared as substrate (Figure 6.2a. It was covered with 50 nm SiN_x to prevent diffusion of the phosphor into the wires. Holes with a diameter of 250 nm and a pitch of 500 nm were created via nanoimprinting. The holes were filled with a gold layer, which acts as catalyst later. Secondly, (Figure 6.2b GaP nanowires in the wurtzite phase with a V/III ratio of 21.5 were grown with the two-step core-clad procedure until they reached a diameter of 190 nm. More details about GaP growth can be found in Section 5.2. After the gold catalyst had been removed by wet etching (diluted KI/I_2 solution), the sample was loaded into the CCS-MOVPE again and a 14 nm thick $Si_{0.86}Ge_{0.14}$ layer was grown around the wurtzite GaP core, adopting its crystal structure (Figure 6.2d). In a final step, (Figure 6.2e), the SiGe alloy in the lonsdaleite phase was grown using disilane (Si_2H_6) and germane (GeH_4) as precursors. The interlayer between the GaP core and $Si_{1\text{-}x}Ge_x$ acts as a sacrificial buffer layer to trap any gallium or phosphor from the core. It also decreases the strain caused by the different lattice constants of the target heterostructure. GaP was chosen as core material because of its lattice match with silicon, but the lattice constants of GaP and germanium are mismatched by 4% [180, 181]. Therefore, SiGe composites with higher silicon content are easier to grow strain free.

For the Si thickness series no buffer layer was used. The GaP core has a diameter of 135 nm and a length of 10 μm. The Si shell, which was grown at 900 °C with Si_4H_{10} as precursor, varies from 23 nm to 260 nm. Two different sets of the same series were grown. The fabrication steps are the same for both series, only the gold catalyst removal process was improved for the second series because this step had deteriorated the nanowire quality of the first silicon thickness series.

Ge content [%]	shell thickness [nm]
90	855
81	855
70	405
60	130
50	100
40	82

Table 6.1: Sample description of the $Si_{1\text{-}x}Ge_x$ nanowire series: the germanium content and the shell thickness are given for the six samples.

Studies on the crystal structure of the GaP core and on the uniform shell in the lonsdaleite crystal phase can be found in reference [45] for the Si nanowires and in reference [182] for the SiGe nanowires.

All core-shell nanowires were analysed and characterised under vacuum by THz spectroscopy at room temperature. The samples were prepared by transferring the wires onto a parylene-coated quartz disc, which is transparent for THz radiation [129] and which increases the nanowire density due to their adhesion to the polymer. The samples were excited by laser pulses (wavelength of 800 nm, 35 fs pulse duration), and excitation fluence was varied between 34 μJ cm^{-2} and 1229 μJ cm^{-2}.

6.4 Lonsdaleite phase SiGe nanowires with different Ge contents

A series of $Si_{1\text{-}x}Ge_x$ nanowires grown in the lonsdaleite phase around a GaP template were investigated with THz spectroscopy, which was explained in Chapter 3. The series consists of six samples with a germanium content between 90% and 40%. Each sample has a 190 nm thick GaP core, but the SiGe shell in thickness varies, as can be seen in Table 6.1. The total diameter is the sum of the core diameter and of two times the shell thickness.

Photoconductivity decays were taken for each sample and their lifetimes were extracted with a monoexponential fit. Figure 6.3a shows the fluence dependence of the sample with $Si_{0.19}Ge_{0.81}$ nanowires on a semilogarithmic scale. The lifetime increases significantly from 795 ps to 1498 ps when changing the excitation fluence

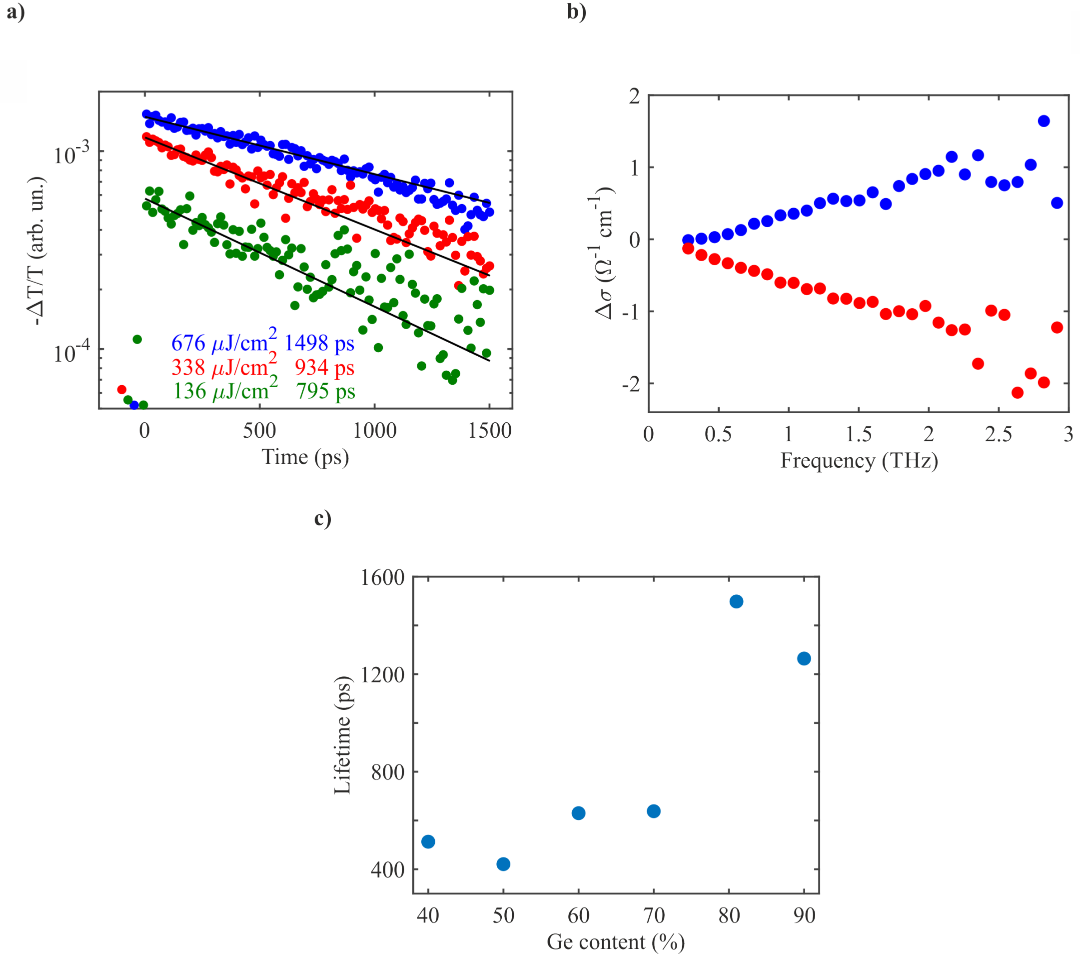

Figure 6.3: (a) Photoconductivity decays of $Si_{0.19}Ge_{0.81}$ nanowires reveal trap saturation for higher fluences. (b) The imaginary (red) and real part (blue) of the frequency-dependent photoconductivity of $Si_{0.5}Ge_{0.5}$ nanowires at 676 μJ cm^{-2} indicate a high doping density. (c) Lifetimes, which were extracted at 676 μJ cm^{-2} for SiGe wires with different germanium contents, do not confirm the theoretically-predicted direct bandgap.

from 136 μJ cm^{-2} to 676 μJ cm^{-2}. The lifetimes become longer with higher fluence because the photoinjected charge-carrier density increases. Therefore, traps can be saturated and more carriers recombine unaffected by traps. Consequently, the significant changes in lifetime indicate a large number of traps.

Furthermore, a high doping density is found in the $Si_{0.5}Ge_{0.5}$ nanowires (Figure 6.3b. The THz photoconductivity spectra, measured at a fluence of 676 μJ cm^{-2}, determines the frequency-dependent real (blue) and imaginary (red) parts of the photoconductivity of nanowires. Theoretically, these data can be fitted with the surface plasmon model to extract charge-carrier density, doping density, scattering

time and mobility. The measured frequency-dependent photoconductivity spectrum should show the plasma frequency $\omega_0 = \sqrt{g\frac{Ne^2}{\epsilon_0 m^*}}$ (see Equation 3.8). The plasma frequency can be extracted from the graph by taking the frequency at the position where the imaginary part of the photoconductivity becomes positive. However, this plasma frequency in Figure 6.3b is beyond the observable spectral range of 3 THz. The bending of the imaginary part towards the positive range is not even noticeable. The spectrum looks more like a "scissor" than the expected shape for a typical semiconducting nanowire, which is shown in Section 3.1 Figure 3.7. The "scissor"-like shape of photoconductivity likely originates from a very high doping density in $Si_{1-x}Ge_x$. Despite the high density of dopant, defects and traps, it should still be possible to see indications for a direct bandgap in this series.

Theoretically, hexagonal $Si_{1-x}Ge_x$ could become a direct bandgap if the germanium content exceeds a certain threshold. This threshold has not been experimentally determined so far and theoretical calculations have predicted different values.

In order to extract the threshold between indirect and direct bandgap materials, the lifetimes of the $Si_{1-x}Ge_x$ series were plotted against the germanium content at 676 μJ cm^{-2}, as can be seen in Figure 6.3c. Lifetimes for direct bandgap materials are shorter than for the same material with an indirect bandgap [140] because a third particle is involved to conserve the law of momentum for radiative recombinations. Therefore, a decrease in photoconductivity lifetime with rising germanium content is expected. In my experiments, it is found that $Si_{1-x}Ge_x$ nanowires with germanium contents between 40% and 70% have short lifetimes between 421 ps and 638 ps, while the lifetimes of the samples with 81% and 90% Ge (1498 ps and 1264 ps, respectively) are three times longer.

There are several different reasons which could explain why these observations contradict theoretical calculations. For example, the nanowires may not have been grown uniformly in the lonsdaleite phase resulting in an indirect bandgap for all germanium contents. It is also possible that the higher lifetimes for the samples with 81% and 90% germanium content indicate that another unknown effect is prominent. This effect could, for example, be the different nanowire diameters

for each sample because this is the only parameter, except for the germanium content, which changes significantly. $Si_{1-x}Ge_x$ nanowires with 81% and 90% Ge have the largest Si shell of 855 nm, while for the other samples, the shells decrease from 405 nm to 82 nm. Nanowires have a large surface-to-volume ratio. So the surface with its defects and traps largely affects the lifetime. When the nanowire diameter is smaller, the surface-to-volume ratio is bigger, resulting in a shorter lifetime compared to the same nanowires with bigger diameters.

Therefore, the direct bandgap of hexagonal SiGe could not be proven with the current data, but further steps have been taken. Firstly, the THz setup was upgraded to achieve a longer bandwidth. Secondly, the growth of lonsdaleite phase nanowires was improved to enable the fabrication of a more homogeneous series of nanowires with reduced unintentional doping. Therefore, THz spectroscopy was performed on lonsdaleite phase silicon to understand the correlations between growth and nanowire performance better and to analyse their optoelectronic properties.

6.5 Defects and their influence on electrical properties in lonsdaleite Si

Ideally, silicon in the lonsdaleite phase can be grown strain-free around the wurtzite GaP template, because the lattice constants are matched. However, the nanowire surface is not uniform and smooth, thus side nanowires grow from it (called parasitic growth). To get a better understanding of these highly defective lonsdaleite Si nanowires, the effect of different morphologies are investigated using THz spectroscopy. Three hexagonal Si nanowire samples were grown with the same recipe in the same MOVPE system. They all had the same silicon shell thickness of 70 nm around a 135 nm wurtzite GaP core. Despite the same fabrication method, the quality of the samples varied significantly: the sample called H05673 showed barely any sign of parasitic growth, while H05679 showed more, and the third sample H05677 was a branched nanowire sample. The discrepancy in quality can be seen in the SEM pictures, which were taken by Yizhen Ren at the University of Eindhoven, in Figure 6.4a, 6.4c, and 6.4e. On the right of each picture, the

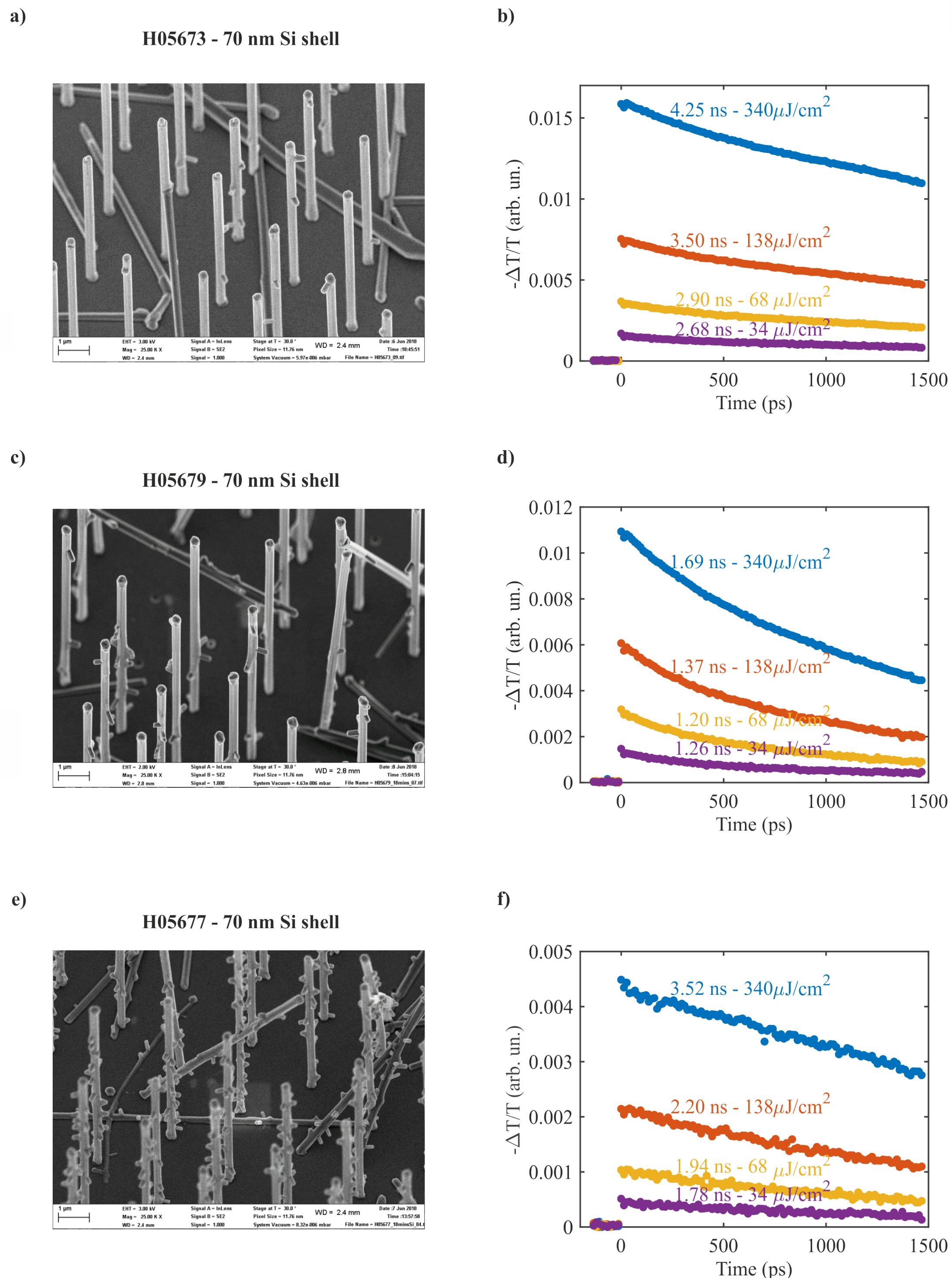

Figure 6.4: The importance of morphology on nanowire properties is shown by three nanowire samples with a 135 nm, wurtzite GaP core and a 70 nm silicon shell in lonsdaleite phase. All samples were grown the same way. However, the morphology of each one of them is quite different. (a) Sample H05673 consists of straight nanowires, with a small amount of parasitic growth. (c) Sample H05679 displays more side nanowires and (e) sample H05677 is dominated by parasitic growth. The photoconductivity decays are always on the right of the corresponding SEM pictures, which were taken by Yizhen Ren.

corresponding fluence-dependent photoconductivity decays characterised by THz measurements can be seen (Figure 6.4b, 6.4d, and 6.4f). The parasitic growth is caused by the residues of the gold droplet, which was used as catalyst for the growth of the GaP core. The droplet is removed by wet-etching. However, some gold residues seem to be left on the side facets of the GaP nanowires. Therefore, the etching process and its lack of reproducibility appears to be the limiting factor for controlled growth of lonsdaleite Si nanowires.

In THz spectroscopy measurements, the fluence was varied between $34\,\mu\mathrm{J\,cm^{-2}}$ and $340\,\mu\mathrm{J\,cm^{-2}}$ and the lifetimes were extracted by monoexponential fits. For each of the three samples, the lifetimes increase for higher fluences because the larger density of charge-carriers saturates traps. This is an indication of a high density of defects.

Furthermore, the change of photoconductivity lifetime depending on the excitation fluence varies for each sample indicating a different quantity and quality of traps and defects. The sample with the lowest parasitic growth (H05673) has the highest lifetime of 4.25 ns at $340\,\mu\mathrm{J\,cm^{-2}}$ due to its uniform morphology. The lifetime decreases by 37% if the highest and the lowest fluence are compared. This change is larger than the 25% for the sample with medium parasitic growth (H05679), which has the shortest lifetime (1.69 ns at $340\,\mu\mathrm{J\,cm^{-2}}$) of all three samples. This is usually an indication that this sample has the most defects. However, according to the SEM pictures, the sample with the worst morphology is H05677. It has the largest change of lifetime with a reduction of 40% between $340\,\mu\mathrm{J\,cm^{-2}}$ and $34\,\mu\mathrm{J\,cm^{-2}}$. The lifetime at $340\,\mu\mathrm{J\,cm^{-2}}$ is with 3.52 ns higher than that of sample H05679, which has medium parasitic growth. The fact that the highest lifetime is not correlated to the lowest fluence dependence could mean that not only parasitic growth is different for the samples, but that they also have different amounts of defects independent of the side nanowires.

In conclusion, it was shown that certain morphology is detrimental for efficient long-lived nanowires. The best-grown sample has a 2.5 times higher lifetime, than samples with abundant parasitic growth. However, defects, which appear

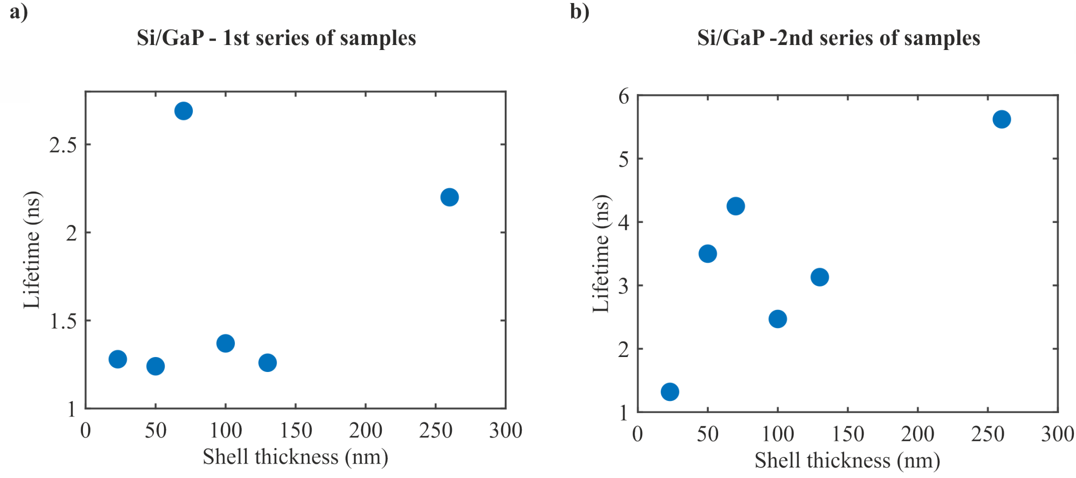

Figure 6.5: Shell thickness-dependent lifetimes of the (a) first series of the hexagonal Si thickness-dependent series and (b) the second series after wet-etching was improved to reduce parasitic growth.

independently of the morphology can also be detrimental for the nanowires and cause a strong fluence dependence of the lifetime.

6.6 Surface recombination of hexagonal silicon

In the following, the surface recombination velocity for lonsdaleite silicon nanowires is studied. The surface recombination velocity quantifies the influence of the surface on the recombination mechanism, and thus on the radiative and non-radiative lifetimes. It is a material-dependent parameter, which is essential for device fabrication because the semiconducting nanowires are more sensitive to the surface than bulk semiconductors due to their high surface-to-volume ratio. The surface recombination velocity S, which is discussed in Section 3.1.3, is correlated to the inverse of the lifetime and the diameter of the nanowire (see Equation 3.4). Nanowires with a large diameter have a longer lifetime than the same wires with a smaller diameter.

To extract the surface recombination velocity, which is defined in Section 3.1.3, THz spectroscopy was performed on the lonsdaleite silicon nanowire thickness series. From the fluence-dependent photoconductivity decays, lifetimes were extracted by monoexponential fits. The results from the decays at around $320 \pm 5\,\mu\text{J}\,\text{cm}^{-2}$ are shown in Figure 6.5a.

The plot does not follow the expected trend for a thickness-dependent series. The lifetime of most samples is around 1.3 ns. Only two samples show different values. This is an indication that another effect is stronger than the influence of the surface on the lifetime. Considering the SEM pictures of this series, the photoconductivity lifetimes are likely dominated by defects caused by growth: parasitic growth, stacking faults, and non-uniformity.

The Si nanowires with a shell thickness of 260 nm show a high photoconductivity lifetime of 2.2 ns, having no parasitic growth but a high stacking fault density. The sample with a 70 nm thick silicon shell has a photoconductivity lifetime of 2.7 ns, twice as high as most other samples. Therefore, the growth for this sample was the best out of the whole series. A closer look was taken at the growth of all samples to determine the reason for the large difference in sample quality, despite all samples were grown the same way, only with different shell thicknesses.

The factor limiting the sample quality was the wet-etching process of the gold catalyst after fabrication of the GaP core, as discussed in Section 6.5. This process was improved and the series was regrown. The lifetimes of the second series are shown in Figure 6.5b. The quality of growth is significantly increased and the lifetimes are up to three times higher than for the first series. Furthermore, the lifetimes are dominated by surface recombination and the sample with the thickest silicon shell (260 nm) has the longest lifetime of 5.6 ns. With decreasing shell thicknesses, the lifetime decreases until it reaches a minimum for Si wires with a 100 nm thick shell. Then the lifetime of the sample with a 70 nm hexagonal Si shell increases drastically to 4.3 ns. Then it decreases again with declining thickness. Apparently, the three samples with the thinnest shells are influenced by different effects than the other samples. They will be discussed in detail in Section 6.7. Before this, the surface recombination velocity for silicon in the lonsdaleite phase was determined using the lifetimes of the three samples with shell thicknesses between 100 nm and 260 nm.

The photoconductivity decays of the samples with 260 nm, 130 nm and 100 nm are compared to each other in Figure 6.6. In Figure 6.6a, the lifetime is seen to decrease for thinner shells, so apparently the surface has a significant influence

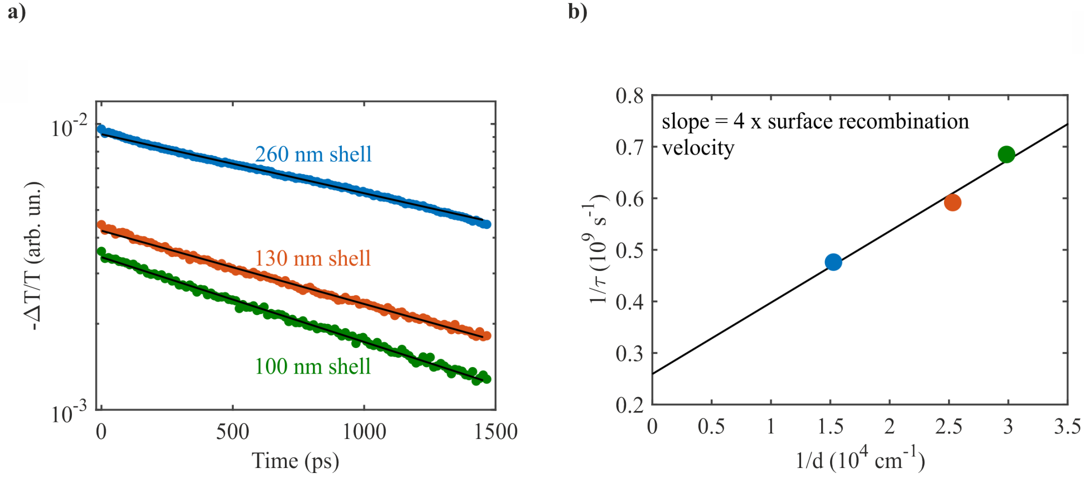

Figure 6.6: (a) Photoconductivity decays of Si shell nanowires with 260 nm (blue), 130 nm (brown), and 100 nm (green) shell around a 135 nm GaP core at a fluence of 138 μJ cm^{-2}. The lifetimes, extracted by monoexponentially fitting (black) the spectra, are 2.10 ns, 1.69 ns, and 1.46 ns, respectively. (b) Plot of the inverse lifetime over the inverse nanowire diameter determines the surface recombination velocity of 3.5 $\times 10^3$ cm/s.

on the nanowire lifetime. The surface recombination velocity is extracted by plotting the inverse lifetime against the inverse nanowire diameter. Then the plot is fitted using a linear function, the slope of which is four times the surface recombination velocity. The surface recombination velocity was determined to be $3.5 \pm 6.7 \times 10^3$ cm/s using Equation 3.4.

This value is of the same order of magnitude as the silicon nanowires in diamond-cubic structure, whose surface recombination velocity is between 1.1 and 1.7×10^3 cm/s [183]. Apparently, the crystal phase does not alter the surface recombination velocity heavily. However, silicon has a 20 times higher surface recombination velocity than InP nanowires (170 cm/s), which are not nearly as much affected by surface defects [125]. Therefore, surface treatment needs to be considered for device fabrication of lonsdaleite Si nanowires. For instance, the influence of the surface could be reduced by passivation with capping layer growth, which has already been proven effective [104, 184].

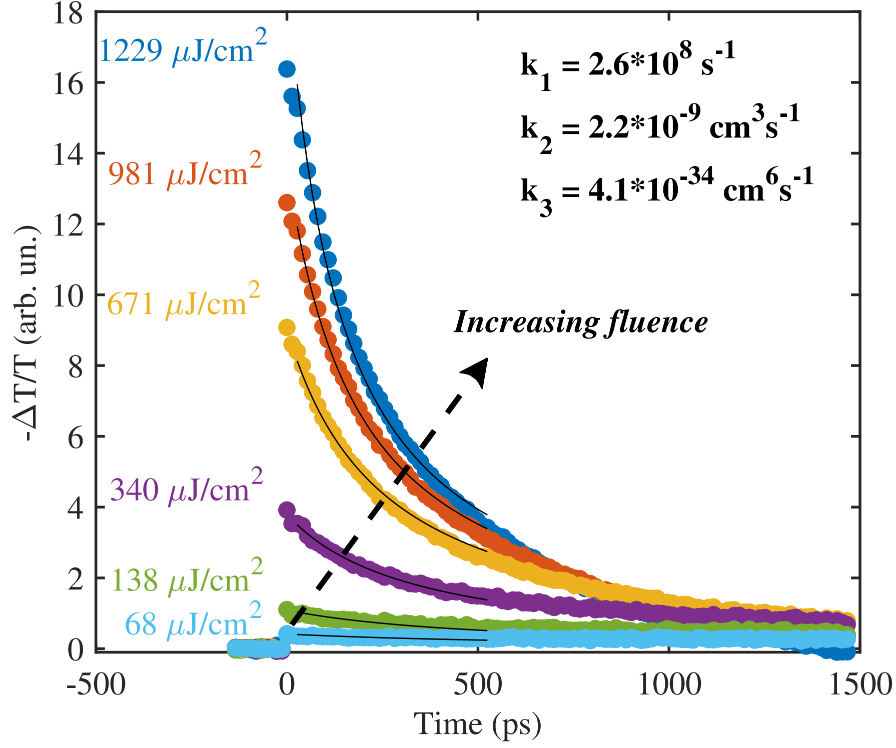

Figure 6.7: Photoconductivity decays of hexagonal silicon nanowires with a 23 nm shell. The scans were globally fitted and coefficients for the rate equation model were extracted. The coefficient for bimolecular decay k_2 indicates a direct bandgap.

6.7 Silicon as direct bandgap material?

I will now discuss silicon nanowires in the lonsdaleite phase, of which THz measurements indicate a direct bandgap for the first time. A direct bandgap is not expected for hexagonal Si because theory predicts an indirect, but smaller bandgap than cubic silicon. However, three samples showed indications for a direct bandgap — lonsdaleite silicon nanowires from the optimised thickness series with diameters of 23 nm, 50 nm, and 70 nm, respectively. Their lifetimes in comparison to the other samples have already been discussed in general in Section 6.6. In the following the focus will be on the sample with a shell of 23 nm because it shows the strongest indication of a direct bandgap.

Photoconductivity decays

Photoconductivity decays of this sample are recorded using laser fluences varying from 68 μJ cm^{-2} to 1229 μJ cm^{-2}. They are plotted in Figure 6.7. The shapes of

the decays alter significantly with fluence. For the lowest fluence, the decay appears to be nearly horizontal, while for the highest fluence the slope is very steep. This kind of behaviour is an indication for a direct bandgap and has been seen before, for example in metal halide perovskites semiconductors [84, 85].

The same experiment was also performed on pure GaP nanowires as control. No signal could be obtained with the same setup parameters as for the measurements with GaP-core Si-shell nanowires. The wavelength of the pump pulse had to be changed from 800 nm to 400 nm by frequency doubling, before a signal could be obtained from the GaP nanowire sample. Therefore, I conclude that the GaP core had no influence on the measurements performed on hexagonal silicon.

A closer look at Figure 6.7 reveals that the photoconductivity decays measured at higher fluences cross the decays measured at lower fluences at around 600 ps after photoexcitation. Theoretically, these crossings should not be possible due to the following reason:
The measurement at the higher fluence has a higher charge-carrier density in the beginning. The density decreases exponentially. Therefore, the carriers of the measurement at a higher fluence will be the same as the one at a lower fluence at some point after photoexcitation. When the carrier densities of two different measurements reach the same value, they should be governed by the same laws and behave exactly the same. Therefore, no crossing of the scans should be possible. However, a crossing of the scans can occur if the experimental settings are not constant, if e.g. the refractive index of the sample changes at high fluences, thus elongating optical path length of the THz pulse.

The signal from the nanowires was small because the active material was only 23 nm thick. To optimise the signal, the photoconductivity decay was not measured at the maximum of the THz pulse, but at the maximum of the ΔT peak, which gives the difference between the THz pulses with pump beam on and off. A timing diagram with these values is depicted in Figure 3.8. However, the refractive index changes for high fluences and carrier densities. Consequently, the optical path of the THz beam passing through the sample increases and the THz pulse is measured

by the gate beam at a different position. A more detailed discussion about this phenomenon can be found in Section 3.1.3. The carrier density and signal are significantly higher for the photoconductivity decays at higher fluences. Therefore, the refractive index and the optical path of the THz pulse change more than for scans at lower excitation power. This results in a shift of the pulse position, at which the signal is measured, and thus in a crossing of the photoconductivity decays for times larger than 600 ps. However, the change in refractive index does not explain the uncommon behaviour of the hexagonal silicon sample with 23 nm shell thickness.

Interpretation

In this following section, I will discuss the recombination processes of the sample with a 23 nm shell, which indicate a direct bandgap. The change from very long lifetimes to very short lifetimes with increasing fluence is usually caused by a change of the dominant recombination method. At low fluences and low carrier densities, respectively, monomolecular recombination dominates, but this is displaced by bimolecular decay at higher fluences and larger carrier densities. In most cases, the lifetime increases with higher fluences due to trap saturation, as discussed in section 6.5. It could be that the behaviour observed for hexagonal silicon with small thicknesses has not be seen before, because the photoconductivity decays were taken at a lower fluence than previous studies on nanowires. To exclude this possibility, I took THz photoconductivity decays of InP nanowires, which have a direct bandgap, at fluences up to 1229 μJ cm^{-2}. However, for this sample the lifetimes stay constant with increasing fluence.

The strong decrease in lifetimes with increasing laser fluence has been seen before in metal halide perovskites [85], whose lifetimes are dominated by bimolecular decay. To verify if this recombination mechanism also dominates the hexagonal Si sample — which would be a strong indication for a direct bandgap — the photoconductivity decays were globally fitted with the rate equation:

$$\frac{dn}{dt} = -k_1 n - k_2 n^2 - k_3 n^3, \tag{6.1}$$

Material	**bandgap**	$\mathbf{k_2}$ **[cm^3/s]**	**Ref.**
GaAs	direct	7.2×10^{-10}	[185]
n-doped GaAs	direct	3.5×10^{-10}	[186]
InAs/InAlAs NW	direct	1.4×10^{-10}	[187]
InP NW ZB	direct	2.0×10^{-9}	[188]
InP NW WZ	direct	1.1×10^{-8}	[188]
SiC	indirect	2.5×10^{-15}	[189]
Si	indirect	1.1×10^{-14}	[190]
Si	indirect	9.5×10^{-15}	[191]
crystalline Si	indirect	4.7×10^{-15}	[192]

Table 6.2: Rate equation coefficients for different direct and indirect bandgap semiconductors.

where n represents the charge-carrier density, k_1 the recombination rate coefficient for monomolecular decay, k_2 that for bimolecular decay constant, and k_3 that for Auger recombination. A detailed discussion is given in Section 2.2. The fit was only performed from the highest point of $\Delta T/T$ to 500 ps, in order to not be influenced by the crossings of the scans.

The rate equation coefficients were determined to be

$k_1 = 2.6 \times 10^8\,1/\mathrm{s}$

$k_2 = 2.2 \times 10^{-9}\,\mathrm{cm}^3/\mathrm{s}$

$k_3 = 4.1 \times 10^{-34}\,\mathrm{cm}^6/\mathrm{s}$.

The order of magnitude of the radiative recombination coefficient k_2 is a strong indication that the lonsdaleite silicon sample has a direct bandgap, as indeed the comparison with other semiconductors in Table 6.2 shows.

Indirect bandgap materials like SiC or Si have a radiative recombination coefficient at the order of 10^{-14} to $10^{-15}\,\mathrm{cm}^3/\mathrm{s}$, whereas k_2 of direct bandgap materials like InP or GaAs is of the order of 10^{-8} to $10^{-10}\,\mathrm{cm}^3/\mathrm{s}$. Therefore, the lonsdaleite sample with 23 nm shell thickness seems to have a direct bandgap. However, it still needs to be discussed why this sample is so different to the other samples of the thickness-dependent Si series which are dominated by monomolecular decay and trap saturation. Furthermore, hexagonal silicon is supposed to have an indirect bandgap according to theoretical calculations.

Rödl *et al.* calculated the lonsdaleite silicon bandgap under special circumstances, and they concluded that the bandgap will become direct if a biaxial strain of 4% or more is applied [168]. No strain was intentionally applied in my research, but it could have been introduced during growth, since core-shell heterostructures are more sensitive to strain than axial ones [141]. The strain could be stronger for a thinner shell, while it could be released easier for a thicker one [193]. This would explain why the sample with a 23 nm thick shell show strong signs of a direct bandgap, while the samples with 50 nm and 70 nm show a similar, but less strong trend at photoconductivity decays and the samples with diameters of 100 nm or thicker do not show any indication of a direct bandgap.

While a direct bandgap would explain the behaviour of the sample in Figure 6.7, it eventually could have been also influenced by doping. A high enough doping density also results in a strong decrease in lifetime, which can be mistaken for a direct bandgap. As discussed in Section 2.2.3, a high doping density n_0 would change the radiative rate equation to

$$\frac{dn}{dt} = -(k_1 - k_2 n_0)n - k_2 n^2 - k_3 n^3. \tag{6.2}$$

The added factor represents a monomolecular decay, which depends on the doping and the carrier density and can result in a radiative decay. A radiative monomolecular decay increases the fluence-dependent radiative efficiency, as discussed in Section 2.2.3. It can eventually cause or contribute to the observed behaviour.

Rianne Plantenga in Professor Erik Bakkers' group at the University of Eindhoven demonstrated a high doping density for a different sample with a 130 nm shell from the first thickness-dependent series with atom probe tomography. Figure 6.8 shows the content and doping level of the different elements of the Si/GaP core-shell nanowire. A vertical line indicates the transition from GaP core to Si shell. Throughout the whole wire doping due to carbon and oxygen atoms can be observed. Furthermore, Ga and P atoms migrate from the core roughly 10 nm into the silicon shell.

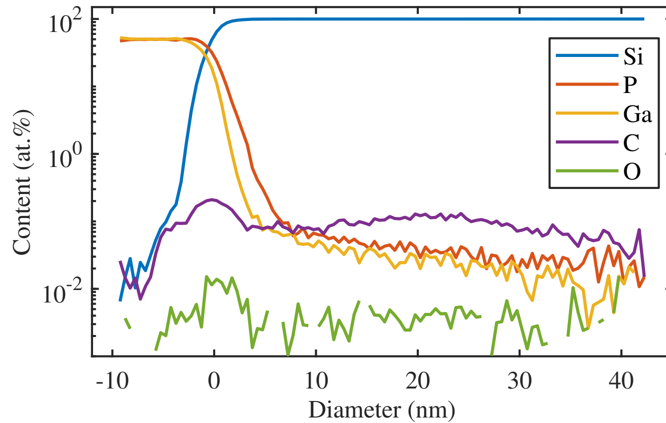

Figure 6.8: Atomic probe tomography on a hexagonal silicon nanowire with a shell thickness of 130 nm from the unoptimised silicon series giving the content of the different materials: the atoms from the GaP core also migrate into the Si shell causing a high doping density for a few nanometres. Furthermore, there is a constant background doping of carbon and oxygen.

I have also taken a THz photoconductivity spectrum of this sample and observed the "scissor"-like shape that was seen for the high density hexagonal SiGe nanowires whose measurement is shown in Figure 6.3. The photoconductivity spectrum scans on other samples from the same silicon thickness series indicate a lower, but still high doping density. The exact density cannot be determined due to the narrow bandwidth of the THz radiation. It can thus be assumed that the sample with a 23 nm thick shell from the second batch, which is characterised in this chapter, has qualitatively, but not quantitatively the same doping as shown in Figure 6.8. The migration of Ga and P atoms into the silicon shell would have a stronger effect on the samples with thinner shells, because the overall doping density of the entire shell would be higher. This could be another explanation for the strong decrease in lifetime with fluence for the sample with a 23 nm shell and the less strong correlation for Si NWs with 50 nm and 70 nm.

To verify, which theory — direct bandgap or doping — dominates the recombination, the photoconductivity decays were not only globally fitted by the (general) rate equation, but also by the rate equation considering doping (6.2). However, independent of the rate equation applied to the decays, the bimolecular recombination coefficient is of the same order of magnitude as other direct bandgap semiconductors'

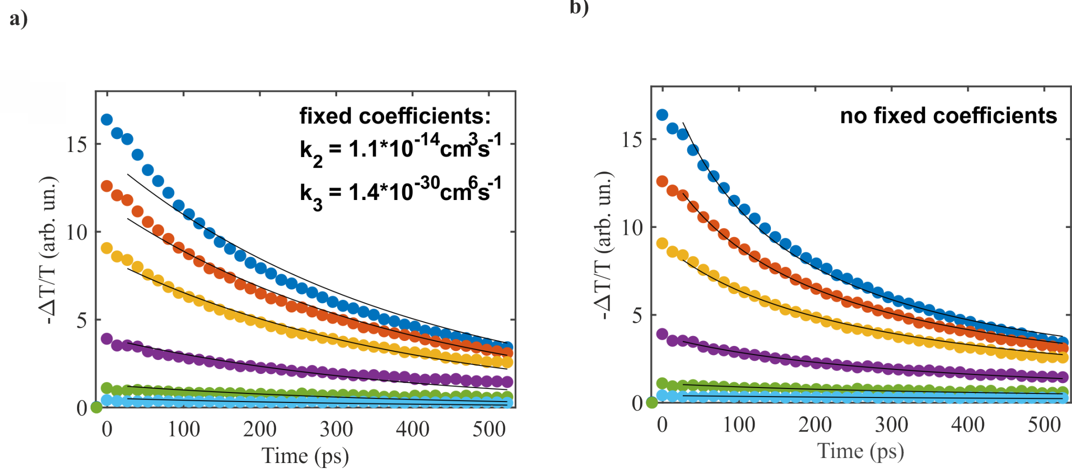

Figure 6.9: The same photoconductivity decays of the hexagonal silicon nanowires sample with a 23 nm shell are globally fitted with rate equation 6.1 while (a) both the bimolecular and Auger recombination rate coefficient and (b) no recombination rate coefficient are fixed at literature values for silicon in cubic phase with indirect bandgap. The fit in plot (b) coincides the best with the experimental data.

(see Table 6.2). In order to confirm the values for the recombination rate coefficients, the photoconductivity decays were also fitted while k_2, k_3 or both had been fixed with literature values [190, 194]. A comparison of different fits and their match with the measured photoconductivity decays is given in Figure 6.9. However, these forced global fits did not properly match the photoconductivity decays.

These calculations confirm that the bimolecular decay coefficient has the same order of magnitude as the direct bandgap materials, and thus it is very likely that the hexagonal silicon has a direct bandgap. Doping was considered as an explanation for the photoconductivity decays, but doping generally does not influence the bimolecular recombination coefficient by orders of magnitude. Lush *et al.* showed that the bimolecular recombination coefficient only decreased from 3.5×10^{-10} cm^3/s to 1.8×10^{-10} cm^3/s for doping densities of around 1.3×10^{17} cm^{-3} and 3.8×10^{18} cm^{-3} [186]. Therefore, it can be assumed that the dopants only support the decreasing lifetimes with increasing fluences, if they decay radiatively, and not cause them.

Photoluminescence measurement

To confirm the direct bandgap, PL spectroscopy was performed on lonsdaleite Si nanowires with a 23 nm shell, which were standing on the GaP substrate, as opposed to the THz measurements, at which the nanowires were lying on parylene-coated

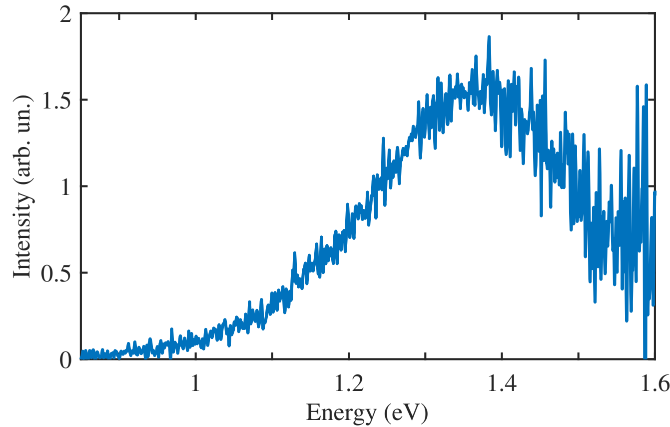

Figure 6.10: Photoluminescence spectrum of hexagonal silicon nanowires with a 23 nm shell at 5 W/cm^2 excitation power.

quartz. This sample fragment was from the same master sample as the nanowires whose photoconductivity decays taken with THz spectroscopy were discussed in this chapter. A 532 nm laser with a power density of 5 W/cm^2 excited the sample, which was cooled down to 4.2 K in a cold finger cryostat. To reduce noise, a lock-in amplifier, triggered by the signal from a chopper running at 3038 Hz, was used for data collection. The Fourier transform infrared spectrometer was used as a detector. Any signal from the scattered laser in the GaP core was cut off by a 780 nm longpass filter. More details about the setup can be found in Chapter 4.

As can be seen in Figure 6.10, the spectrum of the lonsdaleite Si nanowires with 23 nm thick shell exhibits a maximum peak at 1.4 eV. The FWHM of 300 meV is relatively broad. In comparison, the bandwidth of the InAs nanowires in Figure 7.4 is only a few tens of meV.

The peak at 1.4 eV is higher than the direct bandgap of 0.7 eV to 0.9 eV which was predicted by Rödl *et al.* for lonsdaleite Si nanowires which are under a biaxial strain of 4% [168]. However, the PL signal also does not overlap with the bandgap calculated for unstrained, hexagonal silicon nanowires. The energy of their indirect bandgap would be 0.95 eV and the one of the optically forbidden direct gap at 1.63 eV [168]. It could be possible that the optical transition is increased due to quantum confinement in the 23 nm thin silicon shell and the PL signal originates

from direct bandgap silicon. The strain on the shell is very likely not uniform throughout all nanowires. This would explain the broad FWHM of the PL signal.

Conclusion

In summary, the photoconductivity decays of hexagonal silicon with a 23 nm shell show strong indications for a direct bandgap. Theory predicted a direct bandgap for hexagonal silicon with a biaxial strain of over 4% and the global fits to the experimentally measured decays demonstrate a bimolecular recombination coefficient, which is in same order of magnitude as direct bandgap semiconductors.

Dopants eventually cause radiative monomolecular decay, but this would only increase the overall radiative efficiency and not change the bimolecular recombination coefficient significantly. The photoluminescence spectrum does not support the theoretical predicted bandgap, but it does also not negate a direct bandgap because it does not fit to the bandgap of cubic or hexagonal silicon either. Therefore, it can be assumed that the PL originates from the hexagonal silicon's direct bandgap which is shifted to a higher energy due to quantum confinement.

6.8 Summary

In this chapter different SiGe and Si nanowires in the lonsdaleite phase were studied to increase the knowledge of growth, bandgaps, and nanowire properties. The SiGe nanowires had a high doping and trap density. More research on a new generation of improved samples is needed, in order to extract the necessary germanium content for a direct bandgap. The importance of growth technique has also been shown by correlating different morphologies of hexagonal silicon nanowire samples, which were all grown under the same conditions, with their fluence-dependent lifetimes. Furthermore, the etching of the gold catalyst was identified as the fabrication step causing the differences in sample quality and the etching process was improved.

For the realisation of efficient nanowire devices, the surface of the nanowires needs to be considered, because a high surface recombination velocity of 3.5×10^3 cm/s for hexagonal silicon was deduced from the photoconductivity decay measurements of hexagonal silicon nanowires. Therefore, passivation of the samples would be

beneficial for device performance. Furthermore, indications for a direct bandgap for hexagonal, strained silicon were found. This could revolutionise current technology and help developing efficient direct bandgap silicon, optoelectronic devices. However, more research is still needed to confirm the presence of a direct bandgap and clarify the conditions under which it appears.

7

Light emission from InAs-based nanowires

7.1 Introduction to InAs NWs

InAs is an interesting material to study due to its electrical properties and direct bandgap in the mid-infrared region. It has a high mobility, small effective mass, and large g-factor [195]. In nanowire geometry it has the added advantages of low reflectivity and enhanced absorption [39, 184]. This makes InAs nanowires highly desirable for electrical and optical devices like transistors, mid-infrared detectors, LEDs and lasers [3, 14, 34, 196, 197, 198, 199]. Furthermore, InAs has a larger Bohr radius (40 nm) [200] than many other semiconductor materials enabling a strong quantum confinement effect [201], which can increase the radiative recombination rate [38]. If the dimensionality of the wire is reduced below the Bohr radius it can be used for one-dimensional quantum confinement research and devices [91]. However, native surface defects, which can originate from vacancies, antisites, and dangling bonds altering the lattice and band structure of the material [202], usually hinder device applications. In InAs, the Fermi level is pinned above the bandgap due to high energy defects and a narrow bandgap, creating an electron accumulation layer at the surface [72]. This acts like n-doping. It is beneficial for contacting the nanowires for devices or electrical measurements, because it enables an Ohmic contact [195]. However, it can also decrease device performance

under illumination and cause negative photoconductivity [203]. Additionally, the optoelectronic conversion efficiency is reduced due to non-radiative recombination channels at the surface [72].

In contrast to the new areas of hexagonal GaP, Si and SiGe, extensive studies have been performed previously on InAs nanowires because of their superior electrical properties, e.g. high carrier mobility. However, characterisation and optimisation of their optical properties lag behind because many mid- or far-infrared semiconductors have a poor quantum yield compared to materials with visible or ultraviolet bandgaps [204]. Furthermore, spectroscopy in the mid-infrared range is more challenging owing to the limited range of detectors and high atmospheric absorption of this spectral range under ambient conditions [195].

These experimental obstacles were addressed with a home-built cryogenic mid-infrared Fourier transform photoluminescence system, described in Chapter 4. The effect of passivation on electrical and optical properties on two sets of InAs nanowires was investigated. In the first set, InAs nanowires were grown via a MBE system in the group of Professor Anna Fontcuberta i Morral at the École polytechnique fédérale de Lausanne (EPFL). An arsenide shell was grown around the InAs core before Al_2O_3 was deposited with an atomic layer deposition (ALD) system. The second set is a comparison of pure-phase wurtzite and zincblende InAs nanowires with diameters varying from 20 nm to 80 nm, grown via a MOVPE system at the Australian National University (ANU) and coated with ALD Al_2O_3 by Dr. Hannah Joyce from the University of Cambridge. Furthermore, I will explain the effect of antimony doping of InAs nanowires on bandgap engineering. Finally, InAs nanomembranes will be shown as a promising way to create advanced devices with geometries inspired by nanowire-based devices.

7.2 InAs NW passivation

Nanowires have a high surface-to-volume ratio. Hence, charge trapping at surface defects can be detrimental to device performance. To reduce the density of surface

defects, different passivation methods have been tested. In the following, the most promising ones for InAs nanowires will be discussed.

A high percentage of the surface defects of InAs nanowires are associated with the native oxide that forms after InAs has been exposed to oxygen. Etching is one way to remove the undesirable, often detrimental oxide shell. Unfortunately, this not only removes the oxide, but also damages the surface of the InAs causing it to roughen and create more defects [203, 205]. L'Vova *et al.* [206] managed to remove the native oxide layer from InAs without etching by using an aqueous solution of sodium sulphide (Na_2S). The solution simultaneously forms a passivation layer because the sulphur atoms bond to indium atoms.

In another chemical treatment, a self assembled monolayer (SAM) of organic sulphide octadecylthiol (ODT) is formed as protective layer around the nanowires due to the strong chemical bonds between the sulphur atoms and In and As atoms. This method also allows a functionalisation of the surface. However, such passivation is time limited as the SAM decreases under air exposure. Furthermore, fabricating this layer is time consuming and needs an oxygen-free environment and solutions [207].

A very efficient way to achieve effective passivation is the growth of a shell in the same reactor, after nanowire growth has finished. Then the InAs wires are protected before they have ever been exposed to air. Quite often InP is used as shell for InAs nanowires [72, 184, 208, 209]. The valence and conduction bands of InAs and InP build a type-I band alignment [208] helping to keep the charge-carriers away from the surface. With this method, measurable photoluminescence at room temperature has been achieved [184, 208]. The InP passivation does not only enable room temperature emission, but also increases the PL quantum efficiency by orders of magnitude. Jurczak *et al.* [184] have reported a tenfold improvement of PL intensity at 300 K, but only a fivefold improvement at 5 K by adding an InP passivation layer on InAs nanowires. Thermal effects were shown to have less influence on passivated than on unpassivated InAs nanowires. Therefore, the ratio of passivated to unpassivated photoluminescence intensity is temperature-dependent.

With an InAsP shell the photoluminescence was even increased by a factor of 100 at 8 K compared to the unpassivated InAs nanowires. However, there is a lattice mismatch of up to 3.1% which can induce strain [208]. With careful engineering and optimising of the InP shells, strain can be released or compensated.

Another passivation technique for InAs semiconductors avoiding strain uses deposition of atomic layers of Al_2O_3. The advantages of this method are the well-known and easy growth, prevention of oxidation and creation of a type-II band alignment between InAs and Al_2O_3 [210]. Type-II band alignment at a heterojunction spatially separates charge-carriers. For a long time it was challenging either to remove or to prevent native oxides forming before the deposition without roughening the surface. Changing the precursor to the metalorganic precursor trimethylaluminium (TMA) works by removing the native oxide without etching damage or inducing strain due to an oxidation-reduction reaction and creation of a controlled aluminium oxide afterwards [211]. Timm *et al.* have shown that, with this method, for only a 2 nm thick Al_2O_3 layer more than 90% of the native arsenide oxides and up to 90% of the native In oxides are removed [212]. Due to these advantages, this thesis concentrates on InAs nanowires passivated with this technique.

7.2.1 MBE-grown InAs nanowires

7.2.1.1 Growth

The InAs nanowires shown in this section were grown by Dr. Heidi Potts in Professor Anna Fontcuberta i Morral's group at EPFL via a DCA P600 MBE system on GaAs(111)B substrates covered with 4.5 nm of spin-coated silicon oxide. The difference in bandgap between nanowires and substrate allows to distinguish the photoluminescence signals from substrate and wire. Before growth, the substrate was cleaned with buffered oxide etch (7:1) for 20 s and afterwards with a 1:10 solution of 2% hydrogen-silsesquioxane and Methylisobutyl-ketone. Then the substrate was loaded into the MBE and annealed in order to desorb contaminants. The nanowires were grown catalyst-free at a temperature of 520 °C with an arsenic flux

of 1.9×10^{-6} Torr and an indium flux of 1.4×10^{-7} Torr. After growth the sample was cooled down to 100 °C under constant arsenic exposure.

When a sample was passivated with Al_2O_3, a 30 nm thick amorphous arsenic capping layer was grown at a flux of *circa* 1×10^{-5} Torr for 30 minutes. This shell should prevent the InAs nanowires from oxidising. Therefore, its growth happened immediately after the nanowires had been grown and the substrate had cooled to room temperature [69, 213]. Afterwards the samples were transported and loaded into a high vacuum ALD chamber. Then the arsenic capping layer was thermally desorbed by annealing at around 400 °C. For Al_2O_3 growth, the wires were first exposed to a large dose of trimethylaluminium (TMA) and N_2 purge. Then 10 nm Al_2O_3 was grown with TMA and H_2O as precursors at a substrate temperature of 270 °C [214].

In order to study the effect of this passivation, six samples — three passivated with diameters of 105 nm, 123 nm, and 138 nm, and three unpassivated with 102 nm, 110 nm and 137 nm — have been grown. They are in zincblende crystal structure with wurtzite inclusions. In the following, these samples will be referred to as passivated and unpassivated samples with a small, medium, or thick diameter.

7.2.1.2 Passivation effect on optical and electrical properties

Potts *et al.* [69] have previously seen an improvement for Al_2O_3 passivated InAs nanowire transistors over devices using unpassivated nanowires. The on-off ratio increased, the subthreshold was higher and hysteresis was reduced. I will focus on the same samples in the following, in order to investigate how the electrical and optical properties are affected by the Al_2O_3 coating. The photoluminescence measurements were performed by me. The THz measurements on the MBE-grown InAs nanowires were performed by Dr. Jessica L. Boland and have been added to show a comprehensive picture of this special passivation technique.

For the THz measurements the nanowires were transferred onto a quartz disc to enable THz transmission [129]. Samples were excited by a 35 fs laser amplifier with a centre wavelength of 800 nm. Fluences were varied from $7\,\mu J\,cm^{-2}$ to $68\,\mu J\,cm^{-2}$.

Sample description	Surf. lifetime (ps)	Vol. lifetime (ps)
Pass. - small diam. (105 nm)	65	1008
Pass. - medium diam. (123 nm)	160	885
Pass. - thick diam. (138 nm)	—	420
Unpass. - small diam. (102 nm)	92	421
Unpass. - medium diam. (110 nm)	116	490
Unpass. - thick diam. (137 nm)	201	646

Table 7.1: Overview of surface and volume lifetimes of passivated and unpassivated MBE-grown InAs nanowires with different diameters.

All measurements were performed at room temperature under vacuum. More information can be found in Section 3.1.

InAs nanowires are known to have a high surface recombination velocity and are therefore very surface sensitive [125]. This was also confirmed by the photoconductivity decays of the passivated and unpassivated InAs nanowire samples. Furthermore, it was observed that the passivation layer did not improve the electrical and optical properties of the InAs nanowires as assumed. Instead, the results from the THz measurements, which are discussed in more detail in the following, were inconclusive.

The photoconductivity lifetimes, which include non-radiative and radiative recombination, show a biexponential decay in both passivated and unpassivated InAs nanowires. The fast decay within the first 50 to 200 ps probably occurs due to surface states. 150 ps after excitation, unpassivated nanowires can be fitted monoexponentially. These fits are attributed to the bulk material of the nanowire. Therefore, the rate constants of the two photoconductivity decays extracted from each sample are referred to as the surface lifetime and the volume lifetime. The volume lifetimes are determined to be 421 ps, 490 ps, and 646 ps for the samples with thin (102 nm), medium (110 nm), and thick (137 nm) diameter. After passivation, volume lifetimes change to 1080 ps, 885 ps, and 420 ps. A summary of the surface and volume lifetimes can be found in Table 7.1. The passivation does not improve the lifetime for every passivated sample. This inconsistency is also shown in Figure 7.1. Al_2O_3 passivation has quite a different effect on each sample. It deteriorates the performance of the thick nanowires but improves performance for the sample

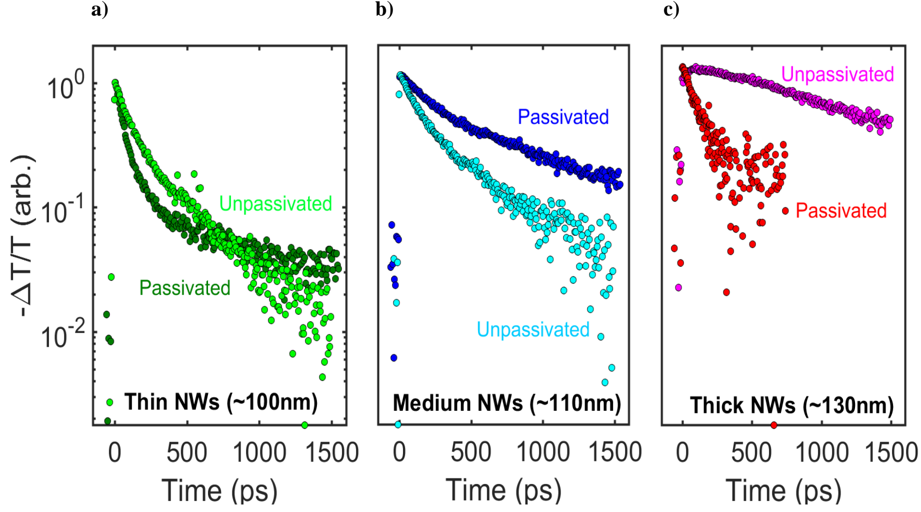

Figure 7.1: Comparison of the lifetimes of passivated and unpassivated InAs nanowires with diameters of (a) 105 nm and 102 nm, (b) 123 nm and 110 nm, and (c) 138 nm and 137 nm, respectively. The samples were excited with 2.0 W/cm^2 power density. The intensity is normed. Passivation has a different effect on each sample. Graph was made by Dr. Jessica Boland.

with medium diameter. In case of the thin diameter samples, the passivated nanowires have a faster decay than the unpassivated nanowires until 700 ps after photoexcitation. Afterwards, the decay of the passivated sample is slower than for the unpassivated one. Overall, passivation does not straight forwardly improve or degrade the electrical properties of the wires.

Furthermore, photoluminescence spectroscopy was performed on the same samples, but with the nanowires free standing on the GaAs substrate. The samples were cooled down to 4 K in a cold finger cryostat and continuously excited with a 532 nm laser at a power density varied between 5.2 and 0.7 Wcm^{-2}. The emitted signal was measured with a Fourier transform infrared spectrometer using a KBr beamsplitter. The InSb detector was connected to a lock-in amplifier referenced to the excitation laser, which was chopped at 3331 Hz, to reduce the noise. Further details about the measurement and calibration can be found in Chapter 4.

From each of the passivated and unpassivated InAs nanowire samples a series of measurements at different excitation fluences were taken. The first scan was

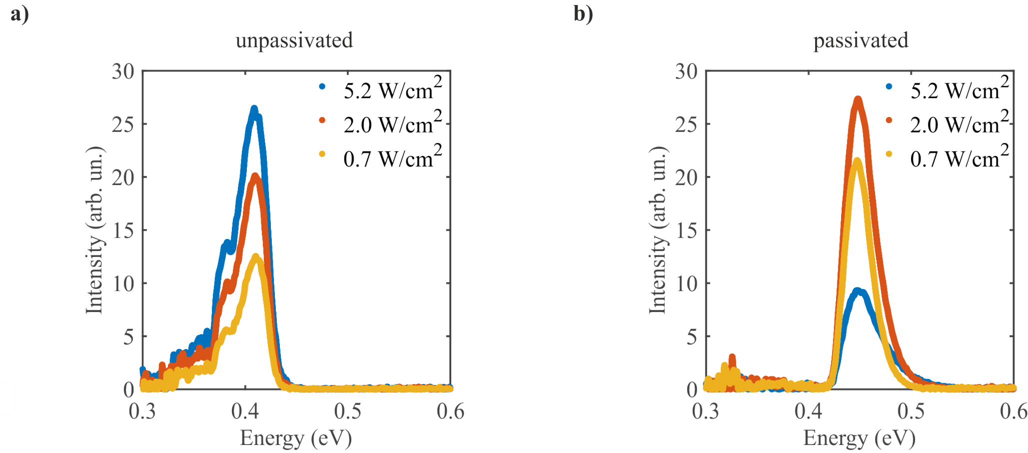

Figure 7.2: Fluence (5.2 W/cm^2, 2.0 W/cm^2, 0.7 W/cm^2) dependent spectra of (a) unpassivated and (b) passivated InAs nanowires with a diameter of 138 nm and 137 nm. The passivated sample is degrading faster than the unpassivated one.

performed at the lowest excitation power density of 0.7 Wcm^{-2}, before being increased to 2.0 Wcm^{-2} and then to 5.2 Wcm^{-2}. In Figure 7.2 the fluence-dependent spectra of the (a) unpassivated and (b) passivated InAs sample with thick diameter are shown. The passivated sample show a strong photo-induced degradation for higher fluences because the PL intensity decreases with rising fluence. The same degradation trend is shown by the passivated sample with medium diameter, but not by the passivated sample with small diameter, and the unpassivated nanowire samples. Furthermore, all passivated samples show a 4 to 6 meV shift to higher energies of the maximum peak with increasing power, while for the unpassivated samples, the peaks shift by 3 to 5 meV to lower energies.

The PL spectra of the three passivated InAs samples with different diameters are directly compared to their unpassivated ones in Figure 7.3. The unpassivated samples emit around 0.41 eV ($\lambda = 3.0\,\mu$m). This value agrees with literature values for zincblende InAs nanowires [195, 215]. Passivated samples emit at a higher energy of around 0.45 eV ($\lambda = 2.8\,\mu$m). It is quite unlikely that the shift is caused by quantum confinement, because the nanowire diameters are larger than the InAs Bohr radius of 40 nm [200]. Koblmüller *et al.* have shown that the diameter of zincblende InAs nanowires needs to be smaller than 100 nm to observe a confinement

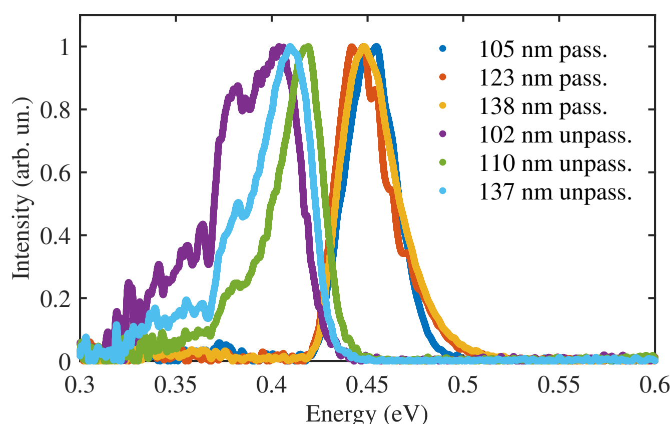

Figure 7.3: Normalised PL spectra for passivated and unpassivated InAs nanowires with varying diameters. The passivation shifts the PL energy peak from 0.41 eV to around 0.45 eV.

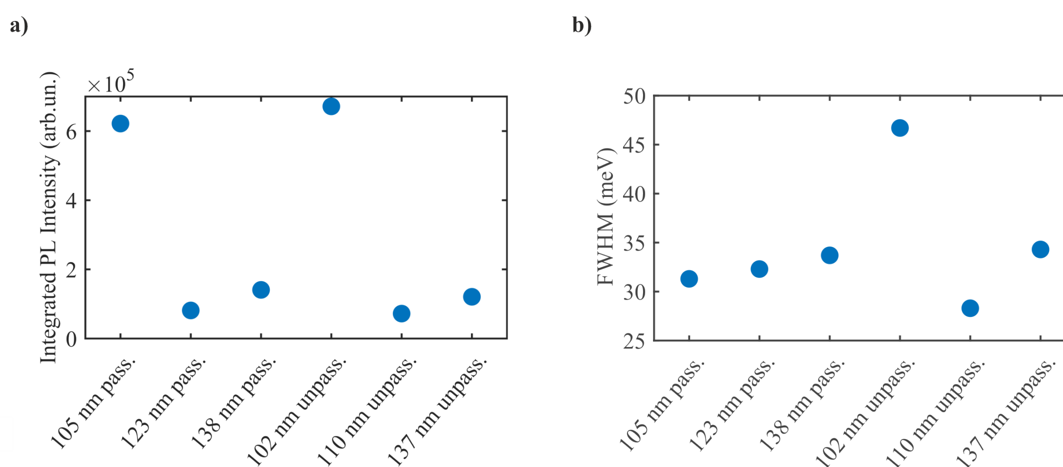

Figure 7.4: (a) Integrated PL intensity and (b) FWHM of passivated and unpassivated InAs nanowires with diameters varying from 102 nm to 138 nm. (a) indicates, that the PL intensity depends on nanowire growth, not passivation. (b) shows a smaller distribution of FWHM for samples with passivation.

effect [215]. A likely explanation for the shift in band gap is strain induced by the Al_2O_3 passivation layer or the arsenic capping layer [201].

In general, passivation is supposed to increase PL efficiency by decreasing the non-radiative decay at the surface and preventing band bending. Thereby, the FWHM decreases and the PL intensity increases. However, the integrated PL intensity for our samples seems to be independent of passivation. Passivated and unpassivated InAs samples with the same diameter give similarly strong signals, as can be seen in Figure 7.4a. The samples with the small diameters have a six

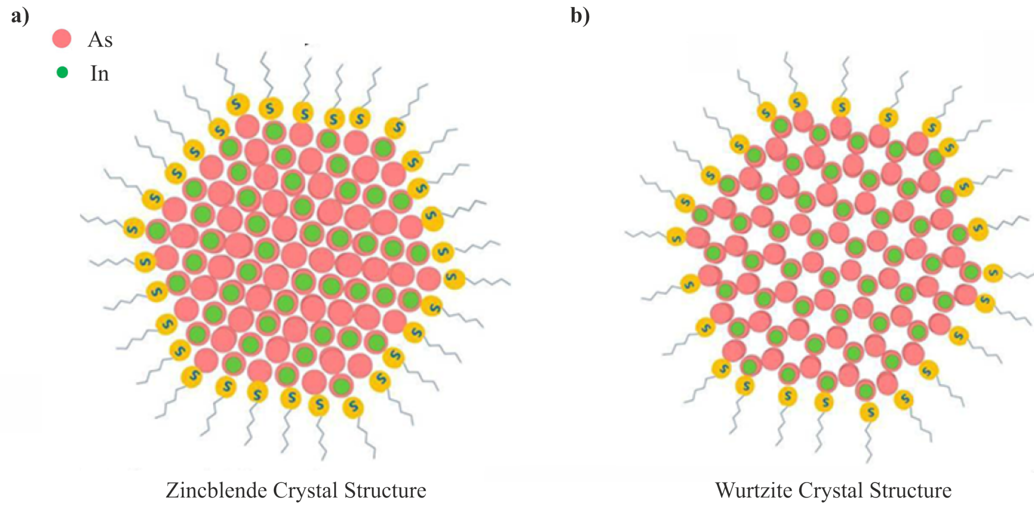

Figure 7.5: Schematic diagram of the cross-section of InAs nanowire with (a) zincblende and (b) wurtzite crystal structure. The stacking density of both atoms are different for the two crystal structures, therefore a different amount of organic sulphide octadecylthiol (yellow dots), which is meant to passivate the wire, can attach to the surface. Adapted from Ref. [207].

times higher PL intensity than the others. This could have been caused by either a less defective crystal structure or a higher nanowire density for these smaller diameters. The Al_2O_3 passivation layer had an effect on the width of the PL signal (Figure 7.4b. The FWHM of the unpassivated samples vary significantly between 28 and 47 meV, while the passivated samples have a smaller distribution of FWHM at around 31 to 34 meV.

In summary, it has been shown that Al_2O_3 passivation of InAs nanowires did not improve the performance of the samples as expected. Strain in the passivated samples shifted the bandgap from 0.41 to 0.45 eV. The coating reduced the distribution of the FWHM but had no help on the PL intensity. Furthermore, the lifetimes extracted by OPTP spectroscopy were inconclusive.

7.2.2 Passivation dependence on crystal structure and sample geometry of MOVPE-grown InAs Nanowires

Because the Al_2O_3 shell used in the former section did not passivate the nanowire surface well, a slightly altered recipe was instead applied for the ALD-deposited Al_2O_3 shell of InAs nanowires, which were grown via MOVPE by Dr. Hannah

Joyce (University of Cambridge). The effect of nanowire diameter and crystal structure on the electrical and optical properties of InAs nanowires and on the effectiveness of passivation were investigated.

Each crystal structure has a different band structure and ratio of surface atoms. InAs usually grows in zincblende structure, but in nanowire it can also be grown in wurtzite. A cross-section of both structures is shown in Figure 7.5. The ratio of In and As atoms at the surface varies with the crystal structure and thus influences the surface dependent properties. It also plays an important role for the effect of passivation. Depending on the passivation method, either In or As has a stronger bond with the passivation layer [207]. This affects the quality of passivation considerably. Additionally, InAs zincblende and wurtzite have different bandgaps of 0.41 eV and 0.48 eV, respectively [38, 51, 215, 216]. For a high photoluminescence efficiency wurtzite needs to be excited with photons having an energy larger than the bandgap, and polarised perpendicular to the nanowire axis, whereas the zincblende crystal structure is polarisation-independent [195]. Also the nanowire diameter affects the optical properties. If the diameter is reduced, the polarisation dependence becomes more prominent and the bandgap shifts to higher energies due to quantum confinement [215]. Because diameter, crystal structure, and passivation are all essential for the electrical and optical properties of InAs nanowires, many papers have been published about these topics. But to my best knowledge, a comprehensive study looking into the effects of these three nanowire parameters at the same time with both electrical and optical measurements has not been done before.

7.2.2.1 Growth

The InAs nanowires discussed in the following section were grown on an InAs(111)B wafer by Dr. Hannah Joyce (University of Cambridge) via a chemical process, not a physical one like the wires discussed in Section 7.2.1. The substrate was treated with a poly-L-lysine solution. This functionalisation enabled the deposition of gold droplets acting as catalysts. The substrate was loaded into an AIXTRON 200/4 horizontal flow MOVPE reactor at the Australian National University and annealed

at 600 °C under arsenide (AsH_3) atmosphere. Afterwards the nanowires were grown using AsH_3 and trimethylindium (TMI) as precursors. The growth parameters were adjusted to achieve pure-phase crystal structures [217].

The set of nanowires consists of ten different InAs nanowire samples: pure-phase wurtzite structure with a diameter of 20 nm, 30 nm, 40 nm, 50 nm, 60 nm, 80 nm, and pure-phase zincblende structure with 20 nm, 30 nm, 50 nm and 80 nm. One piece of each sample was taken and passivated with a 90 nm thick Al_2O_3 shell. The shell was deposited with a Cambridge NanoTech ALD system. TMA and H_2O were used as precursors. To distinguish between the InAs substrate and the InAs nanowires, the wires were transferred onto z-cut quartz discs for both PL and THz measurements. Most of the quartz discs were covered by a thin parylene layer to increase adhesion [127].

7.2.2.2 Experiments and Results

The effect of crystal structure, NW diameter, and passivation on nanowires were systematically studied. The experimental methods and obtained results will be discussed in the following.

Influence of the substrate on PL spectroscopy

Photoluminescence spectroscopy was performed on the samples described above. A 532 nm laser (power density of 6.6, 3.0 or 1.1 Wcm^{-2} at the sample position) excited the samples, which were cooled to 4.2 K in a cold finger cryostat. A Fourier transform infrared spectrometer was used as detector. A lock-in amplifier referenced to a chopper, driven at 3038 Hz, was used to reduce thermal noise. Further details to the experimental setup and calibration are discussed in Chapter 4.

When executing the first PL measurements, I saw that not only were the nanowires transferred onto the quartz disc, but also tiny pieces of InAs substrate, which cannot be distinguished from nanowires by eye. This transfer method was used for many different nanowire types and substrates and has not been reported before. However, these InAs wafers seem to be very brittle, independently of the force used to rub the wires onto the disc. Moving along the substrate for measurements, the

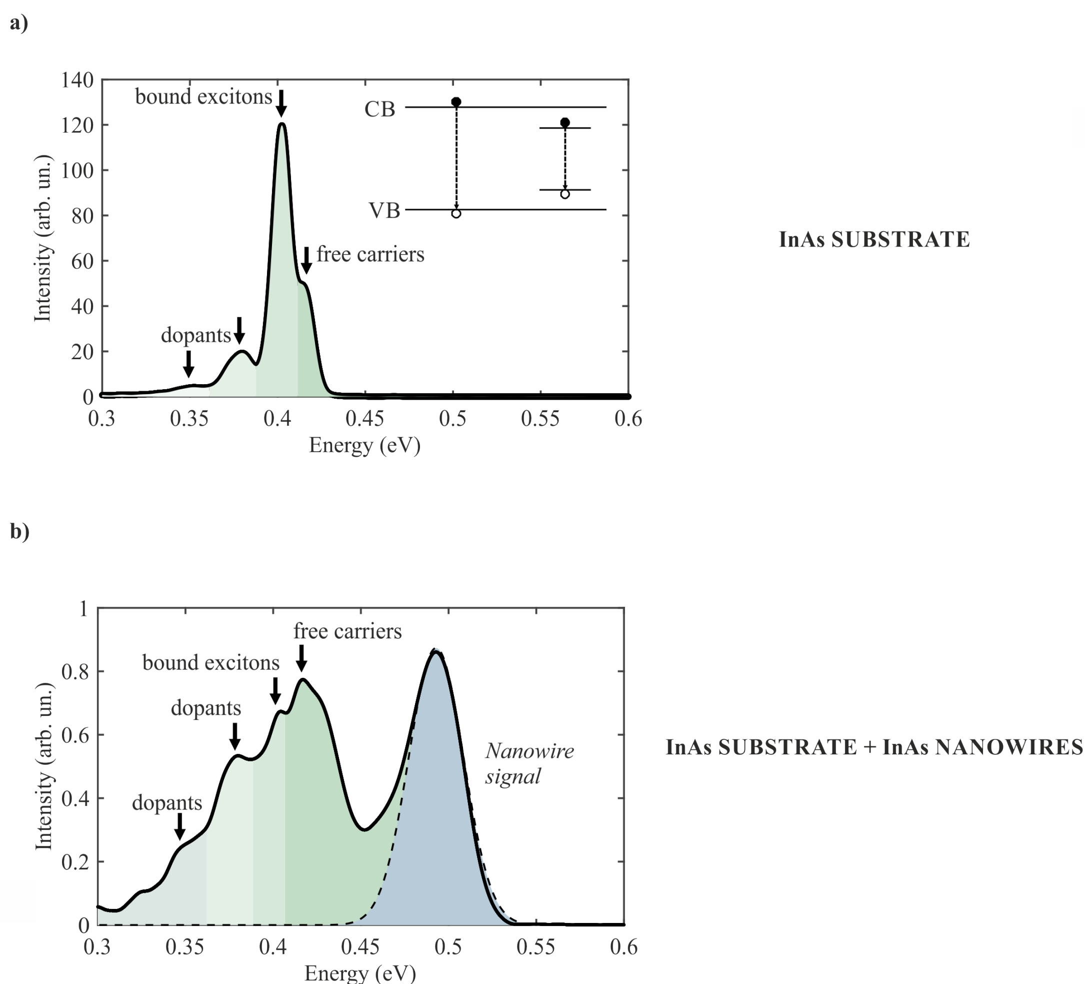

Figure 7.6: (a) Spectrum of the InAs growth substrate for InAs nanowires at power density 3.0 $\mathrm{Wcm^{-2}}$. The multiple peaks can be assigned to free charge-carriers, bound excitons, and dopants. The different recombination mechanisms are colour-coded. The different transitions are depicted in the top right inset. (b) Spectrum of passivated InAs pure-phase WZ nanowires with 50 nm diameter (grey). The dotted line shows the Gaussian fit of the nanowire signal. InAs substrate pieces have been accidentally transferred with the nanowires. Their contribution to the spectrum has been assigned and colour-coded like in (a).

ratio of signal from substrate and wires varied. Therefore, the spectra show many different peaks and each of them is assigned to either nanowire or the InAs substrate.

In order to distinguish between the peaks originating from the nanowires and the growth substrate, PL spectroscopy was performed on the InAs substrate. This spectrum at a power density of 3.0 $\mathrm{Wcm^{-2}}$ is shown in Figure 7.6a. There are four peaks due to different recombination mechanisms, which are also depicted in the schematic diagram inset and discussed in Section 2.2. The peak position and

origin were compared and verified with Tang's paper on InAs photoluminescence [218]. The shoulder at 0.415 eV ($\lambda = 2.99\,\mu$m) is caused by free charge-carriers — electrons and holes which were created by the incoming laser power. The maximum peak at 0.403 eV ($\lambda = 3.08\,\mu$m) is very close to this shoulder and is caused by excitons — a quasiparticle of an electron and hole bound together. They are bound together by the Coulomb interaction and therefore, their energy is slightly below the recombination energy of free charge-carriers [219]. Besides, there are two low energy peaks at 0.352 eV and 0.380 eV. They are caused by recombination via impurity levels. This means that there are impurities or defects in the InAs material below the bandgap which may originate from doping. The charge-carriers, created by the laser pulse, can get trapped in the sub-bandgap states and then recombine radiatively. The intensity and ratio of different peaks emitted from the substrate alters with the position on the sample. For a lot of nanowire samples, the 0.38 eV ($\lambda = 3.26\,\mu$m) peak originating from the InAs substrate pieces is the most dominant peak. This suggests that the doping is not homogeneous through the whole wafer and eventually more concentrated on the surface of the growth substrate.

Identifying all peaks associated with the substrate enables one to distinguish between the signal from wafer pieces and the one from the nanowire samples. As an example, a spectrum of InAs nanowires — pure-phase wurtzite, passivated, 50 nm diameter - is shown in Figure 7.6b. The power density was 3.0 Wcm^{-2}. The nanowire peak at 0.475 eV ($\lambda = 2.610\,\mu$m) is fitted with a Gaussian (dotted line) and shaded in grey. Because the crystal phase is wurtzite, the nanowire peak can be clearly distinguished from the wafer signal and each single peak was assigned and colour-coded the same way as in Figure 7.6a. The peak intensity for free charge-carriers in the InAs wafer here is higher than the intensity for bound excitons.

This is further discussed in Figure 7.7. The ratio of the different InAs substrate's peaks changes drastically for different power densities. At 1.1 Wcm^{-2} recombination of free excitons is dominant and radiative recombination of dopants and free charge-carriers is only evident as a shoulder. The PL intensity increases for higher excitation powers. However, the peak intensity associated with free charge-carriers rises much

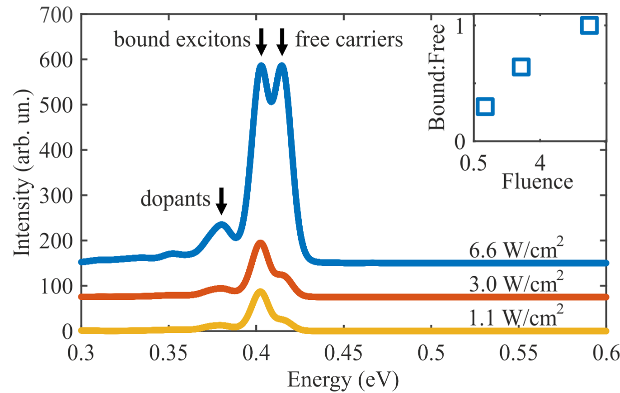

Figure 7.7: Laser fluence-dependent spectra show the Mott transition for InAs wafer. All peaks are assigned to dopants, bound excitons and free charge-carriers. With increasing fluence the intensity of the free charge-carriers rise faster than the intensity of the bound excitons. The ratio of bound excitons to free charge-carriers can be seen in the inset top right. The different spectra are shown with an offset.

faster than the one associated with bound excitons. The ratio of these two intensities increases steeply from 0.29 to 1 for 1.1 $\mathrm{Wcm^{-2}}$ and 6.6 $\mathrm{Wcm^{-2}}$, respectively (see insert Figure 7.7). This effect can be explained by the Mott transition [73, 220, 221]. Photons from the 532 nm laser give their energy to the semiconductor and enable the electron to be excited from the valence to conduction band creating an electron-hole pair. Because the laser energy is higher than the bandgap, the electron in the valence band releases energy by non-radiative processes, such as phonon relaxation, until it reaches the lower limit of the valence band. Electrons and holes are attracted to each other due to Coulomb force and one electron and one hole build an exciton, the binding energy of which is below the bandgap. For higher excitation powers above the Mott transition, the number of charge-carriers increases, resulting in a decrease of Coulomb force between the charge-carriers due to the screening effect. Therefore, fewer excitons are generated and the number of free charge-carrier rises faster than excitons [75, 222, 223].

Analysis of photoluminescence spectra

After the discussion on the photoluminescence from the substrate and the analysis of the multiple peaks, I will now focus on discussing the signal emitted by the nanowires. In Figure 7.8 a selection of spectra is given as an overview. The spectra are divided according to their crystal structure and passivation: (a) zincblende and passivated,

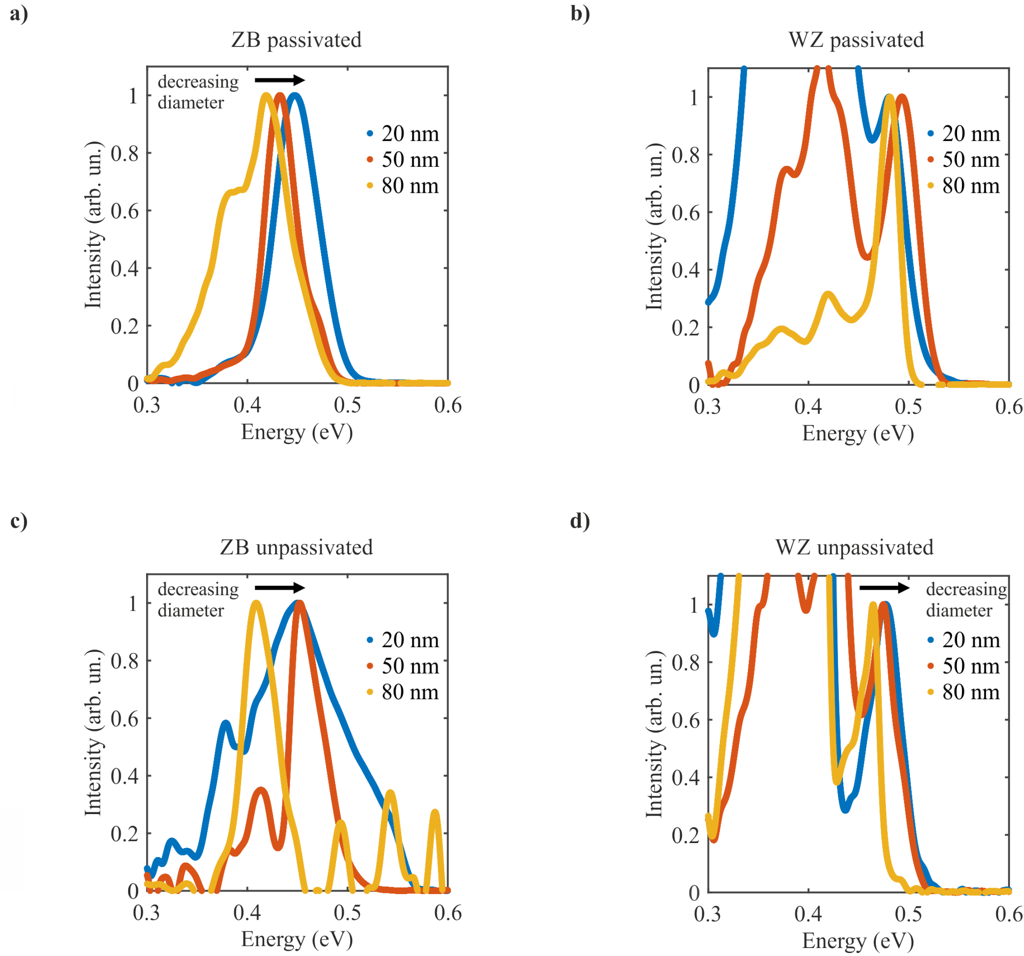

Figure 7.8: Spectra of InAs nanowires with 20 nm, 50 nm, and 80 nm diameter, which are (a) pure-phase zincblende and passivated, (b) pure-phase wurtzite and passivated, (c) pure-phase zincblende and unpassivated, (d) pure-phase wurtzite and unpassivated. In (a), (c) and (d) quantum confinement causes a shift to higher energies with decreasing diameter. Each spectrum was normalised to the nanowire peak and taken at a power density of 3.0 Wcm^{-2}.

(b) wurtzite and passivated, (c) zincblende and unpassivated, (d) wurtzite and unpassivated. In each graph a PL spectrum, which was normalised to the intensity of the nanowire peak, is given for the diameter of 20 nm, 50 nm and 80 nm. There is a difference of roughly 50 meV between the different types of crystal structure. Furthermore, the spectra shift to higher energies with decreasing diameter. This could be attributed to quantum confinement, because diameters of 80 nm or smaller are of the same magnitude as the 40 nm InAs Bohr radius. However, this diameter-dependent shift cannot be observed for pure-phase, wurtzite passivated nanowires.

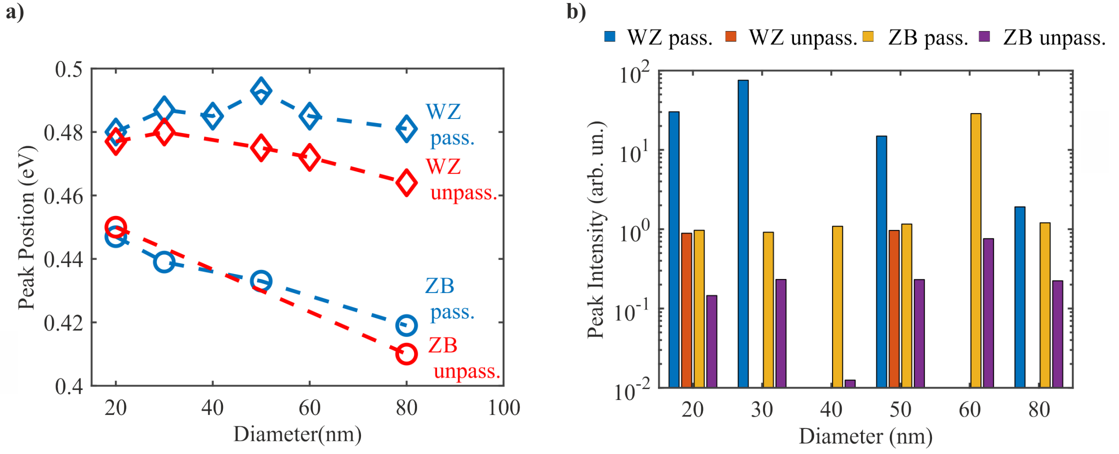

Figure 7.9: Diameter-dependent (a) peak position and (b) peak intensity for different types of InAs nanowires (passivated, unpassivated, pure-phase zincblende, and pure-phase wurtzite crystal structure) at 3.0 Wcm^{-2}.

A closer look at the behaviour of peak position and intensity is taken in Figure 7.9.

Figure 7.9a shows the PL peak energy in relation to the nanowire diameter. Each set of nanowires is colour-coded: blue for passivation, red for no passivation, diamonds for wurtzite and circles for zincblende. The nanowires with zincblende crystal structure, both passivated and unpassivated, show a strong quantum confinement of 40 meV for a diameter change from 80 to 20 nm. This values fit quite well with the theoretical calculated bandgaps for InAs nanowires with different diameters from Koblmüller *et al.* [215]. The nanowires with wurtzite structure and no passivation also show a diameter dependence for the peak position, but the difference is only 13 meV. Therefore, it seems that the quantum confinement effect is less strong for wurtzite than for zincblende structure.

Furthermore, Figure 7.9a shows that the passivated wurtzite InAs nanowires do not follow the same trend as the unpassivated wires and zincblende passivated NWs. Their bandgap seems to be fixed to 0.48 eV ($\lambda = 2.58\,\mu$m). For a nanowire diameter of 20 nm, peak energies of unpassivated wurtzite nanowires are at 0.477 eV ($\lambda = 2.60\,\mu$m) and if passivated at 0.480 eV ($\lambda = 2.583\,\mu$m). At 80 nm diameter, there is 17 meV difference between the unpassivated and passivated peak positions. The effects of passivation on different crystal structures can arise from the altered

ratio of In to As atoms on the surface, because these atoms' bonds with Al_2O_3 differ from one another [207].

Two of the main advantages of passivation are improving the collected photocurrent in InAs nanowire detectors and obtaining a high electroluminescence yield in InAs nanowire LEDs at room temperature. However, this is hard to measure quantitatively with the current PL setup because it is an ensemble measurement and the density on the quartz sample is not homogeneous. Therefore, an overall trend in PL intensity is demonstrated. Figure 7.9b is a bar plot giving the peak intensity for wurtzite, zincblende, passivated and unpassivated InAs nanowires and comparing different diameters. In general, passivated samples have a higher intensity than unpassivated samples with the same structure, the signal of which was sometimes even not detectable. Furthermore, there seems to be a trend of wurtzite samples emitting higher PL intensity than zincblende. PL scans on single nanowires would be preferable to further investigate these samples.

For a better understanding of the processes which take place within the InAs nanowires, a closer investigation of the fluence dependence of the nanowire PL is needed. Figure 7.10 gives an overview of the (a) peak PL energy and (b) peak intensity. Wires with wurtzite structures are depicted as diamonds, and zincblende as circles, and each single sample has a different colour. Most samples show a shift of a few meV towards higher photon energies. This is expected due to the Burstein-Moss effect, which is described in Section 2.2.2. A larger excitation power creates a higher population density for valence and conduction band. The charge-carriers have higher energy states and therefore, photons with higher energies are created during radiative recombination [224]. Two samples (unpassivated InAs nanowires with wurtzite crystal structure of 50 nm diameter, and unpassivated wires with zincblende crystal structure of 20 nm diameter) show a shift of less than 9 meV to lower energies with higher excitation energies. One reason for that could be lattice heating due to the excitation power. Another one could be a lower signal intensity and increased noise, making it harder to determine the peak position of the emitted signal.

a)

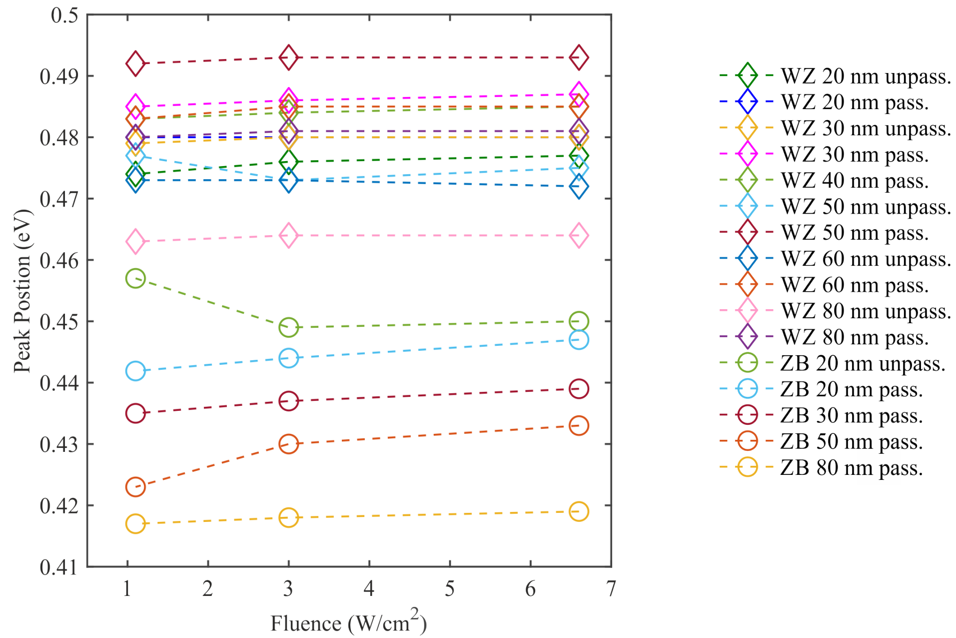

b)

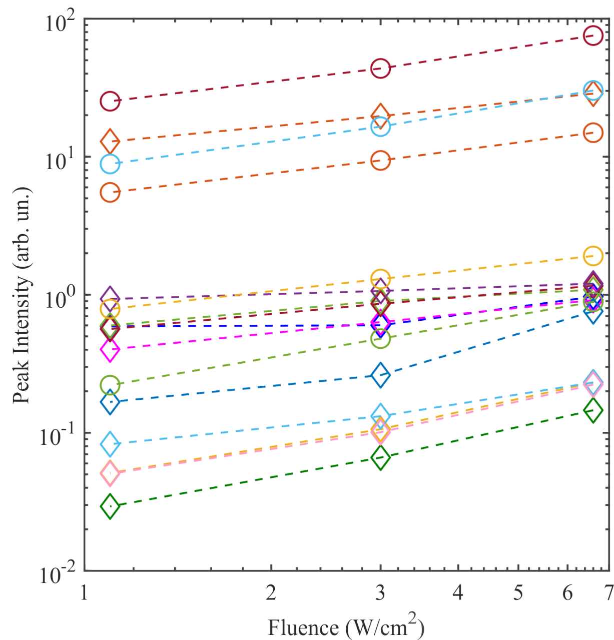

Figure 7.10: Fluence dependence of (a) peak position and (b) peak intensity for different diameters, passivated, unpassivated, pure-phase zincblende, and pure-phase wurtzite InAs nanowires.

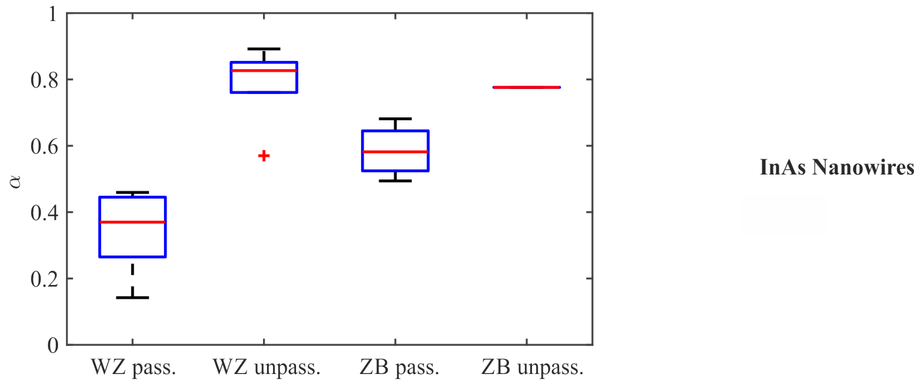

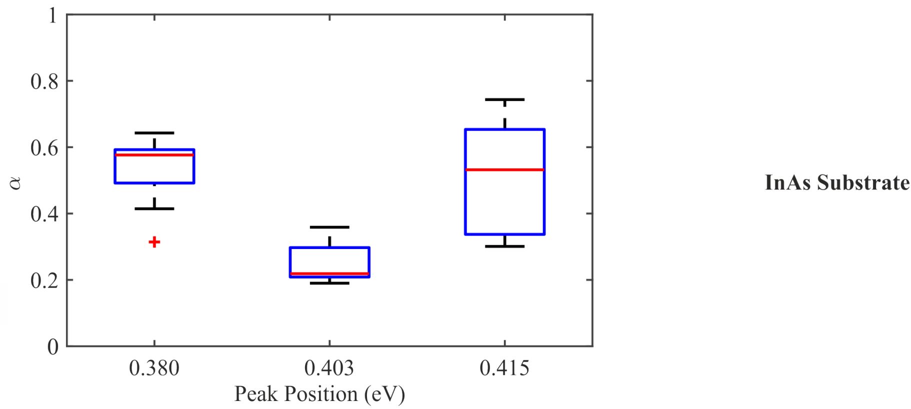

Figure 7.11: The boxplot shows different values of α for (a) InAs nanowires and (b) InAs substrate. The red line in each box marks the median value and the box extends to the 25% and 75% percentiles. The whiskers indicate the point which is furthest away and not an outlier (+).

The peak intensities for the different samples vary by four orders of magnitude. Therefore, Figure 7.10b shows the fluence-dependent intensity on a double logarithmic scale. Photoluminescence intensity I usually follows a power law dependence,

$$I = BF^{\alpha}, \tag{7.1}$$

where F represents the excitation power, B a multiplication factor and α is the exponent determining the type of recombination. Usually $\alpha = 1$ indicates excitonic emission and $\alpha = 2$ bimolecular recombination [225].

Figure 7.10b shows that not every sample follows this equation. An overview of the different α values is given in 7.11. In (a) the exponents are divided in

different categories of nanowire samples: wurtzite structure — passivated, wurtzite structure — unpassivated, zincblende structure — passivated, zincblende structure — unpassivated. For comparison, α is also given for the InAs substrate pieces which were transferred onto the quartz disc together with the wires (Figure 7.11b. The different substrate peaks are distinguished because each of them develop differently with fluence. This abundance of information is shown as a box plot for a better understanding. The median α is depicted as a red line and the box includes 25% to 75% percentiles. The whiskers include all other values except the outlier, which is indicated by a red cross. An outlier is a value for α which is more than 1.5 times the box height away from either the bottom or top end of the box. Every value for α in any category is below 1, indicating a reduction in efficiency converting incoming laser photons into emission of photoluminescence. Furthermore, the median values for unpassivated nanowire samples are higher than for passivated. But this effect is less dominant for zincblende than for wurtzite, where it drops from 0.83 to 0.37.

For the InAs substrate the power law also shows sub-linear behaviour. The values for the peak at 0.415 eV are quite widespread due to their fluence dependence. As show in Figure 7.7, the free carrier density grows faster than the bound exciton density once a threshold is exceeded. The disparity in values for the different peaks are related to their corresponding different recombination mechanisms.

The sub-linear behaviour, which is observed for each NW sample and each peak of the InAs substrate pieces, is caused by thermal heating of the sample. Peak broadening could be another reason. In that case, the energy distribution of the emitted photons broadens and the increase in emitted photons with excitation power cannot be directly correlated with peak intensity.

Analysis of photoconductivity decays taken with OPTP spectroscopy To gain knowledge about the time-dependent behaviour of InAs nanowires with different crystal structures, diameter and passivation, THz spectroscopy measurements were performed on the same non-degraded NW samples that were studied using PL spectroscopy. The photoconductivity decays were obtained by exciting the samples

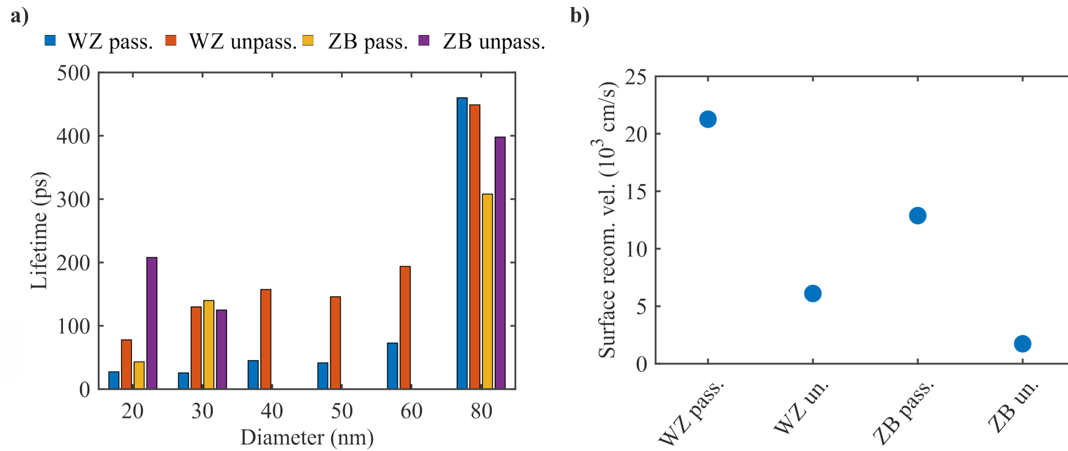

Figure 7.12: (a) Lifetimes and (b) surface recombination velocities for four different groups of MOVPE-grown InAs NWs (WZ and passivated, WZ and unpassivated, ZB and passivated, ZB and unpassivated). The data were taken by OPTP spectroscopy.

with a 35 fs pulse at 800 nm centre wavelength and a fluence between 7 μJ cm^{-2} and 398 μJ cm^{-2}. More information about the OPTP setup can be found in Chapter 3.

The lifetimes were extracted from the photoconductivity decays, of which an example is shown in Figure 3.5, by a monoexponential fit of the photoconductivity decay measurement. A comparison of all InAs NW samples with different diameters (20 nm-80 nm), crystal structures (WZ or ZB), and passivation (Al_2O_3 or none) is given in Figure 7.12a. The substrate pieces have a much longer photoconductivity lifetime than the InAs nanowires [226]. Therefore, their contribution can be neglected.

The photoconductivity lifetimes increase with larger nanowire diameters due to the lower surface-to-volume ratio, which is discussed in detail in Section 3.1.3. Furthermore, the lifetimes of the unpassivated samples are generally longer than their passivated counterparts. When nanowires are generally successfully passivated, the lifetime usually increases because the nanowire surface is protected from dangling bonds, uncontrolled oxidation, and defects. Instead for these InAs nanowires, the passivated samples have significantly shorter lifetimes than the unpassivated samples. This correlation originates from the band bending of InAs materials which was discussed in Section 7.1. For the unpassivated InAs nanowires, the energy bands at the surface are pinned above the Fermi level by traps incorporated into the material,

thus an n-doped accumulation layer is created. The band bending decreases with higher charge-carrier density due to screening effects [86], or with a passivation layer. Therefore, the accumulation layer increases the lifetime of the unpassivated nanowires [227]. The band bending also affects the surface recombination velocities.

The measured surface recombination velocities (Figure 7.12b), which are defined in Section 3.1.3, increase if a passivation layer is added. Passivated nanowires with a wurtzite or zincblende crystal phase have surface recombination velocities of 2.1×10^4 cm/s and 1.3×10^4 cm/s, respectively, which are a magnitude higher than for unpassivated WZ and ZB samples (6.1×10^3 cm/s and 1.7×10^3 cm/s). The accumulation layer of the unpassivated sample prevents the interaction of charge-carriers and surface, while the flat energy bands of the passivated samples do not, thus more processes can happen on the surface. The disparity of α values (see Figure 7.11a for passivated and unpassivated InAs nanowires is also caused by the band bending effect.

Summary

Passivation results in significant improvement in the optical properties. It increases the PL intensity and shifts the bandgap of wurtzite nanowires to higher energies. The latter effect is stronger for nanowires with larger diameters, whereas the bandgaps of zincblende NWs are not influenced. The shift highlights the effects of passivation on different crystal structures due to a changed ratio of In and As atoms at the surface. The other differences between zincblende and wurtzite are discussed on the basis of peak position, peak intensity, and fluence dependence.

The positive effect of the passivation of these samples on electric properties has already been shown by Alexander-Webber *et al.* [203]. They fabricated transistors from the same samples as used in this chapter. Passivation increased the charge-carrier mobility by almost an order of magnitude. However, OPTP spectroscopy has revealed that the photoconductivity lifetimes decrease and the surface recombination velocities increase for passivated samples compared to their unpassivated counterparts. This uncommon correlation is caused by the band

bending for unpassivated samples. The passivation prevents this change of the band structure. Therefore, Al_2O_3 passivation is detrimental for devices with long lifetimes.

7.2.3 Comparison of MBE- and MOVPE-grown InAs NW passivation

In this chapter two sets of InAs nanowires grown by different methods have been discussed. They were grown with diverse methods (MBE, MOVPE) on Si and InAs substrates, respectively. They were passivated with ALD-deposited Al_2O_3 with the same precursors, but the recipes were a little different. The MBE-grown nanowires had an arsenic capping which was removed before Al_2O_3 growth, and was purged with N_2 before passivation. The passivation shell was 10 nm thick. In contrast, the MOVPE-grown samples had a 90 nm Al_2O_3 shell and no pretreatment before ALD deposition.

The effect of passivation on the two sets of InAs nanowires were not consistent. The thick passivation layer for the MOVPE-grown InAs samples significantly improved the optical properties and prevented band bending. The MBE-grown nanowires, however, showed complex behaviours. The PL efficiency was independent of passivation. Furthermore, passivation had inconclusive effects on lifetimes and did not neutralise surface defects.

It is not yet clear whether the different performance of Al_2O_3 passivation at the MBE and MOVPE-grown InAs nanowires is due to the thickness of the Al_2O_3 layer, the pretreatment, the growth, or something else.

7.3 InAsSb compositions

As already mentioned earlier, InAs materials have excellent properties, such as narrow bandgaps, high spin-orbit coupling and large g-factors. Sb incorporation with InAs is of increasing interest because $InAs_{1-x}Sb_x$ maintains many superior properties of InAs (e.g. high mobility), while being able to alter its bandgap. This combination of materials enables tuning of the absorption and emission from 0.35 eV for InAs to 0.1 eV for $InAs_{0.35}Sb_{0.65}$. This is the lowest bandgap achievable with

group III-V semiconductors. Furthermore, the addition of Sb can decrease the defect density because Sb acts as a surfactant [62] due to covalent bonds which are longer than for other group III and V elements. Therefore, Sb tends to float on the top of the layer during growth without being incorporated [228], thus slowing down growth. As such, incorporation of Sb in growth helps control over crystal structure and polytypism of nanowires with even minute doping [68]. The improvements in crystal structure and device performance have been shown by many different groups [229, 230, 231]. Despite the benefits of the surfactant effect of Sb in the crystal structure of InAsSb nanowires, it has been proven difficult to grow this material with high Sb content. Potts *et al.* managed to grow InAsSb up to 35% Sb content [69] and their remarkable electronic properties have been shown in [88]. In the following, their optical properties including a bandgap change from 0.41 eV to 0.23 eV are shown.

7.3.1 Growth and crystal structure

$InAs_{1\text{-}x}Sb_x$ nanowires were grown vertically and self-catalysed on GaAs(111)B substrates via a DCAP600 MBE at a temperature of 520 °C by Dr. Heidi Potts in Professor Anna Fontcuberta i Morral's group at EPFL. To obtain a maximum yield with minimal distribution in nanowire geometry, the growth substrates were coated with a 4.5 nm thin layer of silicon oxide. The antimony flux was increased during growth with Sb concentrations of 0%, 11% 16%, and 35%. In the end, the nanowires are 4 μm long and have diameter of 70 nm, 79 nm, 74 nm, and 85 nm respectively. For increasing Sb content, a strong decrease in the defect density of the InAsSb nanowires is observed, with defect densities of 250 μm^{-1}, 50 μm^{-1} and less than 1 μm^{-1} extracted for InAsSb nanowires with 16%, 21% and 35% Sb content, respectively. Above 16% Sb content, the wurtzite phase is completely suppressed and nanowires with 35% Sb content were determined to be almost completely defect-free with only a few twin defects per micrometre [88].

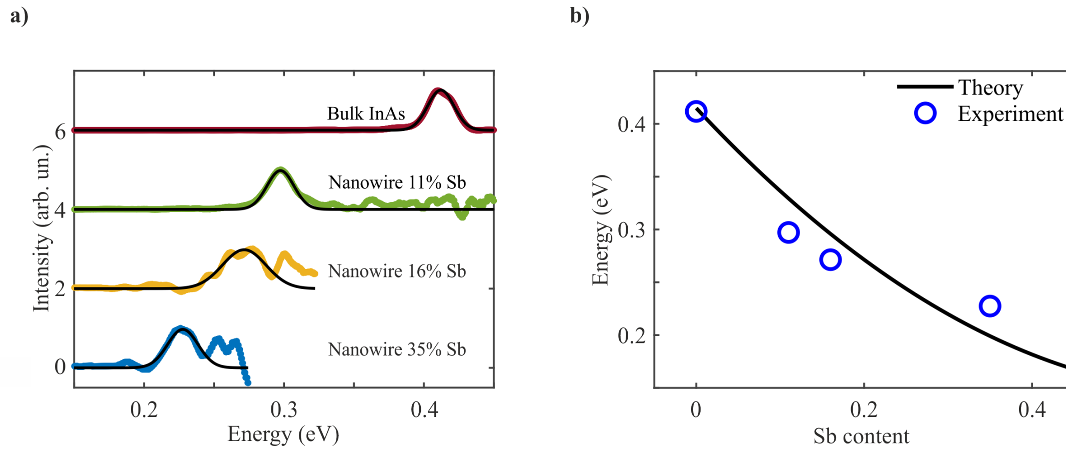

Figure 7.13: (a) Normalised spectra of InAsSb nanowires with different Sb contents and a y-axis offset. Each spectrum is fitted with a Gaussian (black line). (b) Antimony dependent theoretical bandgap (line) in comparison with experimentally determined bandgap (circles) for InAsSb nanowires.

7.3.2 Bandgap dependence on Sb content

The samples were measured with a cryogenic mid-infrared Fourier transform photoluminescence system. A 532 nm laser excited the samples, which were cooled to 6 K, at a power density of 200 mW cm^{-2}, which was reached by using multiple neutral density filters and a lens focusing onto the sample position. The signal was detected by a nitrogen-cooled cadmium telluride detector. To reduce noise, a lock-in amplifier is connected to the detector and a chopper which is driven at 3312 Hz. The measurements were performed on nanowires standing on the GaAs growth substrate.

The obtained spectra are shown in Figure 7.13a. Each spectrum was fitted with a Gaussian to extract the peak position. Each spectrum is normalised and added in the same Figure with a y-offset. The difference in signal intensity for the different samples can be seen due to the variations of noise. InAsSb nanowires with 11% Sb antimony content give a much higher, less noisy signal than the samples with 16% and 35% Sb. This could originate from a possible higher nanowire density, because from this sample I received a piece from the middle of the master sample.

A clear shift towards lower energies with increasing antimony content can be seen for the different spectra. The bandgap is extracted and compared with a theoretically calculated bandgap in Figure 7.13b. For determining the semiconductor

bandgap experimentally, each spectrum was fitted with a Gaussian. Finally, the thermal energy $E = \frac{1}{2}k_bT$ at 6 K was subtracted from the extracted peak position [207]. The theoretical change of bandgap E_{gap} for different antimony contents can be calculated via [232]

$$E_{\mathrm{gap}} = xE_{\mathrm{gap}}(\mathrm{InSb}) + (1 - \mathrm{x})\mathrm{E}_{\mathrm{gap}}(\mathrm{InAs}) - \mathrm{Cx}(1 - \mathrm{x}) \tag{7.2}$$

C represents the bowing factor, an empirical value describing the bandgap of ternary materials. x stands for the antimony content. $E_{\mathrm{gap}}(\mathrm{InSb})$ is the bandgap of InSb and $E_{\mathrm{gap}}(\mathrm{InAs})$ is bandgap of InAs at 6 K, the temperature T at which the measurements were done. The bandgaps of these materials were determined by

$$\begin{aligned} E_{\mathrm{gap}}(T) &= E_{\mathrm{gap}}(0\,\mathrm{K}) - \alpha \mathrm{T}^2/(\mathrm{T} + \beta) \\ E_{\mathrm{gap}}(\mathrm{InSb}) &= 235 - 0.27\mathrm{T}^2/(\mathrm{T} + 106)[\mathrm{meV}] \\ E_{\mathrm{gap}}(\mathrm{InAs}) &= 415 - 0.276\mathrm{T}^2/(\mathrm{T} + 83)[\mathrm{meV}]. \end{aligned} \tag{7.3}$$

The first equation of 7.3 calculates the bandgap depending on the temperature. $E_{\mathrm{gap}}(0\,\mathrm{K})$ is the bandgap at 0 K and α and β are two empirical parameters. The next two equations are specifically tailored for InAs and InSb. The values used for these calculations were measured by Fang *et al.* for bulk samples [233]. C was set to 0.662 eV. Farrel *et al.* [232] have determined this value for MOVPE-grown InAsSb nanowires with an antimony content of up to 15%. This value of C also coincides well with the established value for bulk InAsSb of 0.7 eV [234].

The peak position shifts from 0.41 eV for InAs to 0.23 eV for $InAs_{0.65}Sb_{0.35}$. Furthermore, there is a good agreement between the theoretical and the experimental values. The peak position of the InAs bulk of 0.41 eV sits on top of the theoretical curve. There are slight deviations of the measured bandgap for InAsSb nanowires from the theoretical determined bandgap. The difference can be attributed to bulk values used for calculations and polytypsm of the wires. Different crystal structures, like wurtzite and zincblende, are expected to have different bandgaps. Another reason could be a nonuniform distribution of antimony atoms in radial direction of the nanowires [69].

Nonetheless the deviations between experiment and theory are minimal. Due to that and their small bandgap, these nanowires are perfect candidates for bandgap engineering via antimony incorporation and for thermoelectric and thermophotovoltaic applications.

7.4 Summary

In summary, I explained the outstanding properties of InAs nanowires and their usage for electronic applications. However, for optoelectronic applications the efficiency of the emitted signal is too weak and surface defects favour non-radiative recombination. Different ways for passivation and their advantages and disadvantages were debated. This chapter discussed ALD-deposited Al_2O_3 deposition on InAs nanowires - grown with MOVPE and MBE. Both sets used the same materials but different recipes, ending up with very different results. The MBE-grown InAs nanowires had only a 10 nm thick shell, which was grown after the arsenic capping layer had been removed by annealing. This method appears not to increase photoluminescence efficiency, but to induce strain, and give inconclusive results for photoconductivity lifetime measurements. However, MOVPE-grown InAs nanowires with 90 nm thick Al_2O_3 shell and no treatment before ALD deposition show a clear improvement in photoluminescence efficiency.

Furthermore, the optical properties of MOVPE-grown InAs nanowires, their dependence on diameter and crystal structure and the effect of passivation on these parameters were investigated. The optical bandgaps for pure-phase wurtzite and pure-phase zincblende for diameters varying from 80 nm to 20 nm were investigated. The difference between the crystal structures was determined to be around 50 meV. Moreover, the spectra show a clear quantum confinement with decreasing diameter, because the diameter length is close to the Bohr radius. Each of the samples was also passivated. The shell had different effects on the different crystal structures due to the different amount of bonds formed between the shell and In and As atoms, respectively.

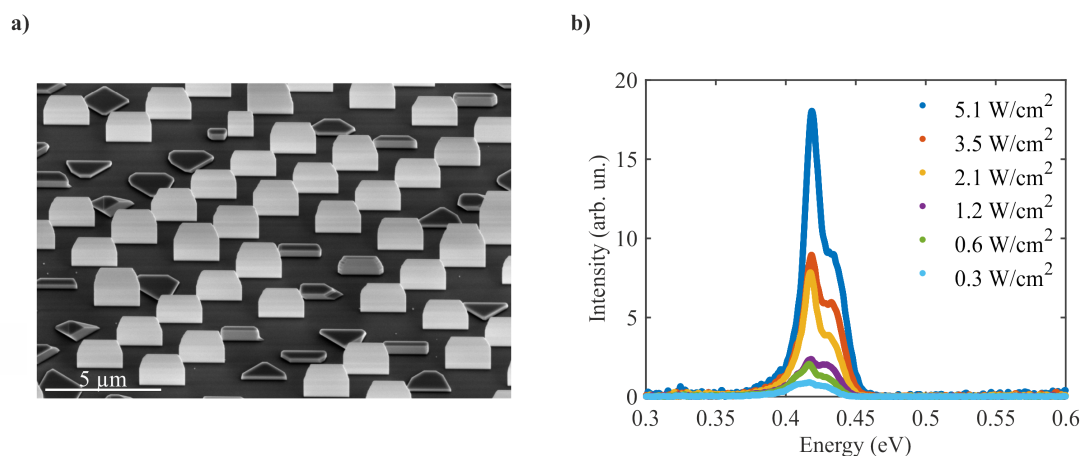

Figure 7.14: (a) SEM images and (b) fluence-dependent spectra of InAs nanomembranes. SEM was performed by Naiyin Wang.

Furthermore, a ternary material combination, which inherits the properties of InAs, but also enables better control of growth and bandgap engineering, was introduced. The bandgap changes from 0.41 eV to 0.23 eV for 0% and 35% antimony content, respectively, and is in good agreement with theoretical values. However, the quantum yield is quite low for InAsSb. It could be improved by Al_2O_3 passivation.

7.5 Outlook

There are different developments to utilise InAs nanowires for applications. The addition of Sb — as described above— is one of them. Another development changes the geometry and not the material combination: InAs nanomembranes.

Nanowires offer many possibilities when it comes to material combination, defect-free growth, crystal structure control, and abrupt radial and axial junctions. However, nowadays device fabrication has a large demand on different well-controlled geometries, like nanosails, rings or membranes [235, 236]. These structures can be fabricated effectively by etching. However, the surface will be damaged and complex structures and material combinations are hard to achieve. Therefore, growing these structures from the bottom up with the knowledge about nanowires, combines the amazing properties and possibilities of nanowires with flexible geometry, thus enabling an even higher degree of engineering for optical and electrical applications.

In Figure 7.14a, InAs nanomembranes are shown as an example for the progress of different geometries based on InAs nanowire growth. The nanomembranes have the form of sheets, but the knowledge about growth originates from the research about nanowires. The sample was grown by Naiyin Wang in Professor Chennupati Jagadish's group at ANU. These membranes have a length of 4 to 5 μm, a thickness between 54 nm and 116 nm and a width of 1 to 3 μm. A fluence-dependent series of PL spectra is shown in Figure 7.14b. The measurements were taken with the FTIR PL system. More information about this spectroscopic technique can be found in the former sections and in Chapter 4. The energy peak at 0.42 eV ($\lambda =$ 2.95 μm) confirms the zincblende crystal structure. Furthermore, a shoulder appears at around 0.43 eV ($\lambda = 2.88\,\mu$m), which becomes more pronounced with increasing excitation power density. The shoulder could be caused by surface states or high n-type doping [237]. Moreover, quantum confinement could also cause the shoulder. For InAs nanowires, quantum confinement appears for diameters smaller than 100 nm [215]. The nanomembrane's thickness vary largely from 54 nm to 116 nm. This is in the range which can cause quantum confinement. Also polytypism could cause a second peak. For a better understanding more investigation is necessary.

The current study gives an insight into the growing world of nanowire-based applications which is accelerated by combining new geometries with the knowledge about well-controlled growth and interesting properties, which was gained through research on nanowires. Such progress is reliant on the quantitative understanding of how composition and processing methods influence the optical properties of these materials.

8
Conclusion and Outlook

8.1 Summary

This thesis has been mostly concerned with the characterisation of special, promising materials for applications in the infrared, such as thermoelectric devices (InAsSb nanowires), photodetectors (InAs nanowires, InAsSb nanowires) and electrically driven nanowire lasers directly integrated on a silicon chip (hexagonal Si and SiGe nanowires). The various materials emit and absorb at different wavelengths and thus cover different spectral ranges in the IR. This work aims to build a bridge between the growth of nanowires and their fabrication into devices. The analysis of nanowires' optical and electrical properties enables one to give feedback about their growth, to understand their features and determine their optimum usage. It contributes to inspire industrial applications for nanowires.

In order to achieve a comprehensive study of nanowires with THz and PL spectroscopy, a home-built cryogenic mid-infrared Fourier Transform Photoluminescence setup was built (Chapter 4). This setup was optimised to measure the photoluminescence of nanowires emitting with low radiative efficiency in the infrared while saving cost and time.

In Chapter 5 different types of wurtzite GaP nanowires, which have a direct bandgap due to their hexagonal crystal structure, were investigated and analysed,

in order to find the optimal template for the growth of hexagonal Si and SiGe. Therefore, the growth defects were investigated because the hexagonal shell around the GaP core will inherit the defects of the core. For GaP nanowires, which are grown in one step, stacking fault densities resulting from the different precursor flow rates have been correlated to the photoconductivity lifetimes. Furthermore, the sample with a V/III ratio of 30.0 had the highest lifetime of 398 ps and the lowest defect density of $0.3\,\mu m^{-1}$. These nanowires were compared to wurtzite GaP nanowires grown with the two-step core-clad method. Although, the material composition is similar, the samples grown in two steps have a 11 times longer lifetime because the shell growth removed the detrimental chlorine passivation layer, while the samples grown with a single step had a chlorine layer. Furthermore, the nanowires grown in two steps are unintentionally doped with carbon atoms, which causes a decrease of the lifetime when excited with increasing laser fluence. A comparison of all these different types of nanowires lead to GaP wurtzite nanowires grown with the two-step core-clad method and a V/III ratio of 21.5 to be selected as the template for the growth of hexagonal silicon and silicon-germanium.

In Chapter 6, Si and SiGe in the lonsdaleite phase are discussed. These materials are highly interesting because of their predicted change in energy bands. Hexagonal SiGe has a direct bandgap, while its cubic counterpart has an indirect one. This makes the material ideal for optoelectronic devices, especially because SiGe is compatible with existing silicon-based technology. It was not achievable to demonstrate the theoretically predicted direct bandgap for SiGe by measuring the photoconductivity lifetime for samples with different amounts of germanium because other effects, such as the variation in shell thickness, had a larger influence on the lifetime. However, high accidental doping was detected. To reduce the doping density, the growth recipe was improved. It has also been demonstrated that certain morphologies, such as parasitic growth, are detrimental for efficient long-lived nanowires.

Additionally, the surface recombination velocity of 3.5×10^3 cm/s for hexagonal silicon was determined for the first time. It is therefore advisable to passivate future

hexagonal silicon nanowire devices. Furthermore, indications for a direct bandgap in silicon nanowires in the lonsdaleite phase were discovered and discussed on the base of THz and PL spectroscopy. Theoretically, the bandgap of hexagonal silicon is supposed to still be indirect, with the exception of hexagonal Si nanowires with a biaxial strain of 4% or more. This strain causing the direct bandgap is likely to be induced by the thin hexagonal silicon shell of 23 nm.

In Chapter 7, InAs and InAsSb nanowires were also characterised, in order to investigate their usage as detectors and light emitting devices in the mid-infrared around 0.4 eV. For a comprehensive overview of these type of nanowires, THz and PL spectroscopy were performed to extract the changes of optical and electrical properties for wires grown with different systems and recipes, with and without passivation. Furthermore, experiments were performed on pure-phase InAs nanowires in zincblende and wurtzite phase with various diameters. The broad overview enables choosing the right treatment on InAs nanowires for future infrared InAs applications and to adjust them individually to each device. Furthermore, the bandgap of a ternary material, InAsSb, with varying Sb contents, was extracted. The bandgap changed from 0.41 eV to 0.23 eV for 0% and 35% antimony content, respectively, in good agreement with theoretical calculations. The possibility of bandgap engineering and the demonstrated improvement in growth due to the Sb addition makes InAsSb nanowires ideal to cover applications in the mid-infrared region.

8.2 Further work

This thesis has presented new knowledge about nanowires fabricated with different compositions and growth methods. However, there is still a lot to be learned about them.

For example, the strain of the hexagonal silicon nanowires with the presumably direct bandgap needs to be measured and quantified, in order to confirm and improve theoretical calculations. This can be done by TEM measurements at which the relaxed, unstrained unit cell is compared to the unit cell of the strained

sample and then the strain is calculated. Furthermore, THz spectroscopy below the freezing point of the dopants would provide more information about the recombination processes without monomolecular radiative equations because the dopants are not active anymore. Measurements at different temperatures can also provide more information about the rate equation coefficients and the different types of recombination processes. Simultaneously, simulations about the different recombination processes and the dopants acting as traps and recombinations centres for the specific case of strained hexagonal silicon at different temperatures needs to be performed to complement the experiments. Furthermore, more samples need to be grown in order to develop a mature and reliable growth recipe for industrial applications. Additionally, the growth of SiGe nanowires in the lonsdaleite phase needs to be improved in order to examine further the existence of a direct bandgap. Using wurtzite GaAs as a template for the growth of hexagonal SiGe is another approach to achieve defect-free SiGe nanowires because the lattice constant of GaAs matches that of Ge [180, 181]. Defect-free, hexagonal SiGe nanowires with high germanium content are predicted by theory to have a direct bandgap. This theory can be confirmed by investigating these samples with PL and THz spectroscopy because semiconductors with indirect bandgaps have a longer photoluminescence and photoconductivity lifetime than semiconductors with direct bandgap. Furthermore, a photoluminescence spectrum can show if theory and the theoretical predicted bandgaps coincides with experiments. In general, different approaches, like the ones described above, need to be tested, in order to find the best options to produce efficient silicon and silicon compound devices with a direct bandgap and implement them into current technology.

For InAs nanowires and compounds the situation is different. These materials have been well-researched, and different parameters, such as crystal structure, geometry, and passivation, have been comprehensively discussed in this thesis. The next step is to explore different possibilities to engineer devices. InAsSb was introduced as an effective detector whose bandgap can be engineered method to engineered. In order to actually show that InAsSb nanowires are usable as

optoelectronic devices, devices need to be fabricated from these materials and then photocurrent spectroscopy can be performed on them. Devices can not only be engineered by composition, but also by geometry. The growth of new structures, such as nanomembranes and nanorings, is a promising, increasing field. These structures have a larger active area and different properties than the well-known nanowires, but the control, knowledge, and diversity achieved with wires can be applied for fabricating them. However, despite the knowledge gained by studying nanowires, a lot of research needs to be performed on the novel geometric, semiconductor structures and they need to be tested as devices.

Bibliography

[1] P. W. Coteus, J. U. Knickerbocker, C. H. Lam, and Y. A. Vlasov. Technologies for exascale systems. *J. Res. Dev.*, 55(5):1–12, 2011.

[2] H. J. Joyce, Q. Gao, H. Hoe Tan, C. Jagadish, Y. Kim, J. Zou, L. M. Smith, H. E. Jackson, J. M. Yarrison-Rice, P. Parkinson, and M. B. Johnston. III-V semiconductor nanowires for optoelectronic device applications. *Prog. Quantum Electron.*, 35(2-3):23–75, 2011.

[3] B. Mayer, L. Janker, B. Loitsch, J. Treu, T. Kostenbader, S. Lichtmannecker, T. Reichert, S. Morkötter, M. Kaniber, G. Abstreiter, C. Gies, G. Koblmüller, and J. J. Finley. Monolithically integrated high-beta nanowire lasers on silicon. *Nano Lett.*, 16(1):152–156, 2016.

[4] F. Qian, Y. Li, S. Gradecak, H.-G. Park, Y. Dong, Y. Ding, Z. L. Wang, and C. M. Lieber. Multi-quantum-well nanowire heterostructures for wavelength-controlled lasers. *Nat. Mater.*, 7:701–706, 2008.

[5] T. Tokuno, M. Nogi, M. Karakawa, J. Jiu, T. T. Nge, Yo. Aso, and K. Suganuma. Fabrication of silver nanowire transparent electrodes at room temperature. *Nano Res.*, 4(12):1215–1222, 2011.

[6] C. Zhao, N. Alfaraj, R. C. Subedi, J. W. Liang, A. A. Alatawi, A. A. Alhamoud, M. Ebaid, M. S. Alias, T. K. Ng, and B. S. Ooi. III-nitride nanowires on unconventional substrates : From materials to optoelectronic device applications. *Prog. Quantum Electron.*, 61:1–31, 2018.

[7] R. R. LaPierre, M. Robson, K. M. Azizur-Rahman, and P. Kuyanov. A review of III-V nanowire infrared photodetectors and sensors. *J. Phys. D. Appl. Phys.*, 50(12):1–10, 2017.

[8] R. E. Algra, M. A. Verheijen, M. T. Borgstrom, L. F. Feiner, G. Immink, W. J. van Enckevort, E. Vlieg, and E. P. Bakkers. Twinning superlattices in indium phosphide nanowires. *Nature*, 456(7220):369–372, 2008.

[9] R. S. Wagner and W. C. Ellis. Vapor-liquid-solid mechanism of single crystal growth. *Appl. Phys. Lett.*, 4(5):89–90, 1964.

[10] W. Seifert, M. Borgström, K. Deppert, K. A. Dick, J. Johansson, M. W. Larsson, T. Mårtensson, N. Skold, C. P. T. Svensson, B. A. Wacaser, L. R. Wallenberg, and L. Samuelson. Growth of one-dimensional nanostructures in MOVPE. *J. Cryst. Growth*, 272:211–220, 2004.

[11] M. Rauber, I. Alber, M. Sven, R. Neumann, O. Picht, C. Roth, A. Schökel, M. E. Toimil-Molares, and W. Ensinger. Highly-ordered supportless three-dimensional nanowire networks with tunable complexity and interwire connectivity for device integration. *Nano Lett.*, 11:2304–2310, 2011.

[12] F. Jabeen, S. Rubini, and F. Martelli. Growth of III-V semiconductor nanowires by molecular beam epitaxy. *Elsevier*, 40(3):442–445, 2009.

[13] K. W. Schwarz and J. Terso. Elementary process in NW growth. *Nano Lett.*, 11:316–320, 2011.

[14] C. Zhang and X. Li. III-V NW transistors for low-power logic applications-a review and outlook. *IEEE Trans. Electron Devices*, 63(1):223–234, 2016.

[15] A. Fontcuberta I Morral, C. Colombo, G. Abstreiter, J. Arbiol, and J. R. Morante. Nucleation mechanism of gallium-assisted molecular beam epitaxy growth of gallium arsenide nanowires. *Appl. Phys. Lett.*, 92(6):1–3, 2008.

[16] G. Koblmüller and G. Abstreiter. Growth and properties of InGaAs nanowires on silicon. *Phys. Status Solidi RRL*, 8(1):11–30, 2013.

[17] D. Rudolph, S. Hertenberger, S. Bolte, W. Paosangthong, D. Spirkovska, M. Döblinger, M. Bichler, J. J. Finley, G. Abstreiter, and G. Koblmüller. Direct observation of a noncatalytic growth regime for GaAs nanowires. *Nano Lett*, 11:3848–3854, 2011.

[18] D. Rudolph, L. Schweickert, S. Morkötter, B. Loitsch, S. Hertenberger, J. Becker, M. Bichler, G. Abstreiter, J. J. Finley, and G. Koblmüller. Effect of interwire separation on growth kinetics and properties of site-selective GaAs nanowires. *Appl. Phys. Lett.*, 105(3):1–5, 2014.

[19] M. Borg, H. Schmid, K. E. Moselund, G. Signorello, L. Gignac, J. Bruley, C. Breslin, P. D. Kanungo, P. Werner, and H. Riel. Vertical III-V nanowire device integration on Si(100). *Nano Lett.*, 14(4):1914–1920, 2014.

[20] H. Schmid, M. Borg, K. Moselund, L. Gignac, C. M. Breslin, J. Bruley, D. Cutaia, and H. Riel. Template-assisted selective epitaxy of III-V nanoscale devices for co-planar heterogeneous integration with Si. *Appl. Phys. Lett.*, 106(23):1–5, 2015.

[21] P. D. Kanungo, H. Schmid, M. T. Björk, L. M. Gignac, C. Breslin, J. Bruley, C. D. Bessire, and H. Riel. Selective area growth of III-V nanowires and their heterostructures on silicon in a nanotube template: towards monolithic integration of nano-devices. *Nanotechnology*, 24(22):1–6, 2013.

[22] M. Borg, H. Schmid, K. E. Moselund, D. Cutaia, and H. Riel. Mechanisms of template-assisted selective epitaxy of InAs nanowires on Si. *J. Appl. Phys.*, 117(14):1–7, 2015.

[23] R. E. Algra, M. Hocevar, M. A. Verheijen, I. Zardo, G. G.W. Immink, W. J. P. Van Enckevort, G. Abstreiter, L. P. Kouwenhoven, E. Vlieg, and E. P. A. M. Bakkers. Crystal structure transfer in core/shell nanowires. *Nano Lett.*, 11(4):1690–1694, 2011.

[24] L. Namazi, L. Gren, M. Nilsson, M. Garbrecht, C. Thelander, R. R. Zamani, and K. A. Dick. Realization of wurtzite GaSb using InAs nanowire templates. *Adv. Funct. Mater.*, 28(28):1–13, 2018.

[25] C. Deng, T. W. Sigmon, G. K. Giust, J. C. Wu, and M. N. Wybourne. Novel scheme to fabricate SiGe nanowires using pulsed ultraviolet laser induced epitaxy. *J. Vac. Sci. Technol. A*, 14(3):1860–1863, 1996.

[26] Y. Cui, X. Duan, J. Hu, and C. M. Lieber. Doping and electrical transport in Si NWs. *J. Phys. Chem. B*, 104(22):4–7, 2000.

[27] Y. Wu, R. Fan, and P. Yang. Block-by-block growth of single-crystalline Si/SiGe superlattice nanowires. 2(2):83–86, 2002.

[28] A. Zhang, G. Zheng, and C. M. Lieber. Nanowires - building blocks for nanoscience and nanotechnology. *Springer*, (3):1–322, 2016.

[29] A. Colli, F. Martelli, and S. Rubini. Growth of semiconductor nanowires by molecular beam epitaxy. *Elsevier*, pages 55–93, 2013.

[30] K. Ikejiri, T. Sato, H. Yoshida, K. Hiruma, J. Motohisa, S. Hara, and T. Fukui. Growth characteristics of GaAs nanowires obtained by selective area metal-organic vapour-phase epitaxy. *Nanotechnology*, 19(26):1–8, 2008.

[31] L. J. Lauhon, Mark S. Gudiksen, and Charles M. Lieber. Semiconductor nanowire heterostructures. *Philos. T. R. Soc. A.*, 362(1819):1247–1260, 2004.

[32] S. Conesa-Boj, F. Boioli, E. Russo-Averchi, S. Dunand, M. Heiss, D. Rüffer, N. Wyrsch, C. Ballif, L. Miglio, and A. Fontcuberta I Morral. Plastic and elastic strain fields in GaAs/Si core-shell nanowires. *Nano Lett.*, 14(4):1859–1864, 2014.

[33] X. Yan, S. Fan, X. Zhang, and X. Ren. Analysis of critical dimensions for nanowire core-multishell heterostructures. *Nanoscale Res. Lett.*, 10:1–7, 2015.

[34] L. Ma, W. Hu, Q. Zhang, P. Ren, X. Zhuang, H. Zhou, and J. Xu. Room-temperature near-infrared photodetectors based on single heterojunction nanowires. *Nano Lett.*, 14:694–698, 2014.

[35] W. Lu and C. M. Lieber. Semiconductor nanowires. *J. Phys. D. Appl. Phys.*, 39(21):387–406, 2006.

[36] D. Rudolph, S. Funk, M. Döblinger, S. Morkötter, S. Hertenberger, L. Schweickert, J. Becker, S. Matich, M. Bichler, D. Spirkoska, I. Zardo, J. J. Finley, G. Abstreiter, and G. Koblmüller. Spontaneous alloy composition ordering in GaAs-AlGaAs core-shell nanowires. *Nano Lett.*, 13(4):1522–1527, 2013.

[37] T. Stettner, P. Zimmermann, B. Loitsch, M. Döblinger, A. Regler, B. Mayer, J. Winnerl, S. Matich, H. Riedl, M. Kaniber, G. Abstreiter, G. Koblmüller, and J. J. Finley. Coaxial GaAs-AlGaAs core-multishell nanowire lasers with epitaxial gain control. *Appl. Phys. Lett.*, 108(1):1–5, 2016.

[38] A. Alhodaib, Y. J. Noori, P. J. Carrington, A. M. Sanchez, M. D. Thompson, R. J. Young, A. Krier, and A. R. J. Marshall. Room-temperature mid-infrared emission from faceted InAsSb multi quantum wells embedded in InAs nanowires. *Nano Lett.*, 18(1):235–240, 2018.

[39] E. C. Garnett, M. L. Brongersma, Y. Cui, and M. D. Mcgehee. Nanowire solar cells. *Annu. Rev. Mater. Res.*, (41):269–295, 2011.

[40] S. Morkötter, N. Jeon, D. Rudolph, B. Loitsch, D. Spirkoska, E. Hoffmann, M. Döblinger, S. Matich, J. J. Finley, L. J. Lauhon, G. Abstreiter, and G. Koblmüller. Demonstration of confined electron gas and steep-slope behavior in delta-doped GaAs-AlGaAs core-shell nanowire transistors. *Nano Lett.*, 15(5):3295–3302, 2015.

[41] C. K. Yong, K. Noori, Q. Gao, H. J. Joyce, H. H. Tan, C. Jagadish, F. Giustino, M. B. Johnston, and L. M. Herz. Strong carrier lifetime enhancement in GaAs nanowires coated with semiconducting polymer. *Nano Lett.*, 12(12):6293–6301, 2012.

[42] J. L. Boland, S. Conesa-Boj, P. Parkinson, G. Tütüncüoglu, F. Matteini, D. Rüffer, A. Casadei, F. Amaduzzi, F. Jabeen, C. L. Davies, H. J. Joyce, L. M. Herz, A. Fontcuberta I Morral, and M. B. Johnston. Modulation doping of GaAs/AlGaAs core-shell nanowires with effective defect passivation and high electron mobility. *Nano Lett.*, 15(2):1336–1342, 2015.

[43] A. D. Mallorqui, E. Alarcón-Lladó, I. Canales Mundet, A. Kiani, B. Demaurex, S. De Wolf, A. Menzel, M. Zacharias, and A. Fontcuberta i Morral. Field-effect passivation on silicon nanowire solar cells. *Nano Res.*, 8(2):673–681, 2015.

[44] M. Paladugu, J. Zou, Y. N. Guo, X. Zhang, H. J. Joyce, Q. Gao, H. H. Tan, C. Jagadish, and Y. Kim. Evolution of wurtzite structured GaAs shells around InAs nanowire cores. *Nanoscale Res. Lett.*, 4(8):846–849, 2009.

[45] H. I. T. Hauge, M. A. Verheijen, S. Conesa-Boj, T. Etzelstorfer, M. Watzinger, D. Kriegner, I. Zardo, C. Fasolato, F. Capitani, P. Postorino, S. Kölling, A. Li, S. Assali, J. Stangl, and E. P. A. M. Bakkers. Hexagonal silicon realized. *Nano Lett.*, 15(9):5855–5860, 2015.

[46] R. E. Hanneman, H. M. Strong, and F. P. Bundy. Hexagonal diamonds in meteorites: implications. *Science*, 155(3765):995–997, 1967.

[47] C. Frondel and U. B. Marvin. Londsdaleite, a hexagonal polymorph of diamond. *Nature*, 214:587–589, 1967.

[48] P. Caroff, J. Bolinsson, and J. Johansson. Crystal phases in III-V nanowires: from random toward engineered polytypism. *IEEE J. Sel. Top Quant.*, 17(4):829–846, 2011.

[49] Q. Fan, C. Chai, Q. Wei, K. Wong, Y. Liu, and Y. Yang. Theoretical investigations of group IV alloys in the lonsdaleite phase. *J. Mater. Sci.*, 53(4):2785–2801, 2018.

[50] S. Dixit and A. K. Shukla. Optical properties of lonsdaleite silicon nanowires: a promising material for optoelectronic applications. *J. Appl. Phys.*, 123(22):1–7, 2018.

[51] M. B. Rota, A. S. Ameruddin, A. Wong-Leung, J.and Belabbes, Q. Gao, A. Miriametro, F. Mura, H. H. Tan, A. Polimeni, F. Bechstedt, C. Jagadish, and M. Capizzi. Critical temperature for the conversion from wurtzite to zincblende of the optical emission of InAs nanowires. *J. Phys. Chem. C*, 121(30):16650–16656, 2017.

[52] J. Greil, S. Assali, Y. Isono, A. Belabbes, F. Bechstedt, F. O. Valega MacKenzie, A. Yu Silov, E. P. A. M. Bakkers, and J. E. M. Haverkort. Optical properties of strained wurtzite gallium phosphide nanowires. *Nano Lett.*, 16(6):3703–3709, 2016.

[53] S. Q. Wang and H. Q. Ye. First-principles study on the lonsdaleite phases of C, Si and Ge. *J. Phys. Condens. Matter*, 15(12):197–202, 2003.

[54] M. Raya-Moreno, H. Aramberri, J. A. Seijas-Bellido, X. Cartoixà, and R. Rurali. Thermal conductivity of hexagonal Si and hexagonal Si nanowires from first-principles. *Appl. Phys. Lett.*, 111(3):1–5, 2017.

[55] C. Thelander, P. Caroff, S. Plissard, A. W. Dey, and K. A. Dick. Effects of crystal phase mixing on the electrical properties of InAs nanowires. *Nano Lett.*, 11:2424–2429, 2011.

[56] R. Gross and A. Marx. Festkörpephysik. *Oldenbourg*, pages 1–982, 2012.

[57] P. S. Chen, S. T. Fan, H. S. Lan, and C. W. Liu. Band calculation of lonsdaleite Ge. *J. Phys. D. Appl. Phys.*, 50(1):1–6, 2017.

[58] F. Bechstedt and A. Belabbes. Structure, energetics, and electronic states of III-V compound polytypes. *J. Phys. Condens. Matter*, 25(27):1–27, 2013.

[59] N. G. Hörmann, I. Zardo, S. Hertenberger, S. Funk, S. Bolte, M. Döblinger, G. Koblmüller, and G. Abstreiter. Effects of stacking variations on the lattice dynamics of InAs nanowires. *Phys. Rev. B*, 84(15):1–7, 2011.

[60] A. De and C. E. Pryor. Electronic structure and optical properties of Si, Ge and diamond in the lonsdaleite phase. *J. Physics-Condensed Matter*, 26:1–16, 2014.

[61] H. Zheng, J. Wang, J. Y. Huang, J. Wang, Z. Zhang, and S. X. Mao. Dynamic process of phase transition from wurtzite to zinc blende structure in InAs nanowires. *Nano Lett.*, 13(12):6023–6027, 2013.

[62] E. A. Anyebe, M. K. Rajpalke, T. D. Veal, C. J. Jin, Z. M. Wang, and Q. D. Zhuang. Surfactant effect of antimony addition to the morphology of self-catalyzed $InAs_{1-x}Sb_x$ nanowires. *Nano Res.*, 8(4):1309–1319, 2015.

[63] L. Vincent, D. Djomani, M. Fakfakh, C. Renard, B. Belier, D. Bouchier, and G. Patriarche. Shear-driven phase transformation in silicon nanowires. *Nanotechnology*, 29(12):1–7, 2018.

[64] K. A. Dick, P. Caroff, J. Bolinsson, M. E. Messing, J. Johansson, K. Deppert, L. R. Wallenberg, and L. Samuelson. Control of III–V nanowire crystal structure by growth parameter tuning. *Semicond. Sci. Technol.*, 25(2):1–11, 2010.

[65] Z. Ikonic, G. P. Srivastava, and J. C. Inkson. Optical properties of twinning superlattices in diamond-type and zinc-blende-type semiconductors. *Phys. Rev. B*, 52(19):78–85, 1995.

[66] K. A. Dick, C. Thelander, L. Samuelson, and P. Caroff. Crystal phase engineering in single InAs nanowires. *Nano Lett.*, 10(9):3494–3499, 2010.

[67] J. Wallentin and M. T. Borgström. Doping of semiconductor nanowires. *J. Mater. Res.*, 26(17):2142–2156, 2011.

[68] Q. D. Zhuang, E. A. Anyebe, R. Chen, H. Liu, A. M. Sanchez, M. K. Rajpalke, T. D. Veal, Z. M. Wang, Y. Z. Huang, and H. D. Sun. Sb-Induced phase control of InAsSb nanowires grown by molecular beam epitaxy. *Nano Lett.*, 15(2):1109–1116, 2015.

[69] H. Potts, M. Friedl, F. Amaduzzi, K. Tang, G. Tütüncüoglu, F. Matteini, E. Alarcon Lladó, P. C. McIntyre, and A. Fontcuberta I Morral. From twinning to pure zincblende catalyst-free InAs(Sb) nanowires. *Nano Lett.*, 16(1):637–643, 2016.

[70] M. J. L. Sourribes, I. Isakov, M. Panfilova, H. Liu, and P. A. Warburton. Mobility enhancement by Sb-mediated minimisation of stacking fault density in InAs nanowires grown on silicon. *Nano Lett.*, 14(3):1–10, 2014.

[71] D. E. Perea, E. R. Hemesath, E. J. Schwalbach, J. L. Lensch-Falk, P. W. Voorhees, and L. J. Lauhon. Direct measurement of dopant distribution in an individual vapour-liquid-solid nanowire. *Nat. Nanotechnol.*, 4(5):315–319, 2009.

[72] M. Möller, D. S. Oliveira, P. K. Sahoo, M. A. Cotta, F. Iikawa, P. Motisuke, A. Molina-Sánchez, M. M. De Lima, A. García-Cristóbal, and A. Cantarero. Fermi energy dependence of the optical emission in core/shell InAs nanowire homostructures. *Nanotechnology*, 28(29):1–6, 2017.

[73] B.I. Shlovskii and A.L. Efros. Electric properties of doped semiconductors. *Springer*, pages 1–390, 1984.

[74] S. M. Sze. Physics of semiconductor devices. *Wiley*, pages 1–812, 1969.

[75] Hunklinger, S. Festkörperphysik. *Oldenbourg*, 2:1–595, 2009.

[76] A. C. Peacock and N. Healy. Semiconductor optical fibres for infrared applications: A review. *Semicond. Sci. Technol.*, 31(10):1–12, 2016.

[77] K. M. Evenson, D. A. Jennings, and F. R. Peterson. Tunable far-infrared spectroscopy. *Appl. Phys. Lett.*, 44(6):576–678, 1984.

[78] C. Kittel. Introduction to Solid State Physics. *Wiley*, 8:1–680, 2005.

[79] L. M. Herz. Charge-carrier dynamics in organic-inorganic metal halide perovskites. *Annu. Rev. Phys. Chem.*, 67(1):65–89, 2016.

[80] R. L. Milot, G. E. Eperon, H. J. Green, T.and Snaith, M. B. Johnston, and L. M. Herz. Radiative monomolecular recombination boosts amplified spontaneous emission in $HC(NH_2)_2SnI_3$ perovskite films. *J. Phys. Chem. Lett.*, 7(20):4178–4184, 2016.

[81] S. S. Iyer and Y. H. Xie. Light emission from silicon. *Science*, 260(5104):40–46, 1993.

[82] C. Liu, L. Dai, L. P. You, W. J. Xu, and G. G. Qin. Blueshift of electroluminescence from single n-InP nanowire/p-Si heterojunctions due to the Burstein-Moss effect. *Nanotechnology*, 19(46):1–5, 2008.

[83] P. T. Landsberg. Recombination in Semiconductors. *Cambridge University Press*, pages 1–595, 1991.

[84] C. Wehrenfennig, G. E. Eperon, M. B. Johnston, H. J. Snaith, and L. M. Herz. High charge carrier mobilities and lifetimes in organolead trihalide perovskites. *Adv. Mater.*, 26(10):1584–1589, 2014.

[85] M. B. Johnston and L. M. Herz. Hybrid perovskites for photovoltaics: charge-carrier recombination, diffusion, and radiative efficiencies. *Acc. Chem. Res.*, 49(1):146–154, 2016.

[86] J. L. Boland, A. Casadei, G. Tütüncüoglu, F. Matteini, C. L. Davies, F. Jabeen, H. J. Joyce, L. M. Herz, A. Fontcuberta i Morral, and M. B. Johnston. Increased photoconductivity lifetime in GaAs nanowires by controlled n-type and p-type doping. *ACS Nano*, 10(4):4219–4227, 2016.

[87] B. Mayer, D. Rudolph, J. Schnell, S. Morkötter, J. Winnerl, J. Treu, K. Müller, G. Bracher, G. Abstreiter, G. Koblmüller, and J. J. Finley. Lasing from individual GaAs-AlGaAs core-shell nanowires up to room temperature. *Nat. Commun.*, 4(2931):1–7, 2013.

[88] J. L. Boland, F. Amaduzzi, S. Sterzl, H. Potts, L. M. Herz, A. Fontcuberta I Morral, and M. B. Johnston. High electron mobility and insights into temperature-dependent scattering mechanisms in InAsSb nanowires. *Nano Lett.*, 18(6):3703–3710, 2018.

[89] K. Yang, A. Cantarero, A. Rubio, and R. D'Agosta. Optimal thermoelectric figure of merit of Si/Ge core-shell nanowires. *Nano Res.*, 8(8):2611–2619, 2015.

[90] O. Caballero-Calero and M. Martín-González. Thermoelectric nanowires: a brief prospective. *Scr. Mater.*, 111:54–57, 2016.

[91] Y. Tian, M. R. Sakr, J. M. Kinder, D. Liang, M. J. MacDonald, R. L. J. Qiu, H.-J. Gao, and X. P. A. Gao. One-dimensional quantum confinement effect modulated thermoelectric properties in InAs nanowires. *Nano Lett.*, 12(12):6492–6497, 2012.

[92] J. Moon, J.-H. Kim, Z. C. Y. Chen, J. Xiang, and R. Chen. Gate-modulated thermoelectric power factor of hole gas in Ge-Si core-shell nanowires. *Nano Lett.*, 13:1196–1202, 2013.

[93] Y. Yang, W. Guo, K. C. Pradel, G. Zhu, Y. Zhou, Y. Zhang, Y. Hu, L. Lin, and Z. L. Wang. Pyroelectric nanogenerators for harvesting thermoelectric energy. *Nano Lett.*, 12(6):2833–2838, 2012.

[94] E. Garnett and P. Yang. Light trapping in silicon nanowire solar cells. *Nano Lett.*, 10(3):1082–1087, 2010.

[95] F. Lindelöw, M. Heurlin, G. Otnes, V. Daghté, D. Lindgren, O. Hultin, K. Storm, L. Samuelson, and M. Borgström. Doping evaluation of InP nanowires for tandem junction solar cells. *Nanotechnology*, 27:1–6, 2016.

[96] A. K. Sood, J. W. Zeller, R. A. Richwine, Y. R. Puri, P. Efstathiadis, H.and Haldar, N. K. Dhar, and D. L. Polla. Advances in optical fiber technology: fundamental optical phenomena and applications. *IntechOpen*, pages 315–361, 2015.

[97] L. Cao and M. L. Brongersma. Engineering light absorption in semiconductor nanowire devices. *Nat. Mater.*, 8(8):643–647, 2009.

[98] C. M. Natarajan, M. G. Tanner, and R. H. Hadfield. Superconducting nanowire single-photon detectors: physics and applications. *Supercond. Sci. Technol.*, 25(6):1–16, 2012.

[99] S. Ferrari, O. Kahl, V. Kovalyuk, G. N. Goltsman, A. Korneev, and W. H. P. Pernice. Waveguide-integrated single- and multi-photon detection at telecom wavelengths using superconducting nanowires. *Appl. Phys. Lett.*, 106(15):1–5, 2015.

[100] H. Takesue, S. D. Dyer, M. J. Stevens, V. Verma, R. P. Mirin, and S. W. Nam. Quantum teleportation over 100 km of fiber using highly efficient superconductiong NW single-photon-detectors. *Optica*, 2(10):20–23, 2015.

[101] K. Tomioka, J. Motohisa, K. Hara, S.and Hiruma, and T. Fukui. GaAs/AlGaAs core multishell nanowire-based light-emitting diodes on Si. *Nano Lett.*, 10(5):1639–1644, 2010.

[102] E. D. Minot, F. Kelkensberg, M. Van Kouwen, J. A. Van Dam, L. P. Kouwenhoven, V. Zwiller, M. T. Borgström, O. Wunnicke, M. A. Verheijen, and E. P. A. M. Bakkers. Single quantum dot nanowire LEDs. *Nano Lett.*, 7(2):367–371, 2007.

[103] X. Duan, Y. Huang, R. Agarwal, and C. M. Lieber. Single-nanowire electrically driven lasers. *Nature*, 421(6920):241–245, 2003.

[104] D. Saxena, S. Mokkapati, P. Parkinson, N. Jiang, Q. Gao, H. H. Tan, and C. Jagadish. Optically pumped room-temperature GaAs nanowire lasers. *Nat. Photonics*, 7(12):963–968, 2013.

[105] T. M. Babinec, B. J. M. Hausmann, M. Khan, Y. Zhang, J. R. Maze, P. R. Hemmer, and M. Loncar. A diamond nanowire single-photon source. *Nat. Nanotechnol.*, 5(3):195–199, 2010.

[106] P. W. Milonni and J.H. Eberly. Laser physics. *Wiley*, 1:1–831, 2010.

[107] S. Hooker and C. Webb. Laser physics. *Oxford University Press*, 1:1–586, 201.

[108] C. Z. Ning. Semiconductor nanolasers. *Phys. statur solidi b*, 4(2):774–788, 2010.

[109] R. Röder, T. P. H. Sidiropoulos, C. Tessarek, S. Christiansen, R. F. Oulton, and C. Ronning. Ultrafast dynamics of lasing semiconductor nanowires. *Nano Lett.*, 15(7):4637–4643, 2015.

[110] B. Mayer, A. Regler, S. Sterzl, T. Stettner, G. Koblmüller, M. Kaniber, B. Lingnau, K. Lüdge, and J. J. Finley. Long-term mutual phase locking of picosecond pulse pairs generated by a semiconductor nanowire laser. *Nat. Commun.*, 8(15521):1–6, 2017.

[111] B. Piccione, C.-H. Cho, L. K. van Vugt, and R. Agarwal. All-optical active switching in individual semiconductor nanowires. *Nat. Nanotechnol.*, 7(10):640–645, 2012.

[112] H. J. Joyce, J. L. Boland, C. L. Davies, S. A. Baig, and M. B. Johnston. A review of the electrical properties of semiconductor nanowires: insights gained from terahertz conductivity spectroscopy. *Semicond. Sci. Technol.*, 31(10):1–21, 2016.

[113] S. S. Dhillon, M. S. Vitiello, E. H. Linfield, A. G. Davies, M. C. Hoffmann, J. Booske, C. Paoloni, M. Gensch, P. Weightman, G. P. Williams, E. Castro-Camus, D. R. S. Cumming, F. Simoens, I. Escorcia-Carranza, J. Grant, S. Lucyszyn, M. Kuwata-Gonokami, K. Konishi, M. Koch, C. A. Schmuttenmaer, T. L. Cocker, R. Huber, A. G. Markelz, Z. D. Taylor, V. P. Wallace, A. J. Zeitler, J. Sibik, T. M. Korter, B. Ellison, S. Rea, P. Goldsmith, K. B. Cooper, R. Appleby, D. Pardo, P. G. Huggard, V. Krozer, H. Shams, M. Fice, C. Renaud, A. Seeds, A. Stöhr, M. Naftaly, N. Ridler, R. Clarke, J. E. Cunningham, and M. B. Johnston. The 2017 terahertz science and technology roadmap. *J. Phys. D. Appl. Phys.*, 50(4):1–49, 2017.

[114] P. W. Parkinson. Ultrafast electronic processes at nanoscale organic-inorganic semiconductor interfaces. pages 1–172, 2008.

[115] R. Ulbricht, E. Hendry, J. Shan, T. F. Heinz, and M. Bonn. Carrier dynamics in semiconductors studied with time-resolved terahertz spectroscopy. *Rev. Mod. Phys.*, 83(2):543–586, 2011.

[116] K. Reimann. Table-top sources of ultrashort THz pulses. *Reports Prog. Phys.*, 1597(10):1597–1632, 2007.

[117] K. Peng, P. Parkinson, J. L. Boland, Q. Gao, Y.C. Wenas, C. L. Davies, Z. Li, L. Fu, M. B. Johnston, H. H. Tan, and C. Jagadish. Broadband phase-sensitive single InP nanowire photoconductive Terahertz detectors. *Nano Lett.*, 16(8):4925–4931, 2016.

[118] T. Kampfrath, M. Battiato, P. Maldonado, G. Eilers, J. Nötzold, S. Mährlein, V. Zbarsky, F. Freimuth, Y. Mokrousov, S. Blügel, M. Wolf, I. Radu, P. M. Oppeneer, and M. Münzenberg. Terahertz spin current pulses controlled by magnetic heterostructures. *Nat. Nanotechnol.*, 8(4):256–260, 2013.

[119] T. Seifert, S. Jaiswal, U. Martens, J. Hannegan, L. Braun, P. Maldonado, F. Freimuth, A. Kronenberg, J. Henrizi, I. Radu, E. Beaurepaire, Y. Mokrousov, P. M. Oppeneer, M. Jourdan, G. Jakob, D. Turchinovich, L. M. Hayden, M. Wolf, M. Münzenberg, M. Kläui, and T. Kampfrath. Efficient metallic spintronic emitters of ultrabroadband terahertz radiation. *Nat. Photonics*, 10(7):483–488, 2016.

[120] T. Seifert, S. Jaiswal, M. Sajadi, G. Jakob, S. Winnerl, M. Wolf, M. Kläui, and T. Kampfrath. Ultrabroadband single-cycle terahertz pulses with peak fields of 300 kV cm^{-1} from a metallic spintronic emitter. *Appl. Phys. Lett.*, 110(25):1–5, 2017.

[121] G.-S. Park, Y. H. Kim, H. Han, Jo. K. Han, J. Ahn, J.-H. Son, W.-Y. Park, and Y. U. Jeong. Convergence of Terahertz sciences in biomedical systems. *Springer*, pages 1–435, 2012.

[122] A. Nahata, A. S. Weling, and T. F. Heinz. A wideband coherent terahertz spectroscopy system using optical rectification and electro-optic sampling. *Appl. Phys. Lett.*, 69(16):2321–2323, 1996.

[123] G. Gallot, J. Zhang, R. W. McGowan, T. I. Jeon, and D. Grischkowsky. Measurements of the THz absorption and dispersion of ZnTe and their relevance to the electro-optic detection of THz radiation. *Appl. Phys. Lett.*, 74(23):3450–3452, 1999.

[124] J. H. Strait, P. A. George, M. Levendorf, M. Blood-Forsythe, F. Rana, and J. Park. Measurements of the carrier dynamics and terahertz response of oriented germanium nanowires using optical-pump Terahertz-probe spectroscopy. *Nano Lett.*, 9(8):2967–2972, 2009.

[125] H. J. Joyce, C. J. Docherty, Q. Gao, H. H. Tan, C. Jagadish, J. Lloyd-Hughes, L. M. Herz, and M. B. Johnston. Electronic properties of GaAs, InAs and InP nanowires studied by terahertz spectroscopy. *Nanotechnology*, 24(21):1–7, 2013.

[126] B. R. Bennett, R. A. Soref, and J. A. Del Alamo. Carrier-induced change in refractive index of InP, GaAs, and InGaAsP. *IEEE J. Quantum Electron.*, 26(1):113–122, 1990.

[127] X. Tu, J. Wei, B. Wang, Y. Tang, J. Shi, and Y. Chen. Patterned parylene C for cell adhesion, spreading and alignment studies. *Microelectron. Eng.*, 175:56–60, 2017.

[128] W. F. Gorham. A new, general synthetic method for the preparation of linear poly-p-xylylenes. *J. Polym. Sci. Part A*, 4(12):3027–3039, 1966.

[129] C. L. Davies, J. B. Patel, C. Q. Xia, L. M. Herz, and M. B. Johnston. Temperature-dependent refractive index of quartz at Terahertz frequencies. *J. Infrared, Millimeter, Terahertz Waves*, 39(12):1236–1248, 2018.

[130] B. Guilhabert, A. Hurtado, D. Jevtics, Q. Gao, H. H. Tan, C. Jagadish, and M. D. Dawson. Transfer printing of semiconductor nanowires with lasing emission for controllable nanophotonic device fabrication. *ACS Nano*, 10(4):3951–3958, 2016.

[131] A. Hurtado, B. Jevtics, D.and Guilhabert, Q. Gao, H. H. Tan, C. Jagadish, and M. D. Dawson. Novel nanoscale transfer printing technique for precise positioning of nanowire lasers. *SPIE Newsroom*, (2):10–12, 2017.

[132] S. Assali, J. Greil, I. Zardo, A. Belabbes, M. W.A. De Moor, S. Koelling, P. M. Koenraad, F. Bechstedt, E. P.A.M. Bakkers, and J. E.M. Haverkort. Optical study of the band structure of wurtzite GaP nanowires. *J. Appl. Phys.*, 120(4):1–10, 2016.

[133] W. Herres and J. Gronholz. Understanding FT-IR Data Processing. *Series*, pages 1–23.

[134] Bruker Optic GmbH. *OPUS / IR reference manual.* 2011.

[135] A. Belabbes, C. Panse, J. Furthmüller, and F. Bechstedt. Electronic bands of III-V semiconductor polytypes and their alignment. *Phys. Rev. B*, 86(7):1–12, 2012.

[136] N. N. Halder, S. Cohen, D. Gershoni, and D. Ritter. Growth of large diameter pure phase wurtzite GaP nanowires by a two-step axial-radial growth approach. *Appl. Phys. Lett.*, 112(13):1–4, 2018.

[137] A. De and C. E. Pryor. Predicted band structures of III-V semiconductors in the wurtzite phase. *Phys. Rev. B*, 81(15):1–13, 2010.

[138] A. Belabbes and F. Bechstedt. Forbidden band-edge excitons of wurtzite-GaP: a theoretical view. *Phys. Status Solidi Basic Res.*, 256(2):1–6, 2019.

[139] C.-Y. Yeh, Z. W. Lu, S. Froyen, and A. Zunger. Zinc-blende-wurtzite polytypism in semiconductors. *Phys. Rev. B*, 46(16):10086–10097, 1992.

[140] S. Assali, I. Zardo, S. Plissard, D. Kriegner, M. A. Verheijen, G. Bauer, A. Meijerink, A. Belabbes, F. Bechstedt, J. E.M. Haverkort, and E. P.A.M. Bakkers. Direct band gap wurtzite gallium phosphide nanowires. *Nano Lett.*, 13(4):1559–1563, 2013.

[141] S. Conesa-Boj, H. I.T. Hauge, M. A. Verheijen, S. Assali, A. Li, E. P. A. M. Bakkers, and A. Fontcuberta I Morral. Cracking the Si shell growth in hexagonal GaP-Si core-shell nanowires. *Nano Lett.*, 15(5):2974–2979, 2015.

[142] A. Berg, S. Lehmann, N. Vainorius, A. Gustafsson, M. E. Pistol, L. R. Wallenberg, L. Samuelson, and M. T. Borgström. Growth and characterization of wurtzite GaP nanowires with control over axial and radial growth by use of HCl in-situ etching. *J. Cryst. Growth*, 386:47–51, 2014.

[143] S. Conesa-Boj, I. Zardo, S. Estradé, L. Wei, P. Jean Alet, P. Roca i Cabarrocas, J. R. Morante, F. Peiró, A. Fontcuberta I Morral, and J. Arbiol. Defect formation in Ga-catalyzed silicon nanowires. *Cryst. Growth Des.*, 10(4):1534–1543, 2010.

[144] Z. Zhang, Z. Lu, H. Xu, P. Chen, W. Lu, and J. Zou. Structure and quality controlled growth of InAs nanowires through catalyst engineering. *Nano Res.*, 7(11):1640–1649, 2014.

[145] D. Dalacu, K. Mnaymneh, J. Lapointe, X. Wu, P. J. Poole, G. Bulgarini, V. Zwiller, and M. E. Reimer. Ultraclean emission from InAsP quantum dots in defect-free wurtzite InP nanowires. *Nano Lett.*, 12(11):5919–5923, 2012.

[146] C. Thelander, K. A. Dick, M. T. Borgström, L. E. Fröberg, P. Caroff, H. A. Nilsson, and L. Samuelson. The electrical and structural properties of n-type InAs nanowires grown from metal-organic precursors. *Nanotechnology*, 21(20):1–9, 2010.

[147] Y. Cao, J. Zhang, X. Li, T. H. Kosel, P. Fay, D. C. Hall, X. B. Zhang, R. D. Dupuis, J. B. Jasinski, and Z. Liliental-Weber. Electrical properties of InAlP native oxides for metal-oxide-semiconductor device applications. *Appl. Phys. Lett.*, 86(6):1–3, 2005.

[148] P. Parkinson, J. Lloyd-Hughes, Q. Gao, H. H. Tan, C. Jagadish, M. B. Johnston, and L. M. Herz. Transient terahertz conductivity of GaAs nanowires. *Nano Lett.*, 7(7):2162–2165, 2007.

[149] P. Parkinson, H. J. Joyce, Q. Gao, H. H. Tan, X. Zhang, J. Zou, C. Jagadish, L. M. Herz, and M. B. Johnston. Carrier lifetime and mobility enhancement in nearly defect-free core- shell nanowires measured using time-resolved Terahertz spectroscopy. *Nano Lett.*, 9(9):3349–3353, 2009.

[150] S. Assali, L. Gagliano, D. S. Oliveira, M. A. Verheijen, S. R. Plissard, L. F. Feiner, and E. P. A. M. Bakkers. Exploring crystal phase switching in GaP nanowires. *Nano Lett.*, 15(12):8062–8069, 2015.

[151] B. Libby. Let there be light. *Nature*, 409:975–976, 2001.

[152] D. A. B. Miller. Silicon integrated circuits shine. *Nature*, 384:307–308, 1996.

[153] A. G. Cullis and L.T. Canham. Visible light emission due to quantum size effects in highly porous crystalline silicon. *Nature*, 353:335–338, 1991.

[154] L. Vivien. Silicon chips lighten up. *Nature*, 528:483–484, 2015.

[155] D. A. B. Miller. Device requirements for optical interconnects to silicon chips. *Proc. IEEE*, 97(7):1166–1185, 2009.

[156] S. Manna, N. Prtljaga, S. Das, N. Daldosso, S. K. Ray, and L. Pavesi. Photophysics of resonantly and non-resonantly excited erbium doped Ge nanowires. *Nanotechnology*, 23(6):1–7, 2012.

[157] G. D. Sanders and Y. Chang. Theory of optical properties of quantum wires in porous silicon. *Phys. Rev. B*, 45(16):9202–9213, 1992.

[158] F. Buda, J. Kohanoff, and M. Parrinello. Optical properties of porous silicon: a first-principles study. 69(8):1272–1276, 1992.

[159] L.T. Canham. Silicon quantum wire array fabrication by electrochemical and chemical dissolution of wafers. *Appl. Phys. Lett.*, 57(10):1046–1048, 1990.

[160] C. Qi, G. Goncher, R. Solanki, and J. Jordan. SiGe nanowire growth and characterization. *Nanotechnology*, 18(7):1–5, 2007.

[161] J. W. Ma, W. J. Lee, J. M. Bae, K. S. Jeong, S. H. Oh, J. H. Kim, S. H. Kim, J. H. Seo, J. P. Ahn, H. Kim, and M. H. Cho. Carrier mobility enhancement of tensile strained Si and SiGe nanowires via surface defect engineering. *Nano Lett.*, 15(11):7204–7210, 2015.

[162] H. Presting. Near and mid infrared silicon/germanium based photodetection. *Thin Solid Films*, 321(1-2):186–195, 1998.

[163] S. K. Ray, A. K. Katiyar, and A. K. Rayachaudhuri. One-dimensional Si/Ge nanowires and their heterostructures for multifunctional applications - a review. *Nanotechnology*, 28:1–40, 2017.

[164] S. Wong, B. Haberl, B. C. Johnson, A. Mujica, M. Guthrie, J. C. McCallum, J. S. Williams, and J. E. Bradby. Formation of an r8-dominant Si material. *Phys. Rev. Lett.*, 122(10):1–6, 2019.

[165] B. Haberl, M. Guthrie, B. D. Malone, J. S. Smith, S. V. Sinogeikin, M. L. Cohen, J. S. Williams, G. Shen, and J. E. Bradby. Controlled formation of metastable germanium polymorphs. *Phys. Rev. B*, 89(14):16–21, 2014.

[166] L. Vincent, G. Patriarche, G. Hallais, C. Renard, C. Gardès, D. Troadec, and D. Bouchier. Novel heterostructured Ge nanowires based on polytype transformation. *Nano Lett.*, 14(8):4828–4836, 2014.

[167] L. Tsybeskov, K. Moore, and D. Hall. Intrinsic band-edge photoluminescence from silicon clusters at room temperature. *Phys. Rev. B*, 54(12):8361–8364, 1996.

[168] C. Rödl, T. Sander, F. Bechstedt, J. Vidal, P. Olsson, S. Laribi, and J. F. Guillemoles. Wurtzite silicon as a potential absorber in photovoltaics: tailoring the optical absorption by applying strain. *Phys. Rev. B*, 92(4):1–7, 2015.

[169] M. Amato, T. Kaewmaraya, A. Zobelli, M. Palummo, and R. Rurali. Crystal phase effects in Si nanowire polytypes and their homojunctions. *Nano Lett.*, 16(9):5694–5700, 2016.

[170] X. Cartoixà, M. Palummo, H. I. T. Hauge, E. P. A. M. Bakkers, and R. Rurali. Optical emission in hexagonal SiGe nanowires. *Nano Lett.*, 17(8):4753–4758, 2017.

[171] R. H. Jr. Wentorf and J. S. Kasper. Two new forms of silicon. *Science*, 139(3552):338–339, 1963.

[172] J. Bandet, B. Despax, and M. Caumont. Vibrational and electronic properties of stabilized wurtzite-like silicon. *J. Phys. D. Appl. Phys.*, 35(3):234–239, 2002.

[173] J. Tang, J. L. Maurice, F. Fossard, I. Florea, W. Chen, E. V. Johnson, M. Foldyna, L. Yu, and P. Rocai Cabarrocas. Natural occurrence of the diamond hexagonal structure in silicon nanowires grown by a plasma-assisted vapour-liquid-solid method. *Nanoscale*, 9(24):8113–8118, 2017.

[174] A. Fontcuberta I Morral, J. Arbiol, J. D. Prades, A. Cirera, and J. R. Morante. Synthesis of silicon nanowires with wurtzite crystalline structure by using standard chemical vapor deposition. *Adv. Mater.*, 19(10):1347–1351, 2007.

[175] F. Fabbri, E. Rotunno, D. Lazzarini, L.and Cavalcoli, A. Castaldini, N. Fukata, K. Sato, G. Salviati, and A. Cavallini. Preparing the way for doping wurtzite silicon nanowires while retaining the phase. *Nano Lett.*, 13(12):5900–5906, 2013.

[176] Filippo Fabbri, Rotunno Rotunno, Laura Lazzarini, Naoki Fukata, and Giancarlo Salviati. Visible and infra-red light emission in boron-doped wurtzite silicon nanowires. *Sci. Rep.*, 4:1–7, 2014.

[177] D. C. Smith and G. Godard. UV and VIS Raman spectra of natural lonsdaleites: towards a recognised standard. *Spectrochim. Acta A*, 73(3):428–435, 2009.

[178] C. Cayron, M. Den Hertog, L. Latu-Romain, C. Mouchet, C. Secouard, J. L. Rouviere, E. Rouviere, and J. P. Simonato. Odd electron diffraction patterns in silicon nanowires and silicon thin films explained by microtwins and nanotwins. *J. Appl. Crystallogr.*, 42(2):242–252, 2009.

[179] P. Nemeth, L. A. J. Garvie, T. Aoki, N. Dubrovinskaia, L. Dubrovinsky, and P. R. Buseck. Lonsdaleite is faulted and twinned cubic diamond and does not exist as a discrete material. *Nat. Commun.*, 5(5447):1–5, 2014.

[180] I. Vurgaftman, J. R. Meyer, and L. R. Ram-Mohan. Band parameters for III-V compound semiconductors and their alloys. *J. Appl. Phys.*, 89(11 I):5815–5875, 2001.

[181] M. E. Straumanis and E. Z. Aka. Lattice parameters, coefficients of thermal expansion, and atomic weights of purest silicon and germanium. *J. Appl. Phys.*, 23(3):330–334, 1952.

[182] H. I. T. Hauge, S. Conesa-Boj, M. A. Verheijen, S. Koelling, and E. P. A. M. Bakkers. Single-crystalline hexagonal silicon-germanium. *Nano Lett.*, 17(1):85–90, 2017.

[183] M. R. Bergren, C. E. Kendrick, N. R. Neale, J. M. Redwing, R. T. Collins, T. E. Furtak, and M. C. Beard. Ultrafast electrical measurements of isolated silicon nanowires and nanocrystals. *J. Phys. Chem. Lett.*, 5(12):2050–2057, 2014.

[184] P. Jurczak, Y. Zhang, J. Wu, A. M. Sanchez, M. Aagesen, and H. Liu. Ten-fold enhancement of InAs nanowire photoluminescence emission with an InP passivation Layer. *Nano Lett.*, 17(6):3629–3633, 2017.

[185] Y. P. Varshni. Temperature dependence of the energy gap in semiconductors. *Physica*, 34:149–154, 1967.

[186] G. B. Lush. B-coefficient in n-type GaAs. *Sol. Energ. Mat. Sol. C*, 93(8):1225–1229, 2009.

[187] X. Li, K. Zhang, F. Toor, J. Treu, L. Stampfer, G. Koblmüller, and J. P. Prineas. Radiative and nonradiative recombination coefficients of InAs/InAlAs core-shell nanowires. *Cleo*, (111):1–2, 2018.

[188] Y. Wang, H. E. Jackson, L. M. Smith, T. Burgess, S. Paiman, Q. Gao, H. H. Tan, and C. Jagadish. Carrier thermalization dynamics in single zincblende and wurtzite InP nanowires. *Nano Lett.*, 14(12):7153–7160, 2014.

[189] P. Ščajev, M. Karaliunas, E. Kuokštis, and K. Jarašiunas. Radiative and nonradiative recombination rates in cubic SiC. *J. Lumin.*, 134:588–593, 2013.

[190] W. Gerlach, H. Schlangenotto, and H. Maeder. On the radiative recombination rate in silicon. *Phys. Status Solidi*, 13(1):277–283, 1972.

[191] H. Schlangenotto, H. Maeder, and W. Gerlach. Temperature dependence of the radiative recombination coefficient in silicon. *Phys. Status Solidi*, 21(357):357–367, 1974.

[192] T. Trupke, M. A. Green, P. Würfel, P. P. Altermatt, A. Wang, J. Zhao, and R. Corkish. Temperature dependence of the radiative recombination coefficient of intrinsic crystalline silicon. *J. Appl. Phys.*, 94(8):4930–4937, 2003.

[193] G. Cohen-Solal, F. Bailly, and M. Barbé. Critical thickness in heteroepitaxial growth of zinc-blende semiconductor compounds. *J. Cryst. Growth*, 138:68–74, 1994.

[194] K. R. Catchpole. Silicon photoluminescence external quantum efficiency determined by combined thermal/photoluminescence measurements. *Semicond. Sci. Technol.*, 19(12):1411–1415, 2004.

[195] M. B. Rota, A. S. Ameruddin, H. A. Fonseka, Q. Gao, F. Mura, A. Polimeni, A. Miriametro, H. H. Tan, C. Jagadish, and M. Capizzi. Bandgap energy of wurtzite InAs nanowires. *Nano Lett*, 16:5197–5203, 2016.

[196] S. Sasaki, K. Tateno, G. Zhang, H. Suominen, Yu. Harada, S. Saito, A. Fujiwara, T. Sogawa, and K. Muraki. Encapsulated gate-all-around InAs nanowire field-effect transistors. *Appl. Phys. Lett.*, 103(21):1–5, 2013.

[197] T. Tanaka, K. Tomioka, S. Hara, J. Motohisa, E. Sano, and T. Fukui. Vertical surrounding gate transistors using single InAs nanowires grown on Si substrates. *Appl. Phys. Express*, 3(2), 2010.

[198] J. Miao, W. Hu, N. Guo, Z. Lu, X. Zou, L. Liao, and S. Shi. Single InAs nanowire room-temperature near-infrared photodetectors. *ACS Nano*, 8(4):3628–3635, 2014.

[199] T.-T. D. Lu, F.and Tran, W. S. Ko, K. W. Ng, R. Chen, and C. Chang-Hasnain. Nanolasers grown on silicon-based MOSFETs. *Opt. Express*, 20(11):12171–12176, 2012.

[200] M. Scheffler, S. Nadj-Perge, L. P. Kouwenhoven, M. T. Borgström, and E. P. A. M. Bakkers. Diameter-dependent conductance of InAs nanowires. *J. Appl. Phys.*, 106(12):1–4, 2009.

[201] F. Ning, L.-M. Tang, Y. Zhang, and K.-Q. Chen. First-principles study of quantum confinement and surface effects on the electronic properties of InAs nanowires. *J. Appl. Phys.*, 114(22):1–7, 2013.

[202] R. E. Allen, T. J. Humphreys, J. D. Dow, and O. F. Sankey. Theory of surface-defect states and Schottky barrier heights: applications to InAs. *J. Vac. Sci. Technol. B*, 2(3):449–452, 1984.

[203] J. A. Alexander-Webber, C. K. Groschner, A. A. Sagade, G. Tainter, M. F. Gonzalez-Zalba, J. Di Pietro, R.and Wong-Leung, H. H. Tan, C. Jagadish, S. Hofmann, and H. J. Joyce. Engineering the photoresponse of InAs nanowires. *ACS Appl. Mater. Interfaces*, 9(50):43993–44000, 2017.

[204] M. H. Sun, E. S. Leong, A. H. Chin, C. Z. Ning, G. E. Cirlin, Y. B. Samsonenko, V. G. Dubrovskii, L. Chuang, and C. Chang-Hasnain. Photoluminescence properties of InAs nanowires grown on GaAs and Si substrates. *Nanotechnology*, 21(33):1–9, 2010.

[205] F. Wang, S. Yip, N. Han, K. Fok, H. Lin, J. J. Hou, G. Dong, T. Hung, K. S. Chan, and J. C. Ho. Surface roughness induced electron mobility degradation in InAs nanowires. *Nanotechnology*, 24(37):1–6, 2013.

[206] T. V. L'vova, I. V. Sedova, M. S. Dunaevskiĭ, A. N. Karpenko, V. P. Ulin, S. V. Ivanov, and V. L. Berkovits. Sulfide passivation of InAs(100) substrates in Na_2S solutions. *Phys. Solid State*, 51(6):1114–1120, 2009.

[207] M. H. Sun, H. J. Joyce, Q. Gao, H. H. Tan, C. Jagadish, and C. Z. Ning. Removal of surface states and recovery of band-edge emission in InAs nanowires through surface passivation. *Nano Lett.*, 12(7):3378–3384, 2012.

[208] J. Treu, M. Bormann, H. Schmeiduch, M. Döblinger, S. Morkötter, S. Matich, P. Wiecha, K. Saller, B. Mayer, M. Bichler, M. C. Amann, J. J. Finley, G. Abstreiter, and G. Koblmüller. Enhanced luminescence properties of InAs-InAsP core-shell nanowires. *Nano Lett.*, 13(12):6070–6077, 2013.

[209] J. W. W. van Tilburg, R. E. Algra, W. G. G. Immink, M. Verheijen, E. P. A. M. Bakkers, and L. P. Kouwenhoven. Surface passivated InAs/InP core/shell nanowires. *Semicond. Sci. Technol.*, 25(2):1–7, 2010.

[210] X. Chen, Q. Zhuang, H. Alradhi, Z. M. Jin, L. Zhu, X. Chen, and J. Shao. Midinfrared photoluminescence up to 290 K reveals radiative mechanisms and substrate doping-type effects of InAs nanowires. *Nano Lett.*, 17(3):1545–1551, 2017.

[211] B. Shin, J. B. Clemens, M. A. Kelly, A. C. Kummel, and P. C. McIntyre. Arsenic decapping and half cycle reactions during atomic layer deposition of Al_2O_3 on $In_{0.53}Ga_{0.47}As$(001). *Appl. Phys. Lett.*, 96(25):1–3, 2010.

[212] R. Timm, A. Fian, M. Hjort, C. Thelander, E. Lind, J. N. Andersen, L. E. Wernersson, and A. Mikkelsen. Reduction of native oxides on InAs by atomic layer deposited Al_2O_3 and HfO_2. *Appl. Phys. Lett.*, 97(13):1–4, 2010.

[213] H. A. Potts. Gold-free growth of InAs nanowires : growth , structural electrical properties. pages 1–159, 2017.

[214] J. Ahn, T. Kent, E. Chagarov, K. Tang, A. C. Kummel, and P. C. McIntyre. Arsenic decapping and pre-atomic layer deposition trimethylaluminum passivation of Al_2O_3/InGaAs(100) interfaces. *Appl. Phys. Lett.*, 103(7):1–4, 2013.

[215] G. Koblmüller, K. Vizbaras, S. Hertenberger, S. Bolte, D. Rudolph, J. Becker, M. Döblinger, M. C. Amann, J. J. Finley, and G. Abstreiter. Diameter dependent optical emission properties of InAs nanowires grown on Si. *Appl. Phys. Lett.*, 101(5):1–5, 2012.

[216] Z. Zanolli, F. Fuchs, J. Furthmüller, U. Von Barth, and F. Bechstedt. Model GW band structure of InAs and GaAs in the wurtzite phase. *Phys. Rev. B*, 75(24):1–8, 2007.

[217] H. J. Joyce, J. Wong-Leung, Q. Gao, H. H. Tan, and C. Jagadish. Phase perfection in zinc blende and wurtzite III- V nanowires using basic growth parameters. *Nano Lett.*, 10(3):908–915, 2010.

[218] P. J. P. Tang, C. C. Phillips, and R. A. Stradling. Excitonic photoluminescence in high-purity InAs MBE epilayers on GaAs substrates. *Semicond. Sci. Technol.*, 8(12):2135–2142, 1993.

[219] L. Schultheis, J. Kuhl, A. Honold, and C. W. Tu. Picosecond phase coherence and orientational relaxation of excitons in GaAs. *Phys. Rev. Lett.*, 57(14):1797–1800, 1986.

[220] N. F. Mott. The basis of the electron theory of metals, with special reference to the transition metals. *Proc. Phys. Soc. Sect. A*, 62(7):416–422, 1949.

[221] J. Shah, M. Combescot, and A. H. Dayem. Investigation of exciton-plasma Mott transition in Si. *Phys. Rev. Lett.*, 38(25):1497–1500, 1977.

[222] L. Kappei, J. Szczytko, F. Morier-Genoud, and B. Deveaud. Direct observation of the Mott transition in an optically excited semiconductor quantum well. *Phys. Rev. Lett.*, 94(14):1–4, 2005.

[223] R. Zimmermann. Nonlinear Optics and the Mott Transition in Semiconductors. *Phys. Status Solidi*, 146(1):371–384, 1988.

[224] W.W Chow and S. W Koch. Semiconductor-Laser Fundamentals: Physics of the Gain Materials. *Springer*, pages 1–245, 1999.

[225] L. F. Hernández-García, J. C. Basilio-Ortiz, F. Sutara, and I. Hernández-Calderón. Photoluminescence study of the excitation power dependence of the peak intensities of an asymmetric double quantum well. *AIP Conf. Proc.*, 1934:1–5, 2018.

[226] V. L. Dalal, W. A. Hicinbothem, and H. Kressel. Carrier lifetimes in epitaxial InAs. *Appl. Phys. Lett.*, 24(4):184–185, 1974.

[227] D. Sager, C. Gutsche, W. Prost, F. J. Tegude, and G. Bacher. Recombination dynamics in single GaAs-nanowires with an axial heterojunction: n- versus p-doped areas. *J. Appl. Phys.*, 113(17):1–5, 2013.

[228] B. M. Borg and L.-E. Wernersson. Synthesis and properties of antimonide nanowires. *Nanotechnology*, 24(20):1–18, 2013.

[229] D. Ercolani, M. Gemmi, L. Nasi, F. Rossi, M. Pea, A. Li, G. Salviati, F. Beltram, and L. Sorba. Growth of InAs/InAsSb heterostructured nanowires. *Nanotechnology*, 23(11):1–9, 2012.

[230] W. N. Du, X. G. Yang, X. Y. Wang, H. Y. Pan, H. M. Ji, S. Luo, T. Yang, and Z. G. Wang. The self-seeded growth of InAsSb nanowires on silicon by metal-organic vapor phase epitaxy. *J. Cryst. Growth*, 396:33–37, 2014.

[231] Wenna Du, Xiaoguang Yang, Huayong Pan, Xiaoye Wang, Haiming Ji, Shuai Luo, Xianghai Ji, Zhanguo Wang, and Tao Yang. Two different growth mechanisms for Au-free InAsSb nanowires growth on Si substrate. *Cryst. Growth Des.*, 15(5):2413–2418, 2015.

[232] A. C. Farrell, W. J. Lee, P. Senanayake, M. A. Haddad, S. V. Prikhodko, and D. L. Huffaker. High-quality InAsSb nanowires grown by catalyst-free selective-area metal-organic chemical vapor deposition. *Nano Lett.*, 15(10):6614–6619, 2015.

[233] Z. M. Fang, K. Y. Ma, D. H. Jaw, R. M. Cohen, and G. B. Stringfellow. Photoluminescence of InSb, InAs, and InAsSb grown by organometallic vapor phase epitaxy. *J. Appl. Phys.*, 67(11):7034–7039, 1990.

[234] J. A. Van Vechten and T. K. Bergstresser. Electronic structures of semiconductor alloys. *Phys. Rev. B*, 1(8):3351–3358, 1970.

[235] M. De La Mata, R. Leturcq, S. R. Plissard, C. Rolland, C. Magén, J. Arbiol, and P. Caroff. Twin-induced InSb nanosails: a convenient high mobility quantum system. *Nano Lett.*, 16:825–833, 2016.

[236] N. Wang, X. Yuan, X. Zhang, Q. Gao, B. Zhao, L. Li, M. Lockrey, H. H. Tan, C. Jagadish, and P. Caroff. Shape engineering of InP nanostructures by selective area epitaxy. *ACS Nano*, 13(6):7261–7269, 2019.

[237] M. Fisher and A. Krier. Photoluminescence of epitaxial InAs produced by different growth methods. *Infrared Phys.*, 38:405–413, 1997.